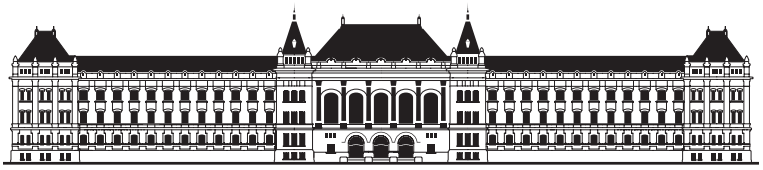

M Ű E G Y E T E M 1 7 8 2
Budapest University of Technology and Economics
Institute of Nuclear Techniques

Particle physics detector development and application for muography

PhD Dissertation

Gábor Nyitrai

Supervisor: Dr. Dezső Varga
Wigner Research Centre for Physics

Budapest
2023

Contents

Abbreviations

MWPC: Multi-Wire Proportional Chamber

MPGD: Micro-Pattern Gas Detector

RPC: Resistive Plate Chamber

DEM/DTM: Digital Elevation Model / Digital Terrain Model

CAD: Computer-Aided Design

PMT: Photomultiplier Tube

WLS: Wavelength Shifting optical Fibres

REGARD: Innovative Gaseous Detector Development Research Group (original name: *R*MKI-*E*LTE *GA*seous detector *R*esearch and *D*evelopment)

CCC: Close Cathode Chamber

FWHM: Full Width at Half Maximum

PCB: Printed Circuit Board

EDM: Electrical Discharge Machining

DAQ: Data Acquisition

ADC: Analog-to-Digital Converter

THP: Temperature, Humidity, Pressure

ABS: Acrylonitrile Butadiene Styrene

GEM: Gas Electron Multiplier

TPC: Time Projection Chamber

CT: Computed Tomography

PET: Positron Emission Tomography

FBP: Filtered BackProjection

ML-EM: Maximum Likelihood, Expectation Maximization

Chapter 1

Introduction

Muography is a novel imaging method that utilizes the muon particles present in the cosmic rays on Earth. These naturally occurring high-energy muons are able to penetrate even kilometers of rock, but denser matter absorbs more muons, similar to X-rays in bones. To a first approximation, the detected muon flux (normalized count rate) depends only on the zenith angle of the arriving particles and the material density integrated along the muon path (density-length). The strictly monotone function between the muon flux and density-length is the core of absorption muography, thus providing a powerful tool to image the average densities of 10–1000 m rock layers by measuring muon trajectories in a given direction unit. The geometric constraint of muography is that the altitude of the particle tracking detector must be lower than the examined object level: no muons come from or below the horizon. However, if the geometric constraint can be overcome, then muography can provide superior imaging resolution compared to other non-destructive geophysical techniques (such as gravimetry, seismic, or electric resistivity survey). Applications arise in multiple disciplines, including volcanology, mining, archeology, or civil engineering, by locating density anomalies like unknown cavities, erosion zones, high-density ore bodies, or even dynamic density changes. In some cases with multiple detector locations, even 3D density reconstruction is possible.

Different muon tracking detector technological directions evolved for muography, originating from the high-energy particle physics experiments. Our detector concepts in the REGARD group[1] are based on the MWPC (Multi-Wire Proportional Chamber) gaseous detector type, which is an inexpensive, reliable, robust, low gas and power consumption design with sufficient tracking resolution (below 10 mm). However, the detectors also have to meet further challenges due to the fact that muographic data collection typically takes months in the harsh environment of a remote field.

The research group I am working in is also involved in developments for the cutting-edge tracking technology of Micro-Pattern Gaseous Detector (MPGD), which enjoys widespread popularity in high-energy particle physics. The MPGD can also be a promising choice for specific muography applications, especially if high resolution and monitoring is required, yet detectorphysical challenges can arise in terms of signal gain homogeneity or production defects.

The motivation of this PhD dissertation is to demonstrate my contribution in the research

[1] Innovative Gaseous Detector Development Research Group, Wigner RCP

and developments of gaseous detectors and the application for muography, aiming to meet the aforementioned requirements and elaborate further on the muographic data evaluation processes, ultimately leading to radiographic or tomographic imaging. More specifically, I elaborate on my developments for the advanced MWPC for the applicability in a wide range of muography situations, present the research on low gas consumption in order to significantly reduce the detector maintenance, introduce our MPGD scanner and my developments on it in the aim of an exclusive gain examination, and finally I describe my efforts to produce muographic images to reconstruct density distributions.

Chapter 2 is a literature review on muography, the cosmic muon physics, and muon tracking possibilities. All the following chapters include different aspects of my research work on the subject, where the line of reasoning from section to section start with its own introduction about research preceding my work, then elaborate on the thesis statements, and finally the results and conclusions are drawn. In the last chapter, an outlook are given about preliminary results and future perspectives of my research work which are awaiting publication.

Chapter 2

Principles of Muography

2.1 Cosmic muon physics

Cosmic radiation on the surface of the Earth is a natural phenomenon known for a century, based on the pioneering work by V. Hess [1] amongst others. He measured an increasing ionization rate with increasing altitude by the famous balloon experiment, thus proving that this radiation originates mostly above and not below the surface of the Earth. Later, between 1930 and 1950, cosmic rays were the main experimental source for the discoveries of early particle physics until the appearance of particle accelerators. The most relevant to this thesis, the muon (μ) particle was discovered in 1936 by C.D. Anderson and S.H. Neddermeyer in a cloud chamber [2], which is shown in Fig. 2.1.

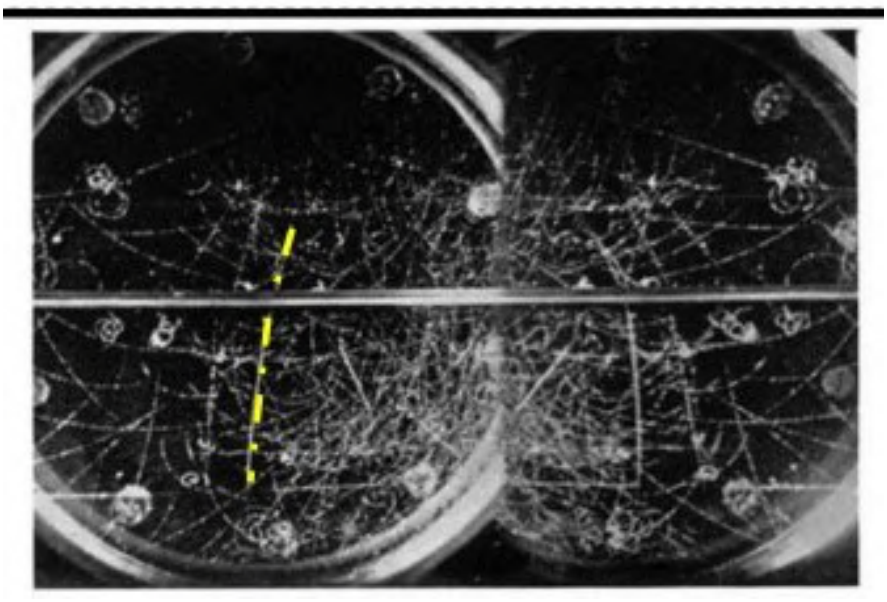

Figure 2.1: The discovery of the muon particle (1936) [2] in the cosmic rays by a cloud chamber experiment. Due to the curved track of the new particle in a magnetic field, its mass was determined to be between those of an electron and a proton, and its charge is positive or negative.

Regarding the origin of these muons on Earth, we now know that they are produced by high-energy collisions of cosmic rays in the upper atmosphere. The protons (and a small fraction of heavier nuclei, and also electrons, positrons, and antiprotons) that originate mainly from galactic radiation and hit the Earth are called primary cosmic rays (Fig. 2.2). Once reaching our planet, they collide with the nuclei of the upper atmosphere, and due to the laws of strong nuclear interactions, a shower of secondary particles, e.g., pions (π^+, π^-, π^0), kaons (K^+, K^-, K^0_S, K^0_L), and their cascade decay products (driven by the weak nuclear interactions), most notably muons (μ^+, μ^-) are produced.

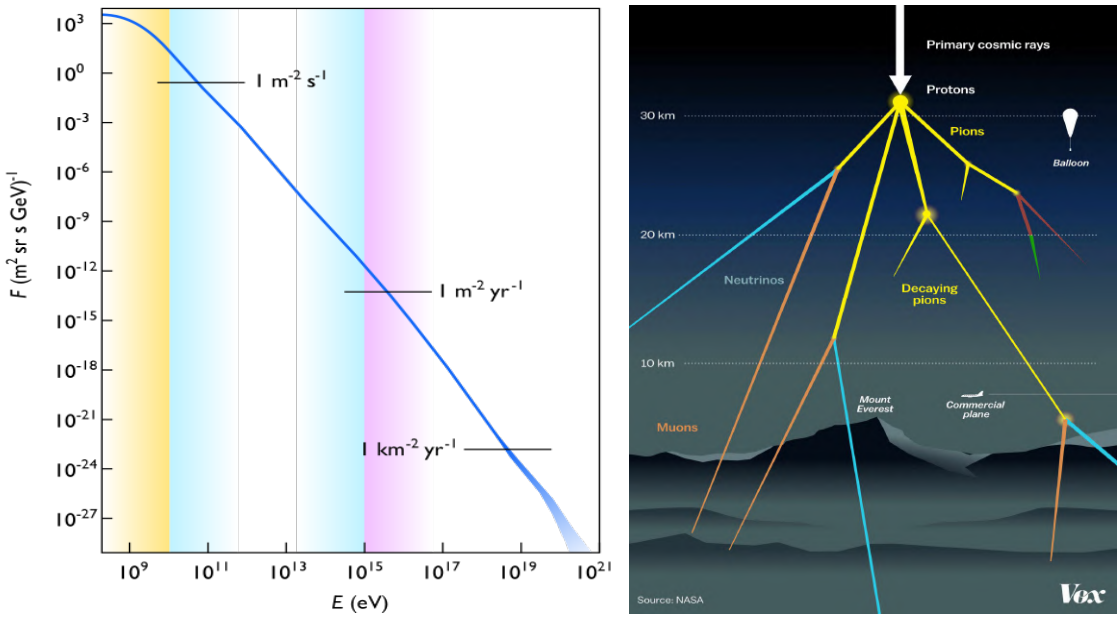

Figure 2.2: Left: Cosmic particle flux versus energy at the top of Earth's atmosphere. The the energy bands marked as yellow, blue, and purple are attributed to solar, galactic, and extragalactic cosmic rays, respectively. Right: Primary cosmic rays collide with the nuclei of the upper atmosphere and create a shower of secondary particles. Through a cascade decays, large number of muons are produced which can reach the surface of the Earth (image: Javier Zarracina/Vox; NASA)

Muography, as the name suggests, utilizes the muon component of the cosmic rays, which is the largest portion of the ionizing cosmic particles on sea level (order of magnitude more than protons and neutrons, and two order magnitude more than electrons or pions), arriving at a rate of 100–200 Hz/m^2[3]. The energy of the muon is inherited from the primary cosmic particle ancestor, and the higher was the energy of the primary, the higher is the energy of the new born muon (due to the conservation of momentum). The birth rate and energy depends on the mean free path of pions and kaons in the atmosphere (do they interact with something before decaying into muons). Eventually, this depends on the altitude of the high-energy collision, the angle of arriving primary particle, the complex process of cascade decays, and the density of the atmosphere. The initial energy distribution of muons receives a special attention in Sec. 4.1 as it plays a key role in calculating the number of muons, thus creating a muographic image. In advance, it is important to mention that typically the high-

energy (>1 GeV) muons are interesting for us. For this reason, the muon rate is constant (in a first approximation) day and night, throughout the year, because the high-energy part of the muon spectrum originates from the galactic or extragalactic sources and not from the Sun.

Like the well known electron, the muon also belongs to the lepton particle family, but it is ∼200 times heavier than an electron. It is unstable, decaying into lighter particles ($\mu^+ \to e^+ \overline{\nu}_\mu \nu_e$ and $\mu^- \to e^- \nu_\mu \overline{\nu}_e$) with a mean lifetime of $\tau \approx 2.2\,\mu s$ at rest. Considering that most muons are produced around 15 km above sea level, by classical mechanical calculation (considering light speed and the given lifetime) they should not reach the surface of the Earth. A remarkable evidence for Einstein's theory of special relativity is that due to the high momentum of the muon, the relativistic dilation increases the observed lifetime by the Lorentz factor ($\gamma = 1/\sqrt{1-\beta^2}$, where $\beta = v/c$ is the speed of the muon relative to the speed of light). For example, a muon with 4 GeV energy corresponds to $\gamma \approx 20$, thus the decay length is $\gamma v \tau \approx 24\,km$[1].

Nature is kind to us: the atmosphere has the right thickness for muons to produce and reach the surface, and also the penetration of muons into rock is high enough to reach even multiple kilometer deep under the surface. Due to the attenuation in the rock, the rate of the muons in a given depth is proportional to the amount of material along their path length. This is why muon imaging of the irradiated rock is possible and the energy deposition of the muon in different materials is a key factor in these investigations. Fig. 2.3 shows the muon stopping power in different mediums on different energy scales.

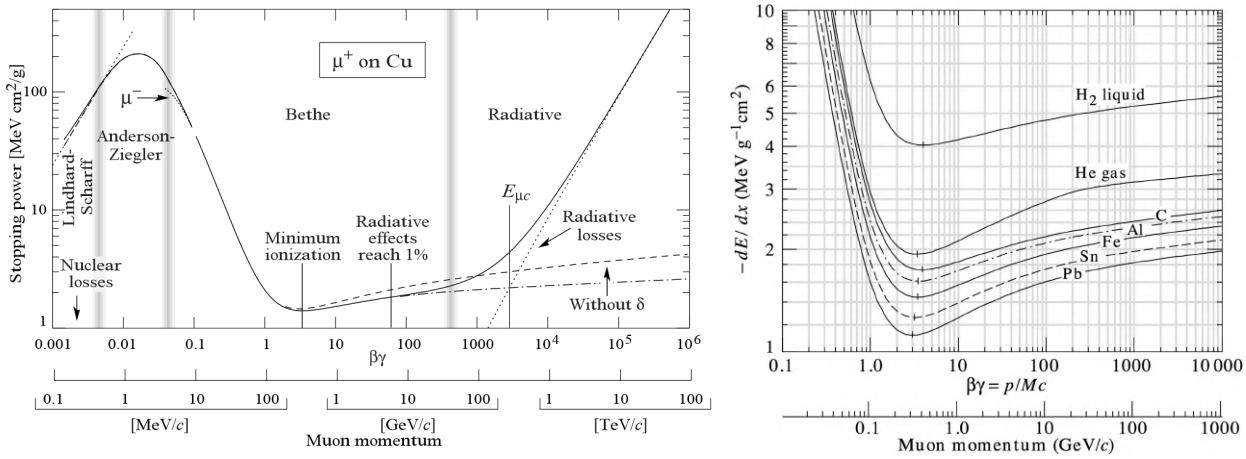

Figure 2.3: Left: Muon stopping power (Bethe formula normalized to density) in copper, over nine orders of magnitude in momentum. Vertical bands are the characteristic points of the curve. Arrows and dashed lines indicate specific effects on the Bethe formula. Right: Muon stopping power in different materials. Note, that the muon energy loss in higher atomic number materials is less due to the $\frac{Z}{A}$ dependence. Figures are adapted from [4].

The mean energy loss of a charged particle is expressed in the Bethe formula[4] as

[1]This calculation is not taking into account the continuous slow-down which can be relevant at lower energies, but negligible in higher energies.

$$\left\langle -\frac{dE}{dx} \right\rangle = Kz^2 \frac{Z}{A} \frac{1}{\beta^2} \left[\frac{1}{2} \ln \frac{2m_e c^2 \beta^2 \gamma^2 W_{\max}}{I^2} - \beta^2 - \frac{\delta(\beta\gamma)}{2} \right], \tag{2.1}$$

where z is the charge number of the incoming particle ($z = 1$ for muons), Z and A the atomic and mass number of the medium, K, $W_{\max}$, I, and $\delta(\beta\gamma)$ are coefficients of the medium for a given incoming particle (proportionality coeffitient, maximum kinetic energy transfer, and mean excitation energy, density effect correction), m_e and c are universal constants (electron mass and speed of light). The energy deposition of muon results mostly from electromagnetic interactions (the radiative losses, like pair production and bremsstrahlung, become significant only in very high energies). The function follows a $-(\ln \beta\gamma - \beta\gamma)/\beta\gamma$ nature (if $0.1 \lesssim \beta\gamma \lesssim 1000$), which has a minimum around 0.25 GeV/c momentum (called minimum ionizing particle or MIP), and above that, the curve is almost completely flat. As mentioned before, the muon energies above 1 GeV are interesting for us, and since the muon momenta above TeV are rare, the relevant part of the spectrum is the 1–1000 GeV range. In this range, the incoming muons with different speeds have almost the same energy loss rate in the medium (and in the detector) due to the flatness of the curve. This means that measuring the speed of cosmic muon is nearly impossible at high energies without stopping them, and challenging in the intermediate energies (0.1–2 GeV). The latter is important for background filtering, but besides that, we do not actually need to measure the muon energy for muography. We are only interested in their directions because the muon rate data in a given direction includes the density information concerning the volume of interest.

2.2 Muography

The muon rate from a given direction is inversely proportional to the amount of material it travelled through as a consequence of the continuous energy loss. This is the basic principle of the "absorption muography", similarly to the X-ray of bones but for large objects or rock layers in the range of 10–1000 m rock thickness. The muon rate is defined by the muon flux (Φ [m^{-2}sr^{-1}s^{-1}]) which is the number of muons (N_{det}) detected in a given direction (θ, ϕ being the usual geodesic zenith and azimuth angles of the horizontal coordinate system, shown in Fig. 2.4 top left panel) and normalized by the 'Acceptance' effective detector surface (A_{eff}, including detector efficiencies), solid angle bin of direction (Ω), and measurement time (τ):

$$\Phi(\theta, \phi, t) = \frac{N_{\text{det}}(\theta, \phi, t)}{A_{\text{eff}}(\theta, \phi) \cdot \Omega \cdot \tau}. \tag{2.2}$$

As a first approximation, the muon flux depends on the path length (L) and average density ($\overline{\rho}$) traveled by the muon through the material: $\Phi(L \cdot \overline{\rho})$. Here $L \cdot \overline{\rho} = \varrho$ is defined as density-length, also called "opacity" [5], in the usual unit of g/cm^2 or m.w.e. (meter-water-equivalent, equivalent of g/mm^2). The distance traveled in the air is neglected and later the altitude correction will contain it. The strictly monotone mapping between the two quantities ($\Phi \to \varrho$) is the core of absorption muography, that allows for locating density anomalies like unknown cavities, erosion zones, high-density ore bodies, or even dynamic density changes

in result (for more details, see Sec. 4.1). This method was used to map the internal density structure of Satsuma-Iwojima Volcano shown as an example in Fig. 2.4. Muons are traversing through the volcanic cone, and the amount of absorbed particles strongly depends on the filling of the magma conduit-reservoir system. The same method can be applied, just to name a few, in archaeology, mining, or civil engineering, to localize density anomalies (significant muographic density deviations from an expected average density).

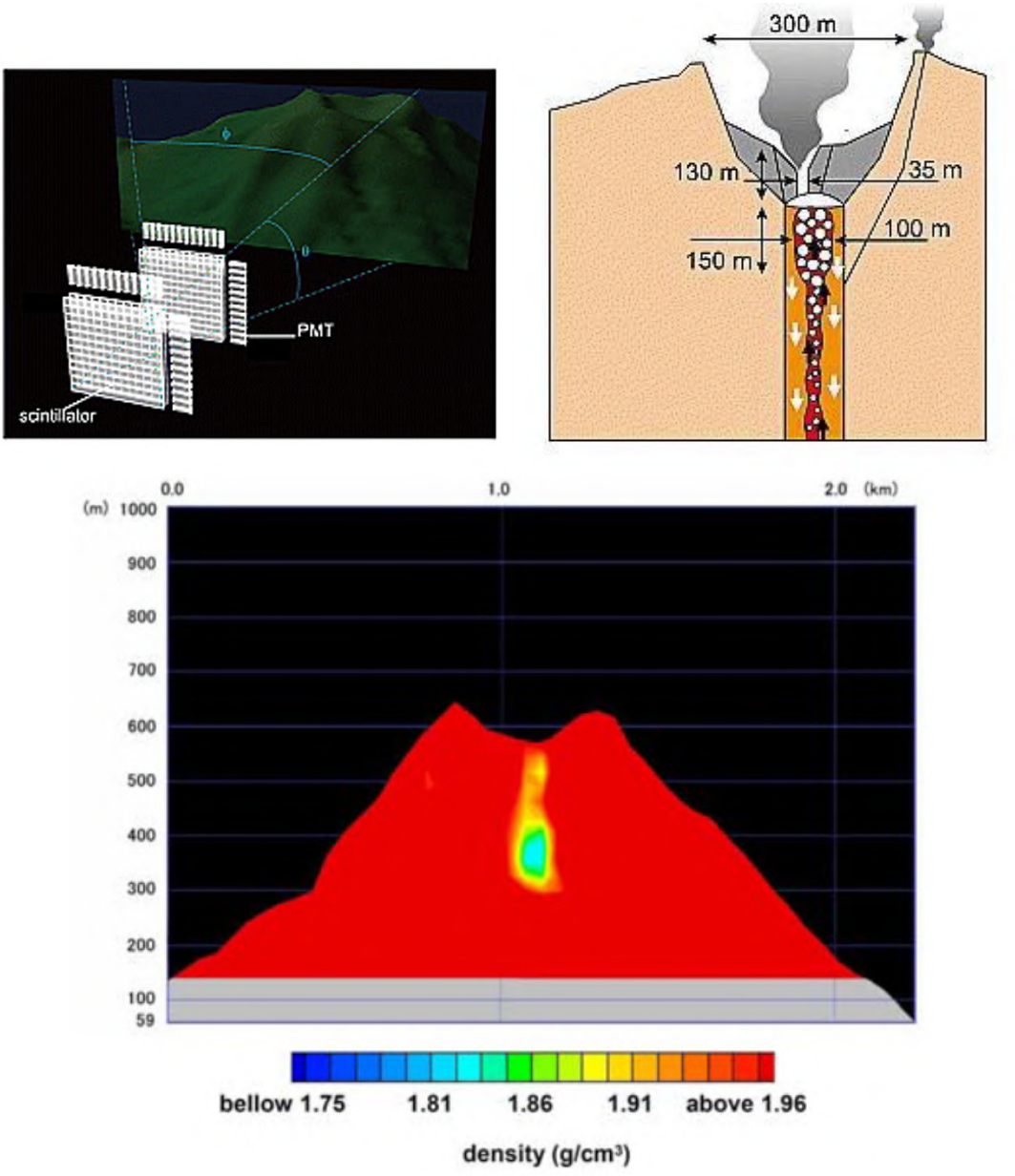

Figure 2.4: The schematic view of the interior structure of the Satsuma-Iwojima Volcano (top right) and the muography detection principle (top left). The resulting muographic density image of the upper few hundred meters of the volcanic cone (bottom) [6].

The first significant pioneering applications of absorption muography was demonstrated

by Alvarez et al. [7] in 1970, but the phenomenon has been investigated even prior [8]. I would also mention here that the effect of an underground tunnel on the muon flux has also been noticed in the Hungarian Jánossy laboratory in the early sixties [9], which was one of the top cosmic ray physics research complex in that time. However the cosmic muon absorption and its utilization was known for a long time, the technology had to improve a lot to be feasible. Since the beginning of the twenty-first century, the number of muography research results are growing ever since [10], influencing a wide range of fields, including volcanology[6, 11, 12, 13, 14, 15, 16, 17, 18, 19]; mining[20, 21, 22, 23]; archaeology[24, 7, 25]; civil engineering[26, 27, 28]; speleology[29, 30]; ice-[31], water-[32, 33, 34], and atmosphere-monitoring[35, 36]; just to mention a few.

Muography relies on the tracking of cosmic muons, in other words the measurement of particle paths travelling through a detector. The high-energy muons travel in straight lines. Small deviations could be caused by multiple Coulomb scattering [37] but it is usually negligible and only measurable in lower energies [38]. So essentially, we measure the rate of muons in a given direction by fitting straight lines to each incoming ionizing particle. Arguments to support the assumption that most of these straight ionizing particles are in fact high-energy muons coming through the examined object, is discussed in Sec. 2.3.2. The details of the conversion between the muon flux (a normalized quantity of the muon rate), and the density-length (the product of rock length and density) is derived in Sec. 4.1. After this conversion, a muographic image can be provided, showing the static density distribution or dynamic density changes inside the object. It is important to note though, that 2D muography (muon radiography) can provide only the average density in the given direction (a low density region without cavities can provide the same image than a high density region with cavities). To get a 3D density distribution (muon tomography), multiple viewpoint data and the process by a tomographic inversion algorithm required, similar to the case of medical CT imaging. This is described in Sec. 4.2.

There are alternative approaches to utilize the naturally occurring muons for imaging. The "scattering muography" method can produce information about the atomic number and density distribution in an examined volume (up to a few cubic meter). The basic principle is that muons at intermediate energies can suffer multiple scattering (see Eq. 4.13 below) more likely in higher $Z \cdot \rho$ materials, so mapping the voxel space by scattering power results in an image sensitive to the $Z \cdot \rho$ contrasts (see Fig. 2.5).

This method was proposed first in 2003, by Borozdin et al. at Los Alamos[40]. Recently, Niederleithinger et al. showed a detailed study of this method, comparing the imaging capabilities with radar, ultrasound, and X-ray laminography[41]. Applications of scattering muography focus mainly on nuclear cargo imaging, nuclear waste monitoring, and reinforced concrete condition assessment (see, for example, applications reviewed by P. Checchia[42]).

Another alternative muography method was proposed in 2016 by I. Bikit et al.[43] at Novi Sad, in collaboration with our group at Budapest. As muons pass through matter, interactions result in secondary particles (mostly electrons and gamma photons) and the cross sections of the processes vary by the density and the atomic number of materials. This technique could be used to investigate mainly the low atomic number content of the target. Recent results are summarized by G. Galgóczi et al.[44]. The combination with the previously mentioned methods are also proposed by groups from Hengyang, China[45], and from Bremerhaven, Germany[46].

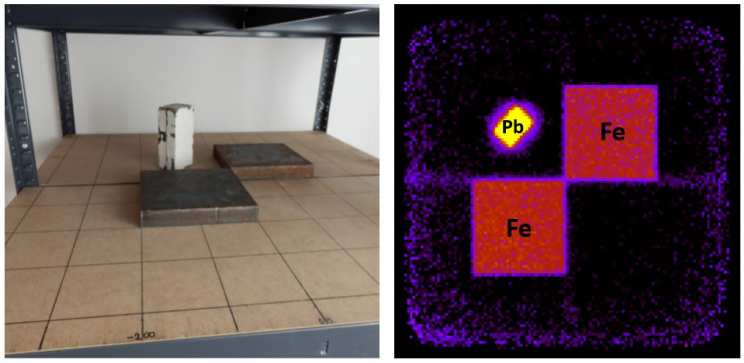

Figure 2.5: First scattering muography image of two Fe and a Pb blocks from our research group in Wigner RCP [39].

Muography in general is a prospering new science field with numerous multidisciplinary applications, but like many other things, it also has its limitations. One issue is the relatively low muon rate: 100–200 Hz/m^2 as mentioned before, or an illustrative example, roughly one muon pierces our palm in every second. For a sufficient statistical certainty, usually hundreds of thousands or even millions of muon tracks are needed from one viewpoint of a muographic survey, depending on the required resolution. This can be achieved in three ways: either by large telescopes, an array of (many) telescopes, or long measurements. In the first two cases, the limiting factor is the available space (e.g., underground) or the budget. In the latter case, the data allocation time is typically weeks or months. Another important issue is that muons only come from above. Therefore, we cannot image from the horizontal direction of the detector and below. The altitude of the detector always has to be lower than the examined object. The decrease of muon flux depends on the arrival zenith angle (θ) which can be roughly approximated with a $\cos^2(\theta)$ function in open air and gets more complicated in rock, as discussed in details in Sec. 4.1.

In conclusion, a field muographic survey generally requires at least some of the following preparations (although not all are always readily available):

- Collecting all the available preliminary information about the location (DEM/DTM surface maps, tunnel maps, rock compositions, average densities, etc.)
- Planning the most suitable measurement positions and viewing angle
- Estimating the required duration for each data collection in different viewpoints
- Preparing the infrastructure (power or batteries, internet or manual data collection, detector transportation, etc.)
- Muon flux and uncertainty calculations, simulations.

After this short overview in this section, the interested reader is invited to find out more details about muography in the following review articles: [10, 3, 47, 48] or in the book from Oláh et al. [49].

2.3 Detectors used in muography

Muon detectors originate from the high-energy particle physics experiments. The continuous push to the technological limits for more than a century has improved the technologies to the level that current detectors are capable of tracking charged particles in 3D with a resolution of tens of micrometers, and are read out digitally at an amazingly high rate. Answering fundamental scientific questions not only provides more knowledge about our world, it also contributes to the society by technological advancements and spin-offs for applications. Muography is the application of particle detectors for geosciences, archaeology, or civil engineering, and although experimental particle physics knowledge is necessary, we cannot use the same detectors one-to-one from those of fundamental sciences. Imaging usually requires remote field data collection in harsh environments, so detectors need to step out of the comfortable laboratories. In contrast to the high-energy physics experiments, muography is not exposed to such a high particle rate (as it was discussed in the previous section), and the required resolution is also lower depending on the specific application. In turn, the robustness against environmental and transportation stress, mobility, autonomy, low gas and power consumption, safety, and cost efficiency are the most important driving factors for R&D.

There are three main technological families in muography, namely gaseous, scintillator, and emulsion detectors. The attributes and different sub-branches of these families is discussed below. The muography detectors can be categorized not only based on technological aspect. It is also an important factor for the detector design if it is placed underground or at surface, and the detector requirements in these cases are discussed in the subsections after the next one.

2.3.1 Detector families and sub-types

Gaseous detectors: A gaseous tracking detector developed in the REGARD group is shown as an example in Fig. 2.6.

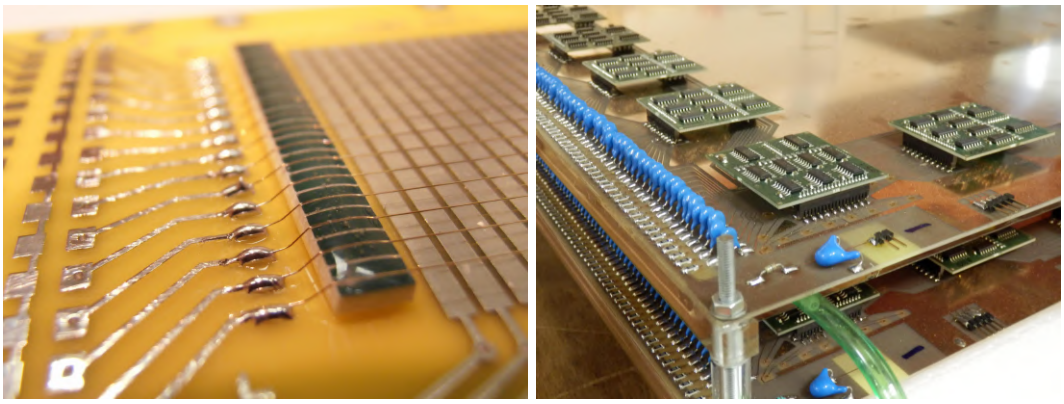

Figure 2.6: One of the gaseous detectors developed by the REGARD group[50]. Left: the inner structure contains wires which provide the coordinate information of the passing particle. Right: photo from the assembled detector, containing the custom designed electronics and a gas inlet tube (green).

The operational principle of gaseous detectors is that the passing particle ionizes the atoms (or molecules) of the gas in a chamber, leaving a trail of electrons and ions. Due to high voltage applied to the anode, the electric charges are collected resulting in signals on the anode. Usually a noble gas is used as ionizing medium (since they have the lowest electron affinity), but in most cases other gases, called quenching gas, are also mixed in for stability [51]. Anodes are usually thin wires (∼20 µm diameter), and the cathode is the wall of the detector itself. Gaseous detectors can be categorized – based on the gas amplification processes – into ionization detectors, proportional chambers, and Geiger-Müller counters. Ionization detectors are utilized in special cases (high-dose rate measurements, gas chromatography) and Geiger-Müller counters are widely used in dosimetry due to their simplicity. Beyond these, most of the gaseous detectors in the technological frontiers are applied in the proportional region. This means that a so-called Townsend avalanche of secondary ionization electrons appear in the gas volume due to the high voltage around the anode (Fig. 2.7 right), causing a gain before the signal formation. The energy - deposited by a passing particle in the gas - is proportional to the signal amplitude, hence the name "proportional chamber". Energy deposition can be useful information but eventually we want to measure the position where the particle passed through the detector. A simple solution is to stretch multiple anode wires next to each other and the position of the wire which provides signal is the coordinate of the passing particle (Fig. 2.7 left). This gaseous detector type is called MWPC (Multi-Wire Proportional Chamber), invented by G. Charpak [52] who has been awarded for his work with Nobel Prize in 1992.

Although MWPCs revolutionized the particle detector technology in the 70s, they required heavy mechanical support structures and constant environmental parameters for stability. Advanced versions, developed for muography by our group, is described in Sec. 3.1. The resolution can be further improved without the risk of sparking by applying microstructure technologies, this is discussed in "Micro-Pattern Gas Detectors" Section 3.2. There are other techniques used in muography as well with enhanced resolution, like the drift tube technology [53, 54] (separated gas volume per wire, the constant "drift" speed of the ionized electron towards the anode is used for the position fine-tuning) or the RPC (Resistive Plate Chamber) [55, 56, 21, 57] (highly resistive plates make it possible to place the anodes closer without sparks) but these are beyond the scope of this dissertation.

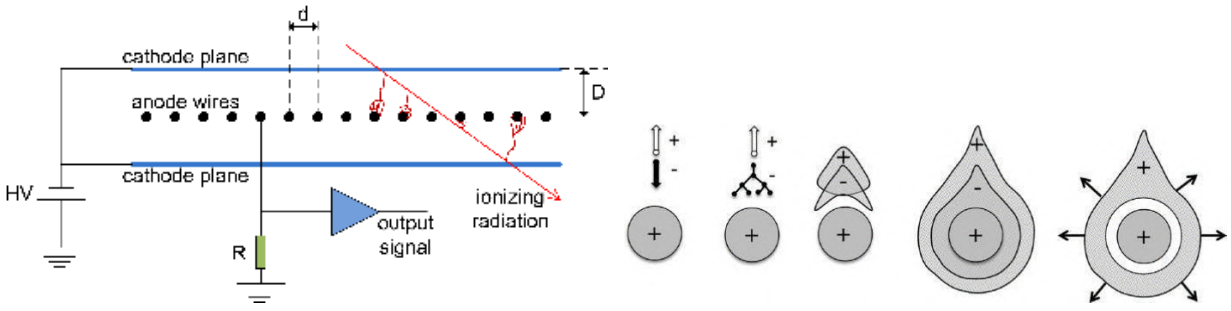

Figure 2.7: Left: schematic of the classical MWPC detector (image: N.B. Budanur; ITÜ). Right: avalanche formation around the high voltage anode wires, adapted from [51].

Scintillator detectors: Scintillation is the physical phenomenon where a material, called scintillator, emits UV or visible light under excitation from an incoming particle. This material can be made of inorganic crystals (with so called activator impurity in them), or organic materials (plastics, liquids, or gas). In muography, the plastic scintillators have spread, because of the relatively easy fabrication and low production cost. Fig. 2.8 shows the potential energies of a molecular chain depending on the distance between atoms.

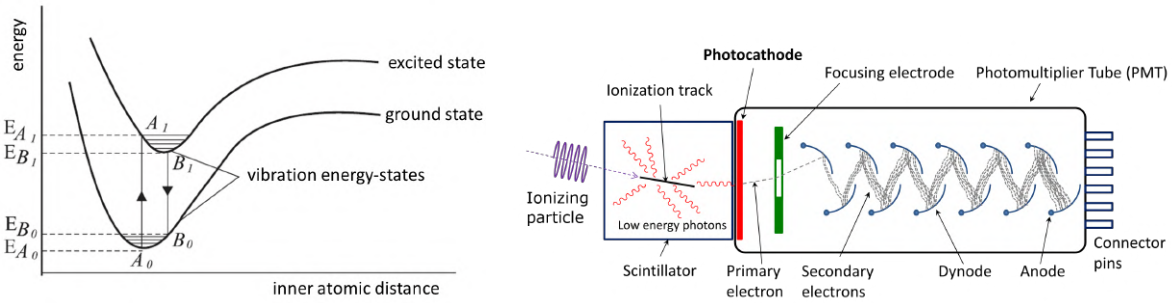

Figure 2.8: Left: illustration of energy states and excitation process in organic scintillators (modified figure from Ref. [58]). Right: schematic of scintillator coupled with a photomultiplier tube.

Excitation can occur due to particle radiation ($A_0 - A_1$ transition) which de-excites to the minimum energy state B_1 via heat release. From here, it returns to the ground state by emitting a photon (transition from B_1 to B_0) which is not absorbed because its energy is smaller than that needed for excitation ($B_1 - B_0 < A_1 - A_0$). The scintillator is therefore transparent to these photons, and by detecting the photons, the properties of the ionizing particle can be measured. The most common tool for scintillation photon detection is the Photomultiplier Tube (PMT) which contains a photon-to-electron conversion plate (photocathode) and multiplier electrodes with stepwise increasing voltage (dynodes) in a vacuum tube. International literature recognises L.A. Kubetsky (USSR) and V. Zworykin (RCA group, USA) amongst others who invented the PMT, but that time it was only used for radio signal amplification. An uncredited pioneer of PMT was Hungarian physicist Zoltán Bay who first proposed the application of PMT for individual electron and gamma photon detection [59] and later developed the device for detecting alpha-, beta-, and X-rays as well. The PMT is still common in scintillator technology (low noise, low dark current, simple response function, less sensitive to temperature), but nowadays the solid-state silicon photomultipliers (SiMP) have a great impact too (low price, high signal gain, insensitive to magnetic fields, etc.).

Considering the scintillator detectors for particle tracking, the usual arrangement is long scintillator bars (or fibers, or other shapes) next to each other and another layer of bars perpendicular to the first one. Similar to that in case of gaseous detectors, the positions of the channels producing signal are the coordinates of the passing particle. The rectangular cross-section bars have simple construction with a well defined resolution depending on the width of the bar (Fig. 2.9 left). The resolution can be enhanced by triangular shape (Fig. 2.9 right) which are slightly more complicated to produce, but this way a passing particle affects two bars, and with a center of gravity algorithm, the position can be fine-tuned.

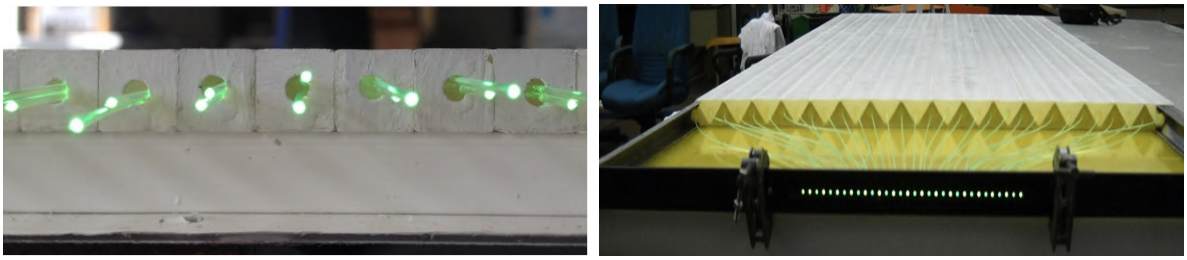

Figure 2.9: Examples for scintillation plastic shapes used in muography. Left: square cross-section bars with wavelength shifting optical fibres (WLS) guiding the light to a position sensitive PMT (MEV project, University of Catania [60]). Right: triangular bars with WLS guiding the light to SiMPs (Mu-Ray experiment, INFN-Napoli [61]).

Emulsion detectors: The nuclear emulsion solid-state detector is a special type of the well known photographic emulsion film with monodispersed silver halide crystal grains. Charged particles passing through a nuclear emulsion leave tracks by interacting with the grains, and after the chemical development of the emulsion layer (below 100 µm thickness), particle tracks can be identified with an optical microscope scanner (Fig. 2.10). Track reconstruction is carried out by focusing to multiple depth in one emulsion layer, and a laminographic image processing recognises the related points of a so-called microtrack. Different microtracks in different layers are connected, eliminating the background noise in the images and providing exceptionally high position resolution (micrometers).

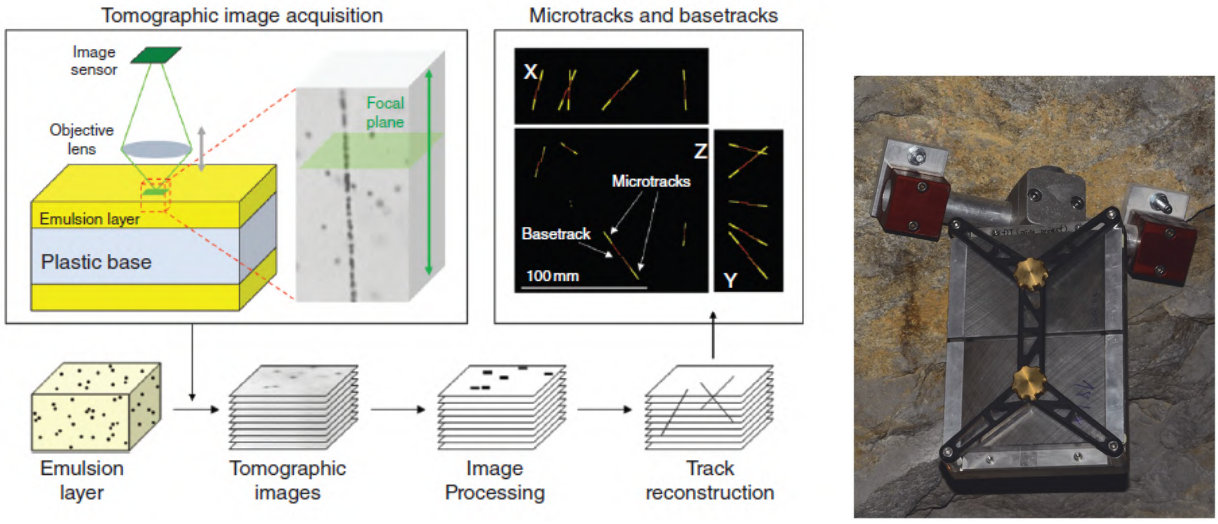

Figure 2.10: Left: Process of emulsion scanning and track reconstruction [62]. Right: Photo of an emulsion detector [63].

Emulsion technology provides passive detectors, which means that tracking is not real-time, in exchange they have zero consumption in the field. In practice, layers are produced in a lab, transported to a measurement site, exposed to the cosmic rays in a viewpoint, transported back to the lab, developed, and the muographic data is available after the scanning of the

Table 2.1: A comparison of detector technologies for some design parameters [3, 49].
* High one-time investment for the optical scanner and production line system, but low film production cost.

	Gaseous detectors		Scintillators		Nuclear emulsion
	MWPC	MPGD	rect.	triang.	
Resolution	1–10 mm	0.1–1 mm	10–20 mm	1–5 mm	0.01–0.1 mm
Monitoring	Yes	Yes	Yes	Yes	No
Weight	Medium	Medium	High	High	Low
Cost	Low	High	Low	Medium	High capital*
Production intricacy	Moderate	Complex	Easy	Moderate	Easy
Consumption	Power, Gas	Power, Gas	Power	Power	None

layers. In consequence, the layers are exposed to the cosmic rays also outside the measurement site resulting in unwanted extra background. The solution for this problem is that detector layers (each contains a double emulsion layer with a plastic base and aluminum coating for protection) are transported separately to the site, and at the beginning of the measurement, at least two detectors are aligned to each other. At the end of the measurement the detectors are detached, therefore the coupling of tracks in the different detectors provides the muographic data collected only in the viewpoint.

Tab. 2.1 summarizes a comparison between the three main detector families (and some of the sub-types). The comparison provides a relative estimation between the technologies for some basic requirements such as position resolution, weight, cost, and consumption.

There are many more particle detector technologies besides the above mentioned ones, but those are not so common in muography. Nevertheless, two more detector families may be worth mentioning as those have been applied in muography so far. **Cherenkov detectors** utilize the Cherenkov photon emitted by the high-energy charged particle when passing through a dielectric medium (at a speed greater than the phase velocity of light in that medium). It is possible to use it directly for tracking [64], but the most promising application is background filtering [65, 66], combining it with some of the conventional technology for tracking [17]. Another type is the **semiconductor position-sensitive detector** (e.g., silicon micro-strips or pixels) which has potentially very high resolution, and could be useful in high radiation, compact environment, or space applications [67]. Generally, these alternative methods have much higher cost per sensitive area ratio and therefore are very expensive for muography since the size is an important factor, but still can exist thanks to the fundamental scientific experiments.

2.3.2 Surface detectors and background suppression

Due to the fact that cosmic-ray induced muons are produced in the upper atmosphere, the detector must always be placed on a lower altitude than that of the target. Therefore, the detector is often placed underground (under the examined region), or on the surface by viewing the upper part of a protruding object from the side (see, for example, in Fig. 2.11). In the latter case, usually the environmental stress is an important challenge, like the daily and yearly temperature variation, or storms (humidity, wind, dust, lighting, etc.) [68]. Some protection against storms can be achieved by a proper shielding such as placing the detector in a container or a tent. It is more difficult may be to protect against temperature which can cause stability issues. Preparing the detector to tolerate very high temperatures (>40°C [69]) could pay off in the long-term due to the simplicity and cost efficiency (but of course heat exchanger can be an option too if sufficient power is accessible).

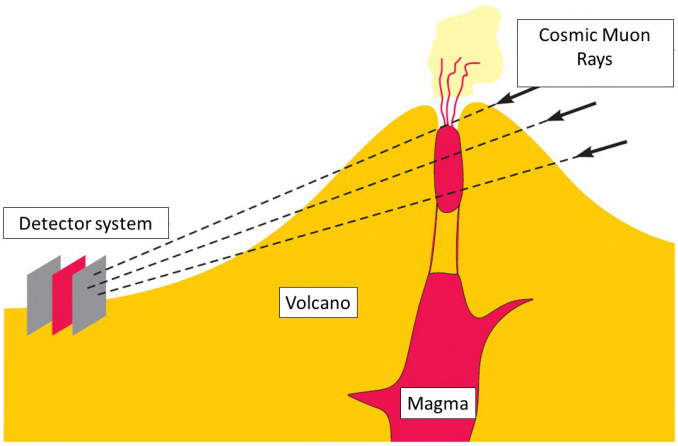

Figure 2.11: Schematics of surface measurement in case of a volcanological application [70, 71].

The most important issue on surface is the high rate of background particles originating from cosmic radiation and mimicking high-energy muons, which actually do not pass through the examined object but result in fake tracks in the detector, blurring the muographic image. This "high" rate is an elusive concept and depends on many things (the number of detector layers, zenith angle, topography, altitude, solar activity, temperature, etc.), but the level of background can be quantified by the minimum flux value which can be measured by the detector. Since the muon flux and density-length are inversely correlated, this value basically provides a maximum rock thickness which can be imaged (with an estimated average density). Measuring this value is simple: since we expect essentially zero muons from the horizon or in the direction of very large rock thicknesses (>1 km), the muon flux from this direction is the level of background. Without any background suppression, this level (translated to rock thickness) could be even below 100 m, so a sufficient background filtering can be a key factor for imaging larger rock thicknesses.

To suppress this background as much as possible, we must first understand its origin. High-energy muons traversing through the examined object leave straight line tracks in the detector as described in Sec. 2.2. However, there is a large portion of low-energy particles (<1

GeV) on the surface of the Earth, such as hadrons (protons, neutrons, pions, etc.) and leptons (electrons, positrons, and low-energy muons) originating from the primary cosmic rays. Most of these particles are usually absorbed or scatter even in thin layers of material such as the detector walls, but there is a finite probability that, despite scattering and absorption, some particles are still able to leave a straight line in the detector.

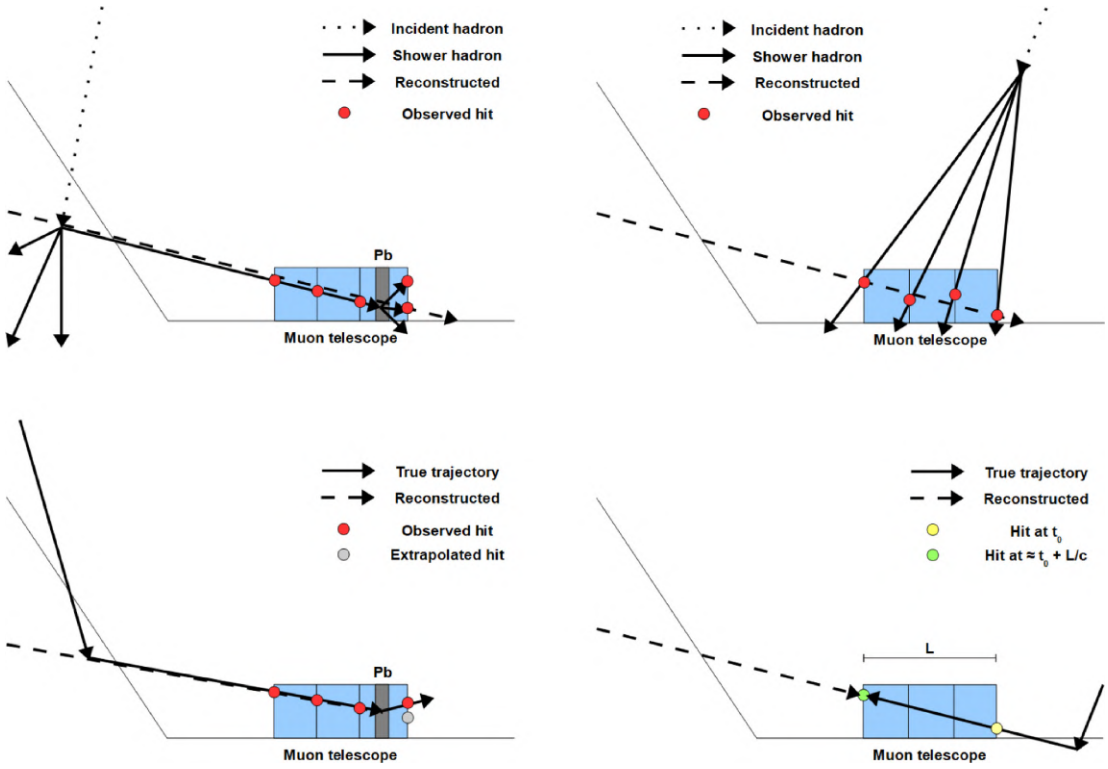

Figure 2.12: Four cases of possible muographic background. Top left: hadrons creating new particles in front of the detector. Top right: cosmic shower creates straight-line coincidence event (combinatorical background). Bottom left: low-energy muons scatter in the detector from the object. Bottom right: low-energy muons scatter backward [3].

Some possible scenarios are outlined in Fig. 2.12. The dashed line represents the reconstructed track which mimics a high-energy muon travelled through the examined object. Four cases are usually examined in muography:

1. hadrons reaching the surface and producing new particles in the direction of the detector view (top left),

2. different components of a hadronic shower accidentally imitating a straight track (top right),

3. muons scattered into the detector in front of the object (bottom left),

4. muons scattered backwards up in the detector to the direction of the object (bottom right).

In case 2, the more detector layers we have, the smaller the chance for this combinatorial background. The 1, 3, and 4 cases are basically intermediate energy particles (0.1–1 GeV [72], or in some cases even up to 5 GeV [73]) which have enough energy to leave a straight line in the detector. The most effective (simple and cost-efficient) protection against them is a scattering/absorbing wall (usually made of lead) between the tracking detector layers which alters the path of these intermediate energy particles [74]. The exact energy cut depending on the thickness of the scattering wall can be derived from detailed simulation studies. However, a consequence of this protection is that this way every particle is effected, even the originally high-energy muons which attenuated to an intermediate energy during the travel in the examined object. Thus, we lose some portion of the useful signals as well. This is usually a tolerable loss since the integral of the muon spectrum in this region is much smaller than the rest of the integral of the spectrum. Another issue could be the high weight of the scattering wall, reducing the portability of the detector. There are alternative methods to reduce the background, e.g., Cherenkov detector application for energy measurement, or a time-of-flight (TOF) measurement to distinguish backward going muons. [75].

2.3.3 Underground detectors and their requirements

If there are artificial tunnels or natural caves are available under the examined object or rock layer, it is advantageous to collect muographic data from those places, but this underground muography has its limitations. The choices for viewpoints are constrained by the accessible area, and the environment is often not friendly there too, although arise different challenges than those on the surface. Two examples of underground detectors installed in a cave and a tunnel are shown in Fig. 2.13.

Figure 2.13: Examples of muon detectors installed underground. Left: Photo taken in the Ajándék cave near Budapest, which is a good example for humid environment. Right: Installation in the Esztramos abandoned mine system in Hungary, which illustrates well the limited space and the importance of portability [30].

Extreme temperatures are rarely a problem underground and the temperature is usually constant, but humidity (or even water droplets) and dust are frequent issues for which the detector must be prepared for. The required level of protection depends on the site, since each site has different environmental parameters, such as temperature, humidity, and pH level. The IP54 standard[2] is sufficient in most cases. Power supply can also be an issue if the location does not have electricity. In this case, low power consumption could be mandatory and the battery charging or replacement can be challenging. It is worth noting, that the application of a solar panel near the entrance of the underground facility can be simple and reliable if the detector is not too far (150–200 m) from the entrance.

Borehole detectors are a new technological frontier in underground muography [76, 77, 78, 79]. Boreholes are artificially drilled holes (around 5–30 cm in diameter) cutting through the rock sequence with up to kilometers of lengths for geoscientific examinations (rock composition, temperature, etc.), mineral exploration, or resource extraction (water, gas, or liquid hydrocarbons). Since this provides direct information about the geology, it is a widely used but remarkably expensive survey method compared to other indirect non-destructive methods like gravity, seismic surveys, magnetic surveys and electric resistivity etc. Regarding geophysics, the commonly used strategy for mineral exploration is to start with the cheapest and easiest method which usually has low resolution, and progress in the direction of more expensive methods with higher resolution, ending with multiple borehole drills. Muography could be included among the traditional methods, providing the highest resolution around a given borehole, and reducing the required number of boreholes.

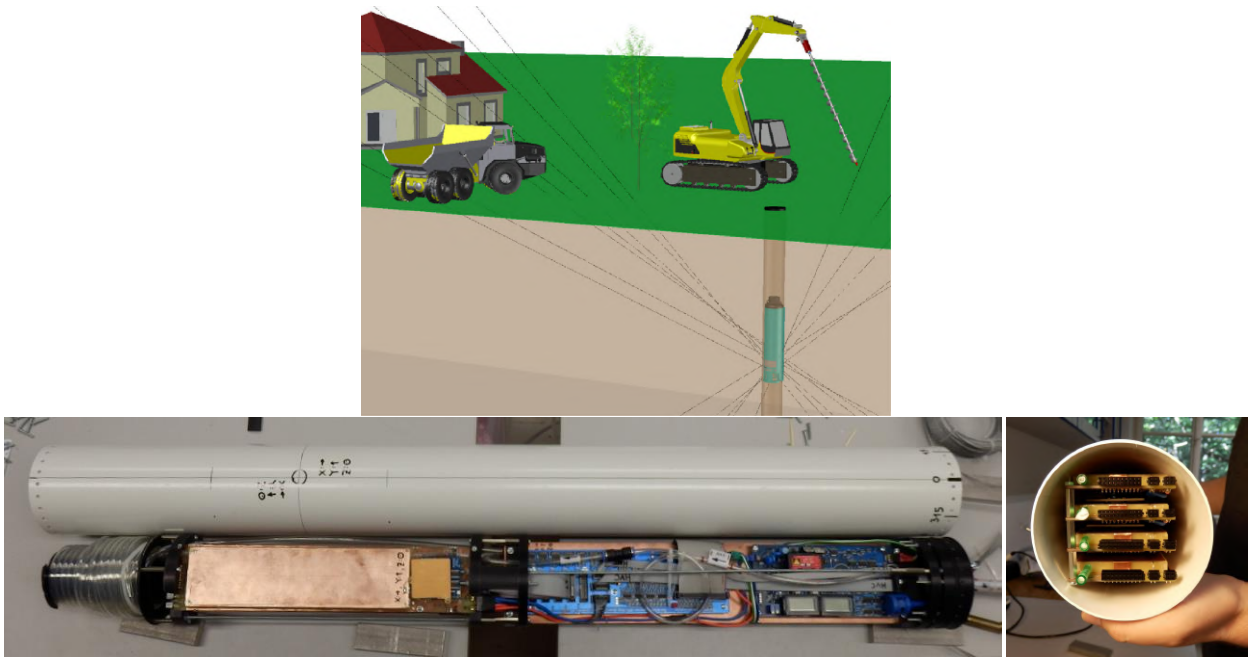

Figure 2.14: A schematic example is shown on the top figure for borehole detector application [3]. The photos at the bottom show the 10 cm diameter prototype of a gaseous borehole detector developed by the REGARD group [30].

[2]International standard of ingress protection (IP) code: iec.ch/ip-ratings (Accessed: 2023-05-30)

Chapter 3

Gaseous detector developments for muography

3.1 Innovative Multi-Wire Proportional Chambers

Close Cathode Chambers: Our research group in the Wigner Research Centre for Physics has been developing gaseous detectors for fundamental research, and applications like muography for more than ten years. One of the new designs was the reconsideration of the classical MWPC detector. Motivated by designing a detector for the proposed ALICE Very High Momentum Particle Identification Detector (VHMPID) [80], the Close Cathode Chamber (CCC) [81] has been developed. The detector concept appeared to be an ideal choice for application in the emerging science field of muography as well due to its excellent stability, resolution, and cost-effectiveness attributions [82]. The CCC technology is still present in our detector supply although it is beyond the scope of this dissertation. However, a short introduction is needed to understand the origin and motivations of the advanced MWPC detector technology which is the main scope of the present work.

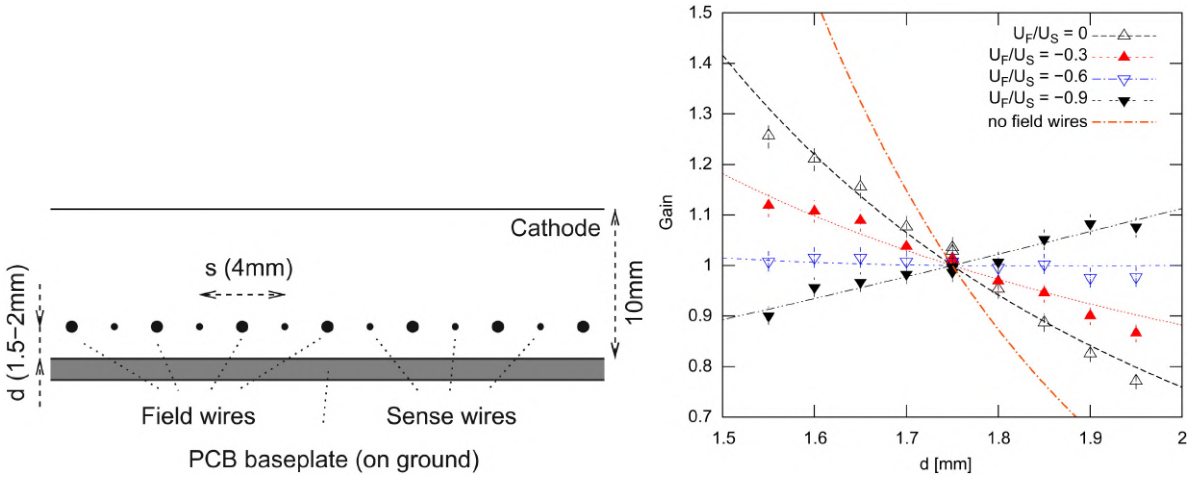

Figure 3.1: Left: Schematic cross section of the CCC detector concept. Right: Relative gas amplifications as a function of lower cathode and wire plane distance d with different U_F/U_S voltage ratios normalized at d = 1.75 mm [81].

The wires in the Close Cathode Chamber are not symmetrically centered – as the name suggests – but closer to one of the cathodes (see Fig. 3.1 left), unlike in the conventional MWPCs. This results in a sharper charge distribution of the passed ionizing particle. The closer cathode has copper 'pad' strips (typically 4 mm wide, created by conventional PCB etching) for providing one coordinate, and the perpendicular wires (specifically the Field wires, ∼100 µm diameter EDM wire) provide the second coordinate of the passed particle, resulting in 3–4 mm FWHM position resolution in both directions [82]. The Sense wires are the anodes (20–25 µm diameter gold-plated tungsten wire). The position resolution can reach even 200 µm FWHM with 2 mm pad width and analog position channel readout if required [83].

Classical MWPCs have a notorious problem with stability and homogeneity of the *gain*, a.k.a. the gas amplification, that is, the number of electrons after the development of the Townsend avalanche which sparked by one primer electron. The gain is very sensitive to the geometry: the wire distances to the cathodes and to each other. Hence, the wires must be stretched to the limit in order to avoid instabilities. Thus a massive chamber wall structure is needed, and the wires can easily break. The most important innovation of the CCC technology is that the ratio of the Field and Sense wire potential (U_F/U_S) has been optimized againsts the wire–cathode distance (d), and such a ratio has been found where there is no dependence from d (Fig. 3.1 right). This means that the gain is not sensitive to small geometric deformations and therefore there is no need for heavy frames or intensive wire stretching, and the detectors are less sensitive to transportation or mechanical influences. Even 1 m × 0.5 m size detector chambers have been demonstrated [83].

In summary, the CCC technology combines multiple ideas, which work efficiently together and provide solutions for a number of typical MWPC problems:

- Field wires are applied to stabilize the electric field.
- Ar:CO_2 mixture of 82:18 (commercial Ferroline C18) non-flammable, non-toxic, non-aging gas can be used, since there are no special issues to overcome which is common in other gaseous detector technologies.
- The position information is collected in the Field wires (instead of the Sense wires, which is the general method). This way the signal is very similar to the pad signals and similar electronics can be used for both coordinates. Furthermore, the Sense wires are coupled together, and provide a good quality trigger signal for the Data Acquisition (DAQ) system.
- Field wire and pad signals are converted to 1 bit information and a shift register circuit collects them to a single board Raspberry Pi mini computer. ADC information from each channel would enhance the resolution by more than a factor of 6 [83], but the power consumption and cost would be significantly higher, not to mention the more complicated DAQ system.
- Cathode planes can be commercial PCB (instead of foils), made from FR4 material with copper surface, since material budget is not an issue in muography. This gives extra robustness and cost-effectiveness to the system.

Photos about the CCC detectors are shown in Fig. 2.6 in the previous Chapter. This detector technology has been performed successfully in a wide range of applications so far. The beautiful Hungarian caves were one of the first muographic field trials to develop robust, autonomous, and mobile detectors, which are able to resist high humidity and mechanical stress of transportation [29]. These detectors were installed in the Molnár János cave (Budapest, Hungary) and in the Ajándék cave (Pilis mountains, Hungary) where no significant unknown cavities have been found. A further measurement has been performed in the historical limestone mine of Kőbánya (Budapest, Hungary) where a known blowhole shaft has been examined. In each case, the measurements have been verified by comparison with the surface topography. A detailed verification of muographic cavity measurement in the Jánossy Pit underground laboratory in the campus of the Wigner RCP also has been carried out [84]. The muon intensity in the Felsenkeller shallow underground laboratory (Dresden, Germany) has been investigated by studying the muon induced events, background, and for planning an active veto of accelerator-based underground nuclear astrophysics experiments [85]. A proposed next generation ground-based gravitational detector's location has also been examined in combination with seismic and infrasound noise, electromagnetic attenuation, and cosmic muon radiation measurements in the underground Mátra Gravitational and Geophysical Laboratory near Gyöngyösoroszi, Hungary [86].

Advanced Multi-Wire Proportional Chambers: In muography applications, it is clear that one of the main detector requirements is the size (active area) since the muon rate is relatively low. Thus, to collect sufficient statistics in a remote field, it is not only important that detectors are stable for long periods of time, but they must also maximize the detector area which fits to the measurement location (keeping in mind the portability). Based on the experiences with the CCC detectors, the need arose for large-size, cost-efficient, and mass producible detectors. It is also worth mentioning, that with increasing detector size, the target object is usually also larger, and since the detector should be considered to be point-like, the position resolution is also allowed to reduce. To satisfy these needs, the following ideas helped to develop a new, advanced MWPC design in addition to the CCC ideas:

- Sparser wire spacing, symmetric cathode-wire-cathode planes, and larger ionization length (2 cm gas gap): if there is more distance between the wires and the cathodes then the gain stability requires no geometric asymmetry.
- Field wires on ground potential: since the new design is expected to be sufficiently stable, reducing the number of high voltage channels greatly simplifies the power supply and electronics, the MWPC geometric sensitivity has been tested with Field wires (also as the Pads and the cathodes) on ground potential (Ref. [83]).
- Pick-up wires: pads are thick wires instead of copper strips. Since PCB etching in large size is problematic, replacing the cathode strips with wires (practically using the same type of wires as for the Field wires) is much more convenient.

The schematic structure of the advanced MWPC design is shown in Fig. 3.2 (from now on, 'MWPC' refers to this design). The top and bottom figures show two perpendicular cross sections. In large chambers, the cathode surface flatness is supported by 3D printed pillars.

In the middle of the gas volume, the 100 µm Field wires (ground potential) and the 20–25 µm Sense wires (anodes) are stretched with a 6 mm spacing between each other. The Pick-up wires (100 µm on ground potential) are located 2 mm from the bottom cathode plane. The anodes are interconnected and are typically around +1700 V high-voltage potential, around which the electron avalanche (gas amplification) forms, and provide the trigger and amplitude measurement for readout as mentioned before. The Field and Pick-up wires provide the x and y coordinate information of the passing particle. The Pick-up wires have 4 mm spacing and connected in groups of three, thus the segmentation pitch is the same as for the Field wires.

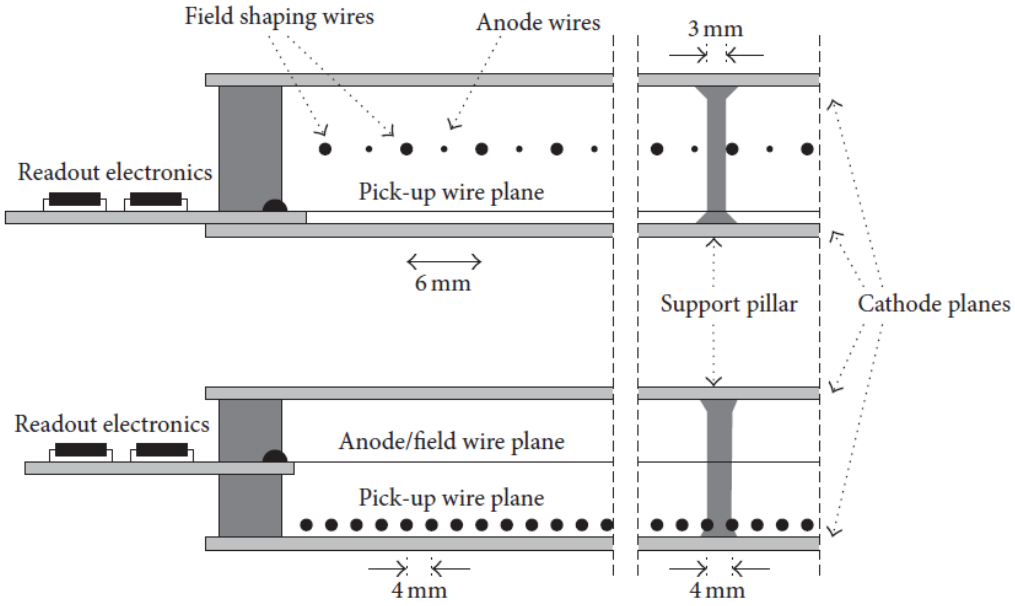

Figure 3.2: Perpendicular cross section view of the advanced MWPC design, showing the geometric configuration of the structure and the soldering points between the wires and the readout electronics [87].

From the Sense wire signal, two output signals are formed (after preamplification and shaping). One is a direct analog output for amplitude measurement, and the other is a TTL-compatible (Transistor-Transistor-Logic) discriminated trigger signal, which are forwarded to the DAQ. The trigger signal is created only when the amplitude reaches a certain level of threshold, with a 2 µs delay timing to the mean maximum of the signal. Each chamber provides a trigger signal for the DAQ, and if a predefined number (usually 3 or 4 out of 6–8 chambers) of signals appear in coincidence, the DAQ start the readout of all the Field and Pickup channels. This way a large portion of possible noise or background event is eliminated. A photo of the DAQ system and the Front-End electronics is shown in Fig. 3.3, all of them custom designed (except the minicomputer) and developed by our research group for muography purposes. The hearth of the DAQ is a Raspberry Pi (RPi) minicomputer running a debian based linux kernel. Thus, compatibility, access (SSH, Wi-Fi), file operations, and programming (C, C++, Bash) are simple. The GPIO (General-purpose Input/Output)

pins are custom programmed to communicate with the DAQ Board, and through that, all electronic components. The main data stream is a synchronous parallel readout of several data-lines, mostly containing the 1-bit info of the channels stored in shift registers, while all other devices (ADC, THP sensor, high voltage supply unit) use a similar scheme with specific decoding. The analog amplitude signal is also digitised via 10 bit ADCs. The total data stream during an event is only around 100 bytes, and since the cosmic event rate is usually well below 100 Hz, we are able to use a simple, low-power RPi computer. The dead time for the total DAQ readout of an event – during which the system is not able to record another event – is below 400 µs, which is acceptable at this event rate. The rate capability has been checked with a 3.5 kHz ^{90}Sr source irradiating the detector on a spot of about 20 cm^2 area, whereas the cosmic event rate corresponded to 0.2 Hz/cm^2, and no tracking efficiency loss has been observed [87]. In the present work, the background and noise performance have also been checked by comparing the real event trigger rate with a 110 Hz random oscillator triggered data, concluding that pure electronic noise is negligible (below 10^{-6}) and background rate is four orders of magnitude below the true event rate.

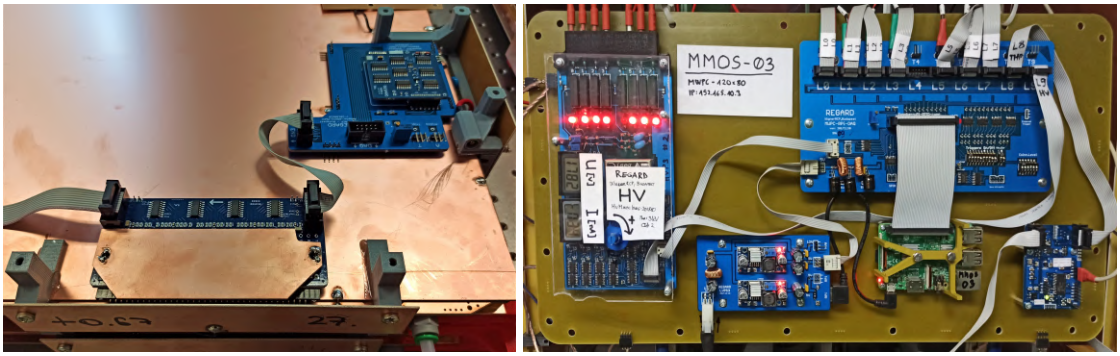

Figure 3.3: Left: Photo of a 32-channel digital front-end card and an ADC card attached on an MWPC. Right: Photo of the DAQ system, containing the HV-unit, DAQ Board, DC-DC converter, RaspberryPi, and a THP (Temperature-Humidity-Pressure) sensor.

A MWPC tracking system usually contains 6–8 chambers, each providing two dimensional information of hit patterns for each event. In most cases, the traversing particle affects several adjacent channels. These groups of hits are called clusters. The size of these clusters depends on many factors (angle, energy, gas amplification, background, etc.), but after a sufficient filtering, the true location of trajectory intersection is expected to be at the center of the cluster. Therefore, the muon tracking algorithm takes into account all the cluster centers in both dimensions, and fits a straight line by the least square method. This recorded track is also checked for straightness by Chi-squared test to filter out low energy particles, which suffered multiple scattering inside the detector (as described in Sec. 2.3.2). The tracking data are also used to continuously monitor the performance of the chambers. When a well defined single track is found, excluding any chamber from the tracking can be used to check the efficiency of the excluded chamber. This allows for the evaluation of efficiencies related to triggering, or tracking (detecting a hit or a cluster), which may vary based on time or location. Performance plots showing the 2D tracking efficiency and time dependent parameters are shown in Fig. 3.4.

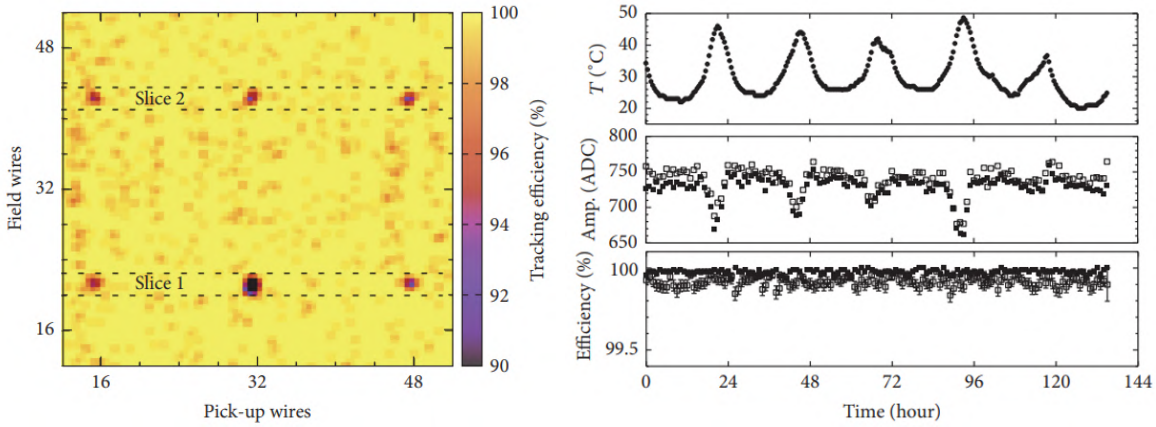

Figure 3.4: Left: Track hit location dependent efficiency of an MWPC chamber, where the effect of pillars can be identified (note the scale starts from 90%). Right: Time dependent parameters during an outdoor measurement, with temperature (top), amplification gain (middle), and tracking efficiency (bottom) [87].

The gain also provides significant performance information, which is highly sensitive to the gas quality and the electric field around the Sense wire. The gain is measured as the mean of the signal amplitude for identified tracks. The high voltage is well regulated, a slight deviation occurs only at high temperatures (above 40 °C, see details later). The gain also depends on the density of the gas (temperature and pressure). At a given high voltage and constant environmental parameters, the gain only depends on the gas purity, since gaseous detectors in general are very sensitive to any electronegative molecule which can capture the ionized electron (oxygen, water vapor, etc.). In order to understand the sensitivity of the MWPC, a study has been performed with the injection of ambient air in the gas system. Five chambers have been used, and the gas (Ar:CO_2 mixture with respective ratios of 82:18) serially flows from Chamber 1 to 5. Prior to the measurement, the system has reached a stable equilibrium of every performance parameter at 1 l/h gas flow rate at 1 atm. At the beginning of the study, 166 cm^3 air has been injected into the gas line between Chamber 1 and 2. Fig. 3.5 shows the gain change relative to the first detector layer which quantifies the effect of air contamination.

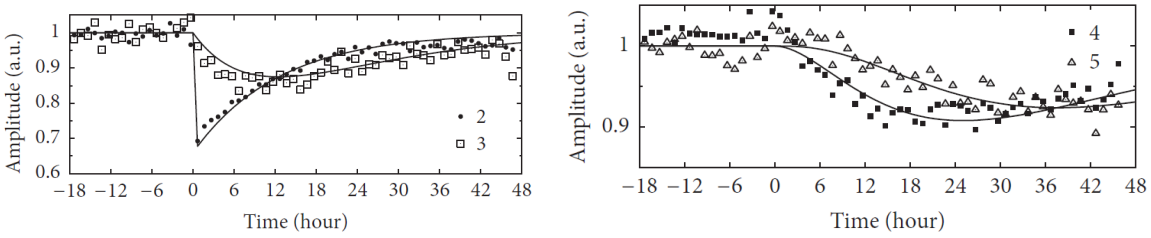

Figure 3.5: Relative gain (mean signal amplitude) of detector layers in the air contamination study, where the amount of injected air was 1.3% of the volume of one chamber at $t = 0$ before Chamber 2. The numbers in the legend refer to the number of the chamber. The contamination propagates and cleans out exponentially in time, and the predicted functions are indicated as solid lines [87].

The pattern follows a clear exponential function in time, and the propagation of contamination into the consecutive chambers is also predictable [87]. It is also worth noting that the tracking efficiency did not drop at all during the entire measurement. This means that even the 34% gain drop – as with the Chamber 2 at the beginning – is tolerable, and that corresponds to 1.3% air contamination (or 2500 ppm O_2).

From the above, we conclude that these innovative gaseous detectors fulfill the most significant requirements for muography and those can be summarised as:

- large sizes besides portability at a sensible cost,
- robustness (mechanical, environmental) and stability for long term outdoor operation,
- high tracking efficiency with low noise and background,
- sustainable and safe operation with low gas and power consumption.

Simplicity is proven useful for education purposes as well [88]. From high school to university level students can join and experience research and development of the advanced MWPC technology and muography, take part in the construction, and conduct laboratory experiments with these devices.

My work in the REGARD group also started as an intern during university studies, evolved and completed into the present dissertation. In the following subsections, my research is explained in detail, focusing on the developments achieved in the MWPC technology. The next subsection discusses the achieved construction methodology and developed components which contributed to the effective production, robustness, and stability of the large size MWPC detectors. Subsection 3.1.2 describes the wide range of detector assembly variations and resolution studies for the different types of demand arising in the muography field. Subsection 3.1.3 and 3.1.4 demonstrate the low gas consumption and stability in harsh environments, with dedicated test measurements as well as in real remote field surveys. Finally, in subsection 3.1.5 I demonstrate the result of MWPC developments on application examples.

3.1.1 Construction

Unfortunately MWPCs – and in general, gaseous detectors – cannot be purchased from the market and this is probably one of the most important disadvantage compared to other detector technologies. However, since they are developed in research laboratories, the hardware can be easily adapted to specific scientific purposes. I developed a cost and time efficient construction methodology of the advanced MWPC chambers, which consequently have already been produced for more than 300 copies in four different size variations so far. The growing number of applications demanded to increase the production, for which the Vesztergombi laboratory complex has been established. Now around half m^2 detector per month can be produced and this capacity can be increased if necessary. The applications are summarized in Chapter 5, focusing on the projects where I also participated in addition to the detector development contribution.

Construction methodology: A chamber is constructed mainly out of fiberglass: G-10 glass fiber reinforced epoxy sidewalls, FR-4 cathode planes and printed circuit soldering point

components. All components are jointed together by two-component epoxy glue (Uverapid-5, or similar), taking care of the outgassing and electric resistance properties of the glue. This ensures gas tightness and similar thermal behaviour between the components (i.e., no mechanical tension in case of temperature cycling) due to the similarity of the material basis. Given the relatively large area, the distance between the cathode planes must remain at the nominal 22 mm with reasonable precision. In order to achieve this, I designed 3D printed support pillars which are glued between the wires, as demonstrated in Fig. 3.6 above, in a pattern to minimize plate bulging. These pillars, made out of insulating and non-outgassing material (ABS), do not touch any of the Field and Sense wires. The pillars were placed closer to the field wires, with around 0.5 mm clearance, which leaves approximately 2.5 mm distance from the Sense wire. The field lines still terminate on the Sense wires near a support pillar, therefore the detector remains sensitive to the traversing particles, with only tiny local tracking efficiency loss around the pillars, as shown previously in Fig. 3.4. Construction takes place on an optical table to ensure precise joints, and surface flatness.

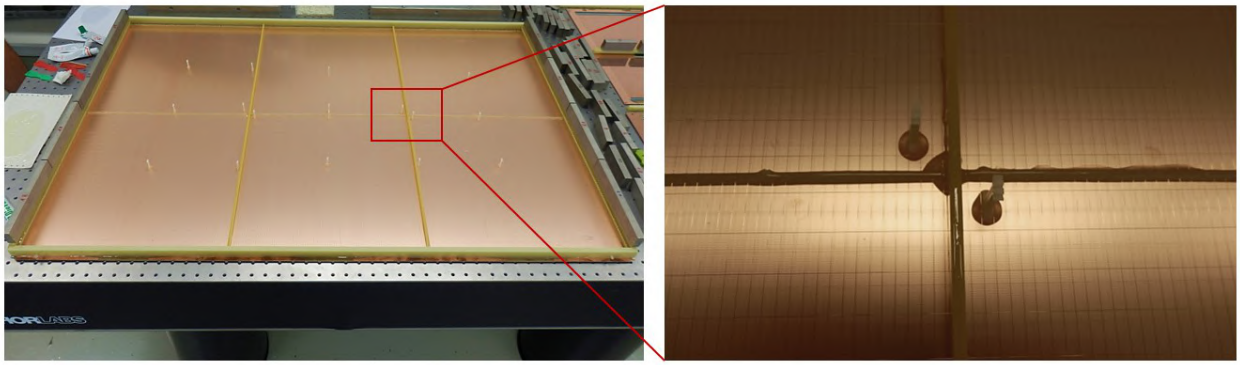

Figure 3.6: Left: an open large-size (120 cm × 80 cm) detector chamber under construction on an optical table, showing the inner structure – pillars and wire supports – before closing with the upper cathode plate. Right: zoom into the chamber, showing the main support structures and wires (Field and Sense wires run from left to right) [89].

Taking into consideration the relatively long epoxy glue hardening time (12–24 hours) and the time requirements of the work processes, I considered the following easy to track work steps:

0. *Parallel processable works:* preparing the epoxi rods (sanding, cleaning, jointing the gas connectors and soldering circuits), 3D printings, and cables (data, trigger, high voltage, ground, etc.).

1. *Base plate construction:* gluing the first layers of soldering circuits, wire supports, and epoxy walls.

2. *Pickup wire plane construction:* positioning and fixing the base plate to a custom designed wire stretching device, then winding the wires (Fig. 3.7 left); soldering the wires and cutting off the wire parts that overhang the detector; gluing the next layer of soldering circuits and epoxy walls.

3. *Sense and Field wire plane construction:* repeating the previous steps with a different wire distancing (12 mm separately for the Field and Sense wires).

4. *Closing:* gluing the last epoxy walls, and the 3D printed pillars; gluing the top cathode plate.

5. *Final preparations:* mounting the readout cards, connectors, groundings, shieldings (Fig. 3.3 left).

6. *Tests, calibrations:* testing gas tightness, high voltage; trigger level calibration; Tracking and outgassing test.

The steps outlined above are grouped into more or less one-day jobs, leaving time for glue hardening at nights. The work can also be shared with multiple technicians for time-saving, cross check, and the parallel construction of multiple chambers. Each time two chambers are built simultaneously with one wire stretching system by fixing a base plate to each side of a wire stretching frame.

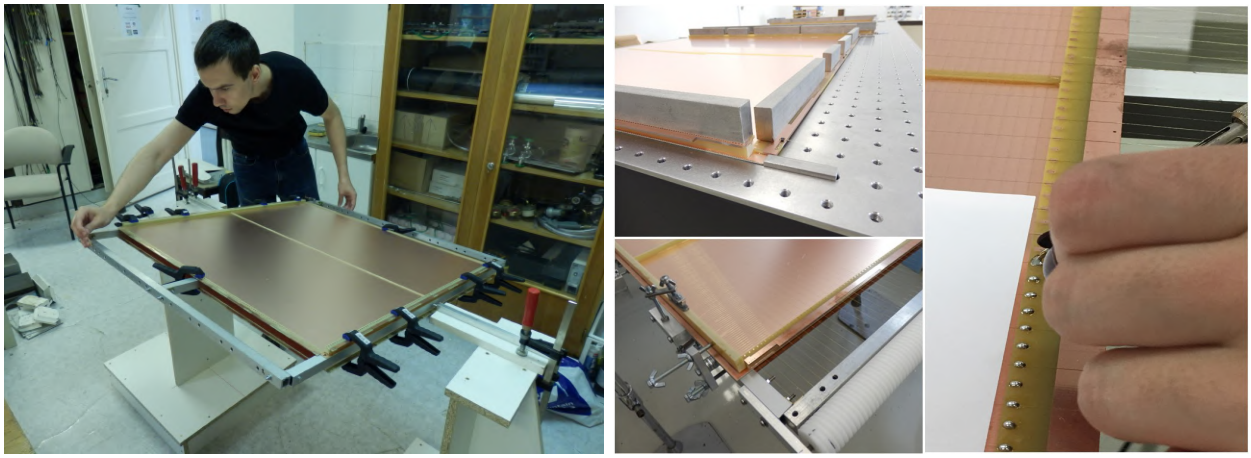

Figure 3.7: Photos of the main construction steps. Left: the first prototype of wire stretching and winding during usage. Top center: gluing, weighting down, and positioning the components on top of an optical table. Bottom center: positioning and fixing the prepared plate to the wire stretching frame. Right: soldering the wires to the circuits, and later the overhanging part of the wires are cut off.

Chamber size variations: Different muographic applications may benefit from different sizes of detectors. In surface muography, the size is generally not limited. Thus, larger sizes are advantageous, meanwhile underground applications require smaller and portable detectors. Maximizing the size is also an aspect underground, but usually the available space is the limitation, e.g., in a mine tunnel even cubic-meter detector could fit, but archaeological or natural underground passages usually allow much smaller dimensions. In the REGARD group, we developed four MWPC chamber sizes so far to cover as many application fields as possible.

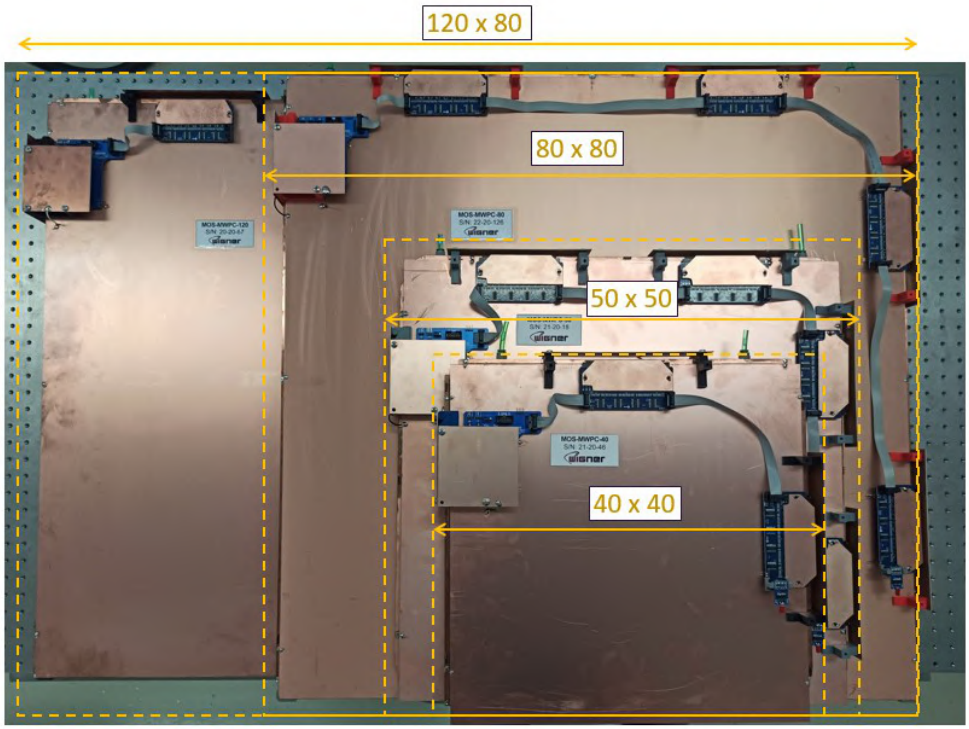

Figure 3.8: Photo of the four size variations of the advanced MWPC chambers.

The 80 cm × 80 cm size variation (abbreviated 'type 80') was the first in historical orders [87]. The segmentation of the wires is 12 mm, connected to an electronic readout channel. One custom designed readout card (current version called DIN632) can handle 32 channels. This chamber variation is equipped with two readout cards on each side. Production experience allowed us to expand the next generation to 120 cm × 80 cm (3 × 2 readout cards 'type 120'), and a small version with 40 cm × 40 cm size (1 × 1 readout cards 'type 40') was also developed for laboratory tests, both with 12 mm segmentation. Practical demands arose to develop a 50 cm × 50 cm version with 9 mm segmentation (2 × 2 readout cards 'type 50') for underground and civil engineering applications, where the size can be a limiting factor but good resolution is needed. The above mentioned chamber variations are shown together in Fig 3.8. For comparability, the properties of the different MWPC chamber variations are summarized in Table 3.1.

Table 3.1: A summary of the main properties of the different MWPC size variations.

	40 × 40	50 × 50	80 × 80	120 × 80
Outer dimensions	$(42\ \text{cm})^2$	$(59\ \text{cm})^2$	$(82\ \text{cm})^2$	$122 \times 82\ \text{cm}^2$
Sensitive area	$0.15\ \text{m}^2$	$0.33\ \text{m}^2$	$0.59\ \text{m}^2$	$0.88\ \text{m}^2$
Volume (inner)	3.35 l	7.3 l	13.2 l	19.8 l
Weight (gross)	2.7 kg	3.1 kg	6.3 kg	11.2 kg
Segmentation	12 mm	9 mm	12 mm	12 mm

Developed components and supplementary instruments: In the following paragraphs, some of my mechanical developments are presented regarding to the effective production and applicability of large size MWPCs. The creative work includes the designing, manufacturing, assembling, testing, and commissioning.

The wire stretching system consists of a chamber fixing frame and a wire dispenser spool. The operation scheme is shown in Fig. 3.9 left. Before winding a layer of wires, two chambers are fixed to an aluminum frame with bearings and stands for rotation. The frame is carefully designed for simple installation to reduce possible errors, and adjustable positioning with guiding grooves to precisely aim the wires to the soldering points (Fig. 3.9 right). The wires must be stretched with a unified force – which is necessary for the homogeneous electric field strength inside the chamber – in such a way that the wires do not break during transport or high thermal expansion. The fracture of the 100 µm brass EDM wire occurs at a load of around 410 g, and the 20–25 µm tungsten wire around 90 g, but much lower tension is enough for gain homogeneity: 80–100 g and 15–20 g, respectively. Before winding, the EDM wire is also cleaned and spooled over to a smaller spool, attached to a DC motor which provides the consistent stretching force. This process is semi-automated by a custom designed wire dispenser system which is shown in Fig 3.10.

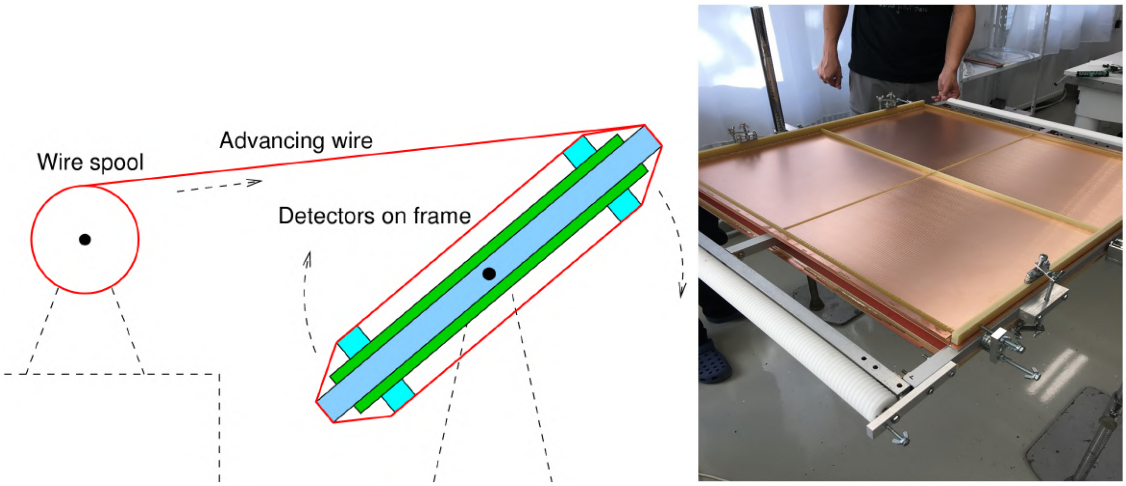

Figure 3.9: Left panel shows the scheme of wire stretching [88]. On the right, the developed chamber fixing frame can be seen with type 80 chambers under construction. The device provides simple installation and precise wire alignment, and also functions as a soldering station.

I introduced 3D printing technology to the research group which proved indispensable ever since. We use Zortrax machines[1] which apply Layer Plastic Deposition technology: depositing melted plastic material layer by layer onto the build platform. In most of our applications, the material is an ABS (Acrylonitrile Butadiene Styrene) blend, namely the Z-Ultrat [90], which is generally a durable thermal and electric resistive filament. 3D printing of the components is not only useful for rapid prototyping, but takes advantage of the ability to produce very complex shapes or geometries that would be otherwise infeasible to construct

[1] https://zortrax.com/ (Accessed: 2023-05-30)

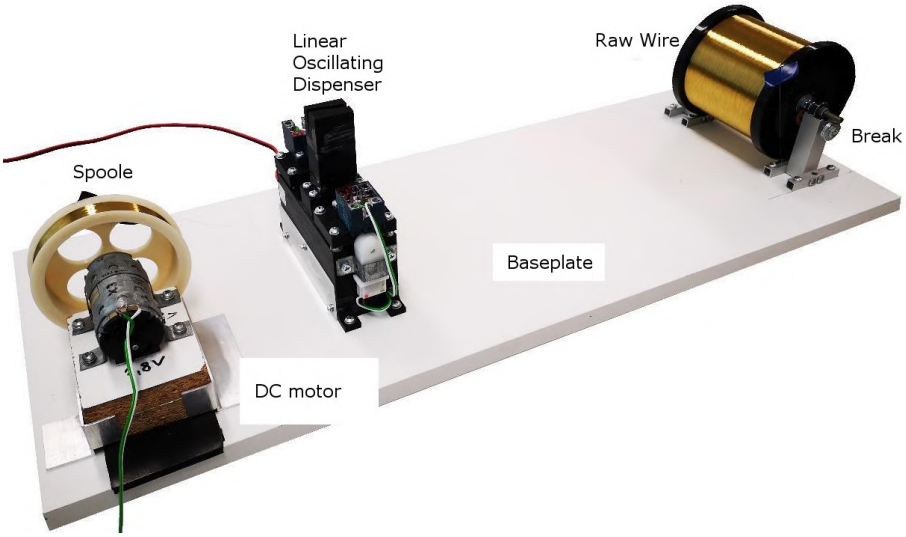

Figure 3.10: The components of the wire dispenser system (figure from László Tercsi).

by any subtractive manufacturing. Therefore, multifunctional tools can be created to meet special needs. The positioning precision of the nozzle is 1.5 µm and the resolution of the extruded material is 90–300 µm. Thus, the quality enables us to use these components in a wide range of mechanical applications even in harsh environments. Some of these 3D printed designs are shown in Fig. 3.11, containing alignment and spacer supports, gas pipe adapter, snap fit joints, and high-voltage connectors.

Figure 3.11: Some of the 3D prints designed for special mechanical purposes. The insulating material allows custom designed connectors, and the high precision enables fine-tuning alignment or support components.

I also contributed to the construction tasks by designing support stands and casing boxes which satisfies special needs for muography. I designed a support stand for surface muography application which can accept type 80 or 120 chambers and 400–800 kg lead absorbing wall. Furthermore, it can be tilted by 10–20°. A photo and a schematic picture is shown in Fig. 5.2. Underground applications require a much more compact mechanical structure, and since the detectors and the support structures are custom designed, I intended to include as many features as possible. Besides that the boxing fulfills the requirements established in Sec. 2.3.3 (IP54 protection against water droplets, dust, etc.), they are dismantleable (have access to all sides), lightweight, impact and wear resistant due to the aluminum support and polycarbonate casing, and the angular direction can also be adjusted. Examples of different underground detector modules are described in the next section, with photos about these assemblies shown in Fig. 3.13.

3.1.2 Detector assembly variations and resolution

A REGARD muon tracking detector system uses eight layers of multi-wire chambers by default (may vary case by case). Although only a straight line must be fitted to the measured points which would not require eight points at the first glimpse, it is still advantageous to used as many as possible for multiple reasons. The fit is more accurate with more points, and the efficiency and muon flux calculation is much more reliable. Moreover, the detector is more robust against chamber malfunction. The high number of layers also helps to filter out low energy background particles. In case of surface muography, when lead scattering walls are applied between the detector layers [74], the tracks must be reconstructed before and after each lead wall, so the background suppression depends on the accuracy of the tracking. In case of underground muography, natural radioactivity (especially in, e.g., uranium mines) can create fake straight line tracks, but the probability of this can be reduced with more tracking points.

Our surface muography detectors, that contain MWPC chambers and lead scattering walls, are called MMOS (MWPC Muography Observation System [91]). Usually 80 or 120 cm versions are applied in vertical alignment with multiple 2–5 cm thick lead walls, spreading along a 2 m long telescope length (see an example in Fig. 3.12), where the telescope length is defined by the distance of the first and last tracking points of a perpendicular muon track.

For underground applications [30], the main design driving factor is portability (in addition to all the other requirements mentioned in the previous sections), and considering the relatively much lower background than on surface, lead scattering walls are not used. The chambers lie horizontally on top of each other, and the precise alignment and spacing of the layers is solved by 3D printed elements. The detector systems, containing 80 × 80 chambers, are called MTL-X (Muon Tomograph Large, with a serial number in the place of 'X') and the detectors that contain 50 × 50 chambers named MTS-5X (Muon Tomograph Small, with a serial number starting from 50). Three different mechanical designs have been constructed for the MTL detectors: MTL-1 has a two-axis rotatable and tiltable stand (72 cm telescope length), in MTL-2 the chambers have been grouped to two separate box and a spacer can be included to enlarge the telescope length (43+30 cm telescope length), and MTL-3 has the simplest construction with one box (42 cm telescope length) and a one-axis tiltable stand. Images of the MTL and MTS detectors are shown in Fig. 3.13.

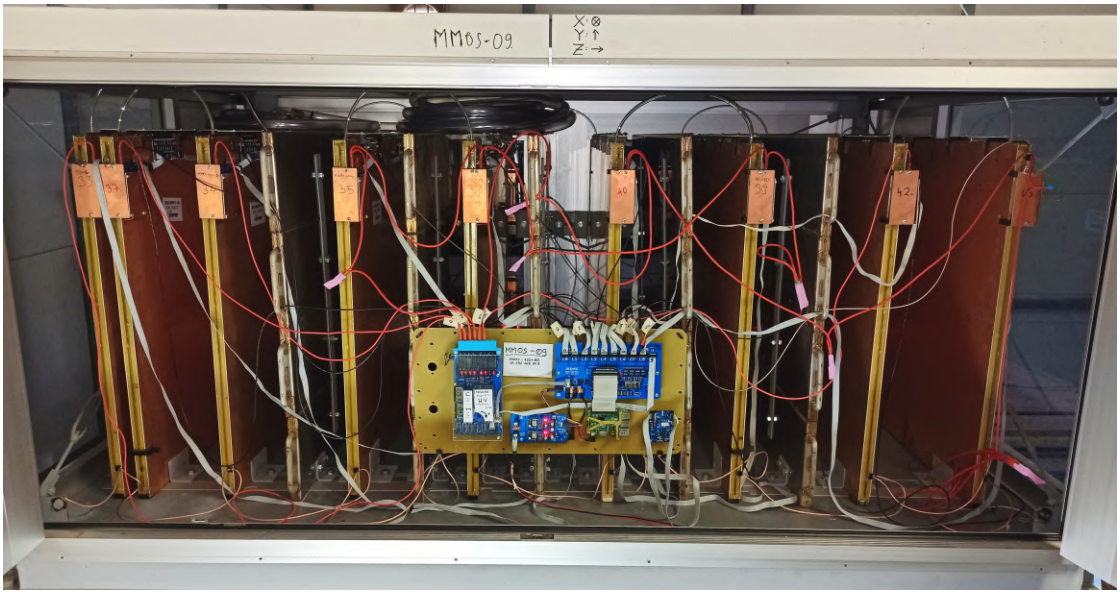

Figure 3.12: A MMOS module at the Sakurajima Muography Observatory [92]. The MWPC modules and absorber/scattering lead walls are arranged vertically, and the DAQ system is located at the center.

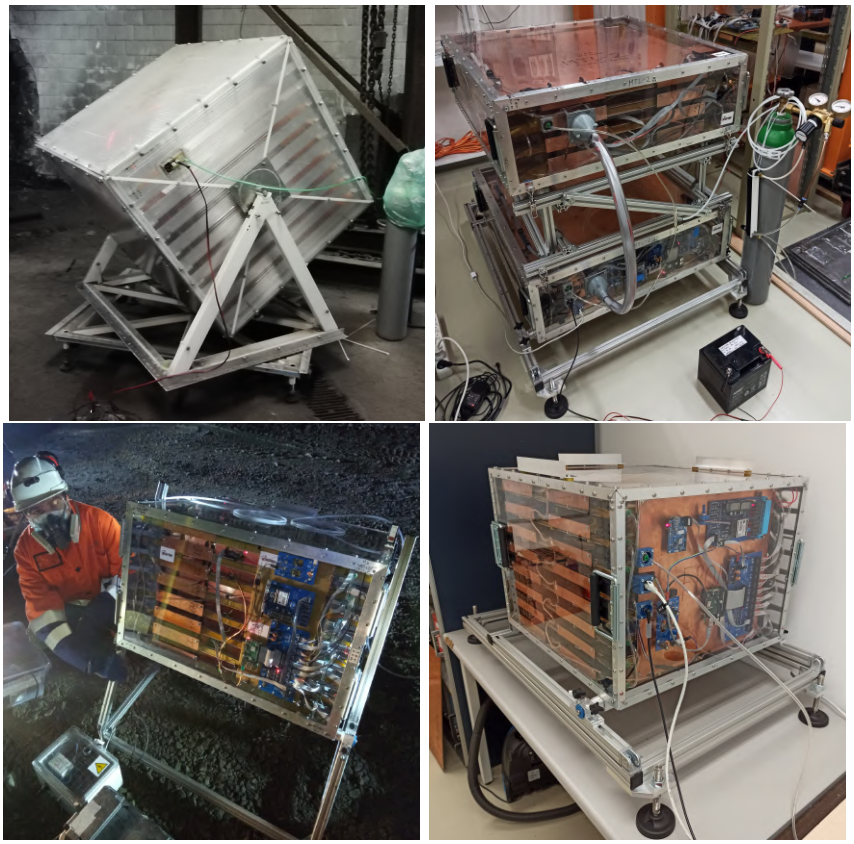

Figure 3.13: Photos of the underground MWPC modules: 'MTL-1' in top-left (muograph with type 80 chambers, on its inclinable rotatable support), 'MTL-2' in top-right (80 cm muograph with two detachable parts), 'MTL-3' in bottom-left (an 80 cm muograph deployed in the Kemi mine, Finland), and 'MTS-50' in bottom-right (compact type 50 muograph).

The MTL-4 and MTL-5 detectors follow the MTL-3 design. The MTS detectors also have a simple design like the MTL-3 (scaled down to their size), of which MTS-50 and MTS-51 have been already constructed and operating. Furthermore, additional detectors are under construction. Type 40 chambers do not have a dedicated support-casing system, but these chambers are very useful for laboratory calibration measurements. The total weight (with casing and stand) of an MTL is around 70–90 kg, and the MTS series are below 50 kg. Standard FC18 gas cylinders (e.g., 50 l, 10 l, 5 l, or 2 l, on 200 bar) can be attached. For instance, a 10 liter bottle could last for more than a year. The total power consumption of a detector is 5–6 W, thus a 12 V 100 Ah battery can last ∼240 hours. Solar panels, and custom designed low-noise UPS system can be integrated as well.

The angular resolution of a tracking detector could be defined as the full width at half maximum (FWHM) of the response function from a point source. In muography it is difficult to produce point source muons, but a simplistic solution is to define angular resolution by the ratio of the segmentation size (δp) and telescope length (l)

$$\delta\omega = \arctan\frac{\delta p}{l} \approx \frac{\delta p}{l}. \tag{3.1}$$

On one hand, the issue with this quantity that it is not including the possible detectorphysical flaws like segmentation inequalities, discretization errors, channel cross-talk, missing or noisy channels, etc. On the other hand, it is an overestimation since clusters usually contain multiple channels, and by the cluster center weighting, the resolution should be better than what Eq. 3.1 implies.

A fair question is how the above mentioned issues affect on the theoretical angular resolution. A simple method is presented here to measure directly the angular resolution. I extended the telescope length by adding an extra tracking layer 4 meters away from the bottom of the detector under investigation, which ultimately reduces the angular resolution by roughly an order of magnitude. Using the high-precision track measurement as point source like reference, I determined the FWHM of the Gaussian response function for multiple tilt angles of the detector. I calculated the quantities for the X-Z and Y-Z projection of the detector separately (the Z "view" axis always perpendicular to the layers). An explanatory sketch of the procedure is shown in Fig. 3.14. When a real track arrives vertically, the tracking algorithm does not necessary fit a perfectly vertical line to the clusters due to the limited resolution (dashed green line), although the extended fit (black line) is sufficiently precise. The FWHM resolution derives from the histogram of the angle deviations in a given tilt

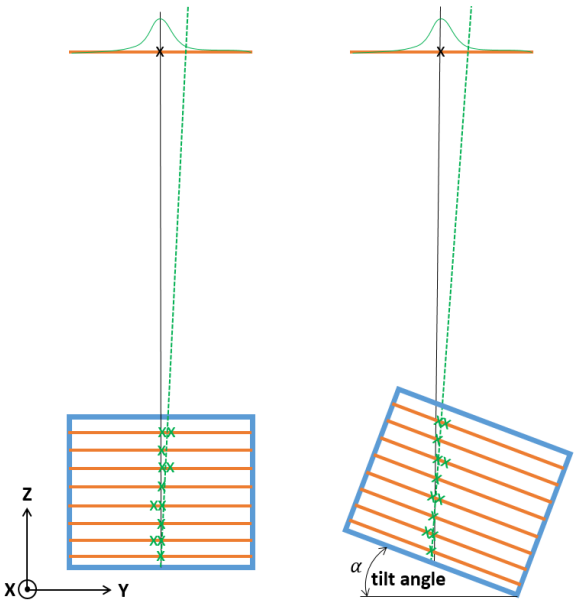

Figure 3.14: Sketch of the direct measurement of angular resolution for tracking detectors.

angle.

The results of the MTL-4 detector are shown in Fig. 3.15. In this case, the detector is tilted around the X axis, so the angular resolution is expected to decrease cos-like in the X-Z projection (X resolution), and $\cos^2$-like in the Y-Z projection (Y resolution), because by an α tilting, the telescope length is effectively longer by $l' = l/\cos\alpha$. In the Y-Z projection the apparent segmentation is also smaller by a factor of $\delta p' = \delta p \cdot \cos\alpha$. It is worth noting, that the resolution expected from Eq. 3.1 is 28 mrad (12 mm segmentation, 420 mm telescope length). However, the peak of the direct measurement of the raw resolution (Fig. 3.15 left) only 23 mrad. On the right, the tracks have been corrected channel-by-channel to avoid

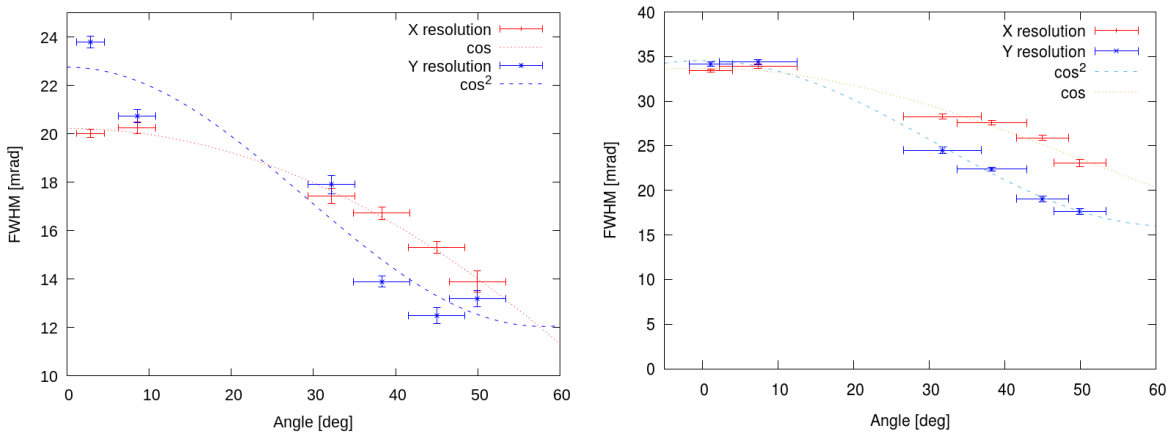

Figure 3.15: Results of the resolution measurements of the MTL-4 detector. The FWHM of the angle deviation is plotted as a function of detector tilting angle. On the right, tracking-based smoothed data are presented, on the left, the raw data are shown.

the possible interference-like patterns in the high resolution muon flux image, caused by the above mentioned detectorphysical flaws like segmentation inequalities or discretization errors. The details of this correction is beyond the scope of this work, but the effect can be directly measured by this method which ultimately smoothes the Gaussian curve. The effect of smoothing naturally lowers the resolution but only with less than a factor of two and the data fit perfectly to the expected tendencies.

For different variations of the detectors, the angular resolution changes linearly with the segmentation size, and changes inversely for the telescope length. For example, it has been confirmed that the MTL-2 detector with the extra 30 cm spacer (73 cm total telescope length) has a resolution of 10.6 mrad FWHM in the X-Z projection, and 12.2 mrad in the Y-Z projection (at zero tilting angle). Furthermore, for the MTS-50 it is 16.7 mrad and 20.0 mrad, respectively. Our surface detectors – which has at least 2 m telescope length – can reach 5 mrad resolution [74].

The determined angular resolution sets the smallest physically meaningful angle binning size, in which the muon flux, detector efficiencies, and other quantities are calculated later. The suitable resolution depends on the application, specifically on the expected size of the examined object and the distance of the detector, the ratio of which should be above the detector resolution. Other important factors to consider are the relatively low muon rate and possible multiple scattering of muons in the target material as mentioned before. Therefore,

it is not advisable to use angle bins that are too small and preceding calculations are required for optimization.

3.1.3 Low gas consumption for autonomous operation

For any gaseous detector, sufficient gas purity must be maintained, since the working gas can be contaminated by electronegative substance (e.g., oxygen, water) by either diffusion, leak, or outgassing from construction materials [93] which obstructs the formulation of Townsend avalanches in the detector. One way to maintain the purity is 'sealed mode' which means that the gas system is closed and the detector is well protected against any contamination. It is actually possible to construct large size cosmic detectors using sealed proportional counters [94], at the cost of relatively low position resolution. A small-size portable muograph telescope was proposed using gas-tight RPCs [95], whereas under laboratory conditions as much as half a year sealed operation was demonstrated [96]. An alternate method for preserving gas purity involves the continuous flushing of gas. This approach is beneficial because it facilitates the construction and reduces the weight of the detector structure, as some degree of gas flow is permitted. This is due to the ambient pressure variation: the system is open-ended, therefore the inner gas pressure follows the atmospheric pressure to avoid mechanical stress on the containment structure. A detailed study [97] denotes possible sources of contamination, as well as the importance of gas autonomy in field applications, and a solution for low gas consumption by using a recirculating gas system with turbines and contamination absorbers. It is important to highlight low gas consumption, since regular gas system maintenance (gas cylinder replacement) in remote field applications can be complicated and unsustainable. Therefore, the key question I addressed [98] is how to achieve as low input gas flow as possible in a realistic outdoor muography system in the most simple way (without expensive and power consuming recirculation system).

For all discussions below, we define 'outgassing' as gain reduction relative to the pure gas (high flow) case. In fact, outgassing is a very broad and complicated term, which includes electronegative molecules from construction materials, but also ambient oxygen from diffusion through detector walls, or water which changes the electron drift velocity. This outgassing also includes even tiny leaks if exist, and air propagation into the sensitive volume from the open end of the gas system. The contamination can be translated to effective air content, which would correspond to the same gain reduction what was examined in Fig. 3.5. The outgassing rate can be quantified from the time derivative of the gain reduction, assuming closed system with constant environmental conditions (sealed mode).

I investigated the following effects in the aspect of low gas flow operation:

- Intrinsic detector outgassing: A test system was assembled for chamber outgassing measurement (gain drop in sealed mode).

- Tubing radial diffusion: A sealed-mode outgassing measurement does not address the issue of contamination propagation through the gas connection tubes or other parts of the gas system, which has been examined separately.

- Axial diffusion from open end: at very low gas output flow one must take into account that contamination can propagate by diffusion from ambient air through the outlet of

the gas system in the gas medium. Therefore the diffusion coefficient of air in argon carbon-dioxide medium has been determined.

- Breathing effect due to ambient temperature (or pressure) variation: Since the temperature drop causes gas volume contraction inside the detector, air can flow into the sensitive volume if the gas flow is lower than the flow caused by the contraction.

The effects are most apparent for large detector volumes, which are difficult to reduce without performance loss (reducing volume at a given area means reducing detector chamber thickness, leading to construction issues mentioned previously). As an example, one single MMOS module has typically a sensitive volume of 100–160 l, and an input flow of 2 l/h was typically used before. Adding a buffer at the end of the gas line, which has a sufficiently large volume, and at the same time long enough to restrict axial diffusion, is a very practical solution. This possibility is investigated below and allows us to reduce input flow at least an order of magnitude which is a significant reduction.

Chamber outgassing in sealed-mode: Gas contamination, including diffusion through chamber walls and gas release from internal components, is a fundamental limiting factor for the operation of low-flow detectors. In our case, this is measured by the gain reduction, because of the short electron drift length it correlates with the tracking performance.

The test detector system dedicated for the low gas consumption experiments is shown in Fig. 3.16, with a photo and a schematic view about the setup. Eight pieces of type 120 chambers lie horizontally on top of each other and cosmic muon tracks provide the gas amplification signal for the standard REGARD DAQ. The gas flows serially – as in all of our detectors – and the gas line order is indicated by blue arrows.

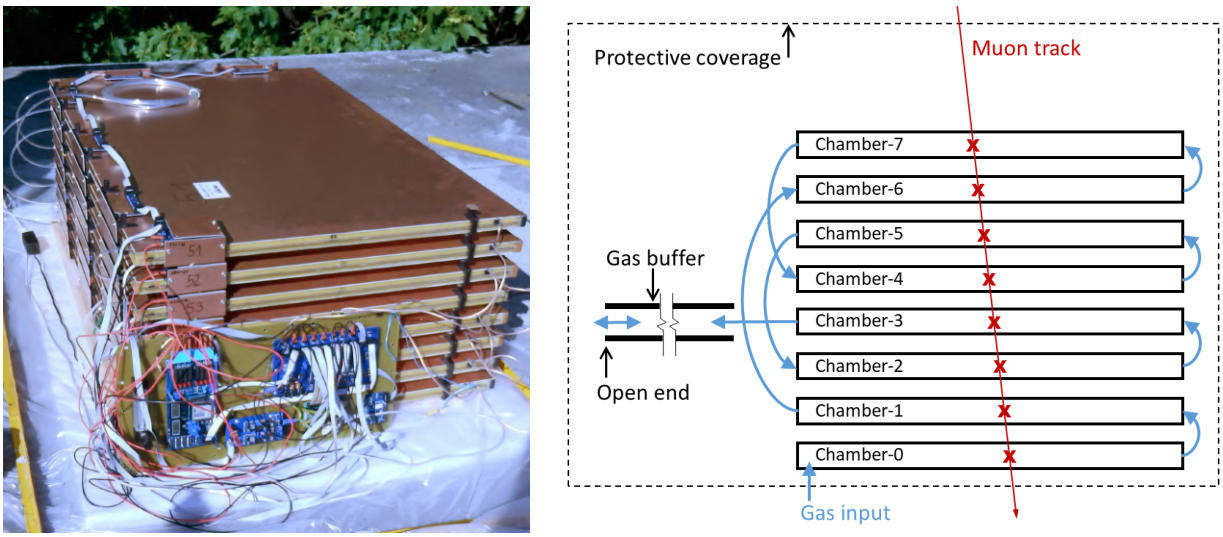

Figure 3.16: Left: The measurement setup installed outdoor, with protective coverage removed. The structure is the same as the one used for outgassing tests in the laboratory conditions. Right: Scheme showing the detector setup with eight MWPC chambers. The gas flows serially through the chambers according to the blue arrows, followed by a buffer tube with open end [98].

The first series of measurements were aimed at quantifying the outgassing of the chambers, which is defined as the rate of gain reduction in sealed mode. For this, eight 120-type chambers were installed under laboratory conditions. For a sufficiently long period of time, a constant gas flow was driven through all chambers. After reaching stable gain, the gas line was rearranged so that some of the detector chambers along the chain were isolated (sealed), and the remaining still received the constant flow. This way, the latters could be used as references, relative to which the gains of the plugged detector chambers were measured.

The results of the measurements are shown in Fig. 3.17. In the displayed results three chambers where measured for 14 days for outgassing, and similar results were obtained from other measurements for the rest. The conclusion of the measurement is that the outgassing of these units under laboratory conditions is below 0.3% gain drop per day. Since even a 30% gain reduction causes no efficiency loss, this means that the full volume can be exchanged in 100 days if we assume linearity. In this case (eight detector chambers with total volume of 160 l), it means that the lower limit of flow is 0.07 l/h (1 cc/min, or 1.6 l/day).

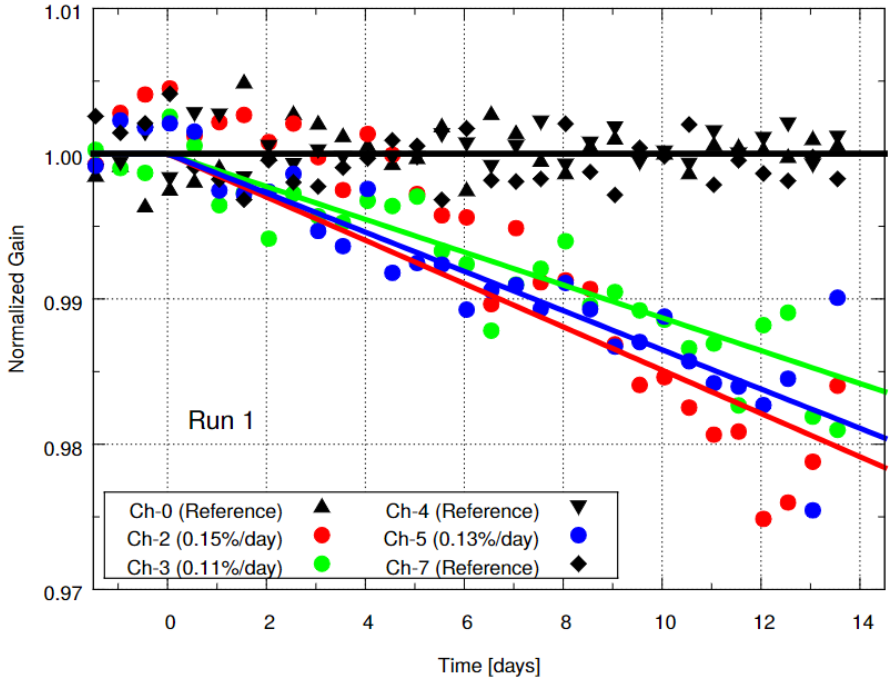

Figure 3.17: Measurements of detector outgassing (gain drop in sealed mode) under laboratory conditions. Chambers 2, 3, and 5 were measured for 14 days for outgassing in this run, the rest were reference with constant gas flow which were used for gain normalization [98].

This attractively low outgassing of the single chambers means that we do not actually need a high flow of clean gas to maintain sufficient tracking performance, the detector could work for even a few months without any new gas input. However, it is still beneficial to run some fresh gas because of the usually much longer muography survey campaigns. The questions are what the practical lower limit in real outdoor scenario is, and how to protect against the contamination effects. If we wish to use a buffer tube which feeds gas back to the system in case of contraction, candidates for such buffer tubing need to be characterized

for outgassing as well.

Tubing radial diffusion: Tubes in the gas system contribute to contamination due to the diffusion through their walls in radial direction. Potential gas tube material choices have been tested and selected for acceptable outgassing. I have found that some samples of PVC tubes strongly reduce gain. However, PU (polyurethane), PA (polyamide), and PE-RT (polyethylene raised temperature resistance) have acceptable outgassing levels for MWPC. Furthermore, copper and stainless steel perform excellent (no measureable outgassing) as perhaps expected for metallic connectors.

The following measurements were carried out in order to quantify gas tube outgassing. Using the standard setup with a serial gas line running at constant flow (with the smaller type 40 chambers in order to amplify the relative effects), the tube section under study was connected between two chambers. In this setting, the chambers before the test tube act as references, and the gain reduction can be measured using the detector chamber after the test tube. The flow and tube length were chosen such that the gas spends a characteristic time in the tubes similar to real conditions. To further minimize systematic errors, we removed the test tube after reaching the saturated constant gain and reinstalled the original (minimum length) gas connection. This action promptly restored the reference gain value. Examples are shown in Fig. 3.18, both for the stability of the reference, as well as the level of gain drop after the test tubes.

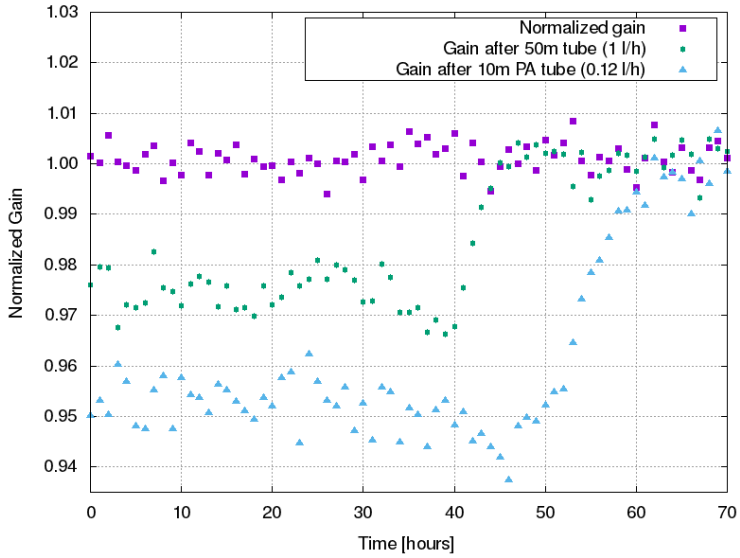

Figure 3.18: Tubing radial contamination diffusion measurement for a 50 meter long PE-RT tube with 16 mm inner diameter at 1 l/h flow, and a 10 m long 4 mm inner diameter PA tube at 0.12 l/h flow. The measurement started days before hour 0 to reach the stationary conditions. The reference chambers are indicated by purple color. At hour 40 and 50 respectively, the test tubes were removed and the gains clearly returned to the reference [98].

In conclusion, specific gas tube samples could be selected for sufficiently low outgassing, including a small (4 mm inner, 6 mm outer diameter) PA used for gas connections, and a large (16 mm inner, 21 mm outer diameter) PE-RT tube for buffer tube. The previously

showed measurements indicate that gas contamination is low in these tubes even if the gas dwells for a long time, but note that in practice the gas stays in them much less.

Axial diffusion: The process of air diffusion in one dimension along tubing from the open end is referred to as axial diffusion. The laws of diffusion (Fick's laws) provide a very clear analytic description and therefore there are very clear predictions about what to expect. A set of measurements were designed in order to test how quantitatively the system follows these predictions, first to ensure that in a complicated ambient condition one clearly understands the governing effects and second, to demonstrate that there are no additional effects beyond the pure diffusion.

The experimental setup contained six pieces of type 40 detector chambers to reduce measurement time and effects related to volume change, and the event rate was increased with a beta source. The underlying principle can be described as follows: variable length of test tubes were connected to the outlet of the final chamber in the gas chain. At the start of the measurement, the gas supply to this particular chamber was sealed off. As a result of diffusion, the gas within the exhaust tube gradually becomes mixed with air, eventually reaching the detector. After a certain time (depending on the length of the test tube), air also diffuses into the sensitive volume. This diffusion process results in a reduction in the gain. The test tubes had an inner diameter of 16 millimeters and was connected to the last chamber via a negligible volume of connecting tube with a fixed length of 14 centimeters and an inner diameter of 4 millimeters. Therefore, the gain of the last chamber – more specifically the derivative of the gain reduction – directly indicates the air concentration at the end of the test tube closer to the detector. These measurements were conducted under stable ambient conditions, with both temperature and pressure remaining constant.

In the case where the test tube length is zero (no test tube attached), continuous diffusion of ambient air from the external environment is present from the onset of the measurement, and therefore one expects a constant gain change (constant time derivative of the gain). This constant corresponds to the "pure air" concentration, serving as a reference relative to which a particular air concentration (at the end of the test tube near the detector) can be determined by the measured gain derivative. The results of these measurements are shown in Fig. 3.19 and confirm this expectation: gain change rate at the 0 m test tube length is indeed constant (normalized to 1 in the figure). The figure shows that 1 m, 2 m, and 4 m test tube lengths feature a considerably slower gain change. The rate of change approaches the ambient concentration after a long time.

In the general case, air concentration (c) along the tube is governed by the drift-diffusion equation

$$\frac{\partial c}{\partial t} = D \cdot \frac{\partial^2 c}{\partial x^2} - \frac{\partial (c \cdot v)}{\partial x} + D_R, \tag{3.2}$$

where D is the diffusion coefficient, v is the flow velocity in the tube, and D_R is the radial diffusion. The radial diffusion has been discussed previously, and found to be negligible. For this measurement setup, the gas movement along the tube (due to breathing effect) is zero now, so $v = 0$. After these considerations, the solution of the pure diffusion equation for air concentration (c) in an infinitely long tube is

$$c = 1 - \mathrm{erf}\left(\frac{L_{diff}}{2\sqrt{D \cdot t}}\right), \tag{3.3}$$

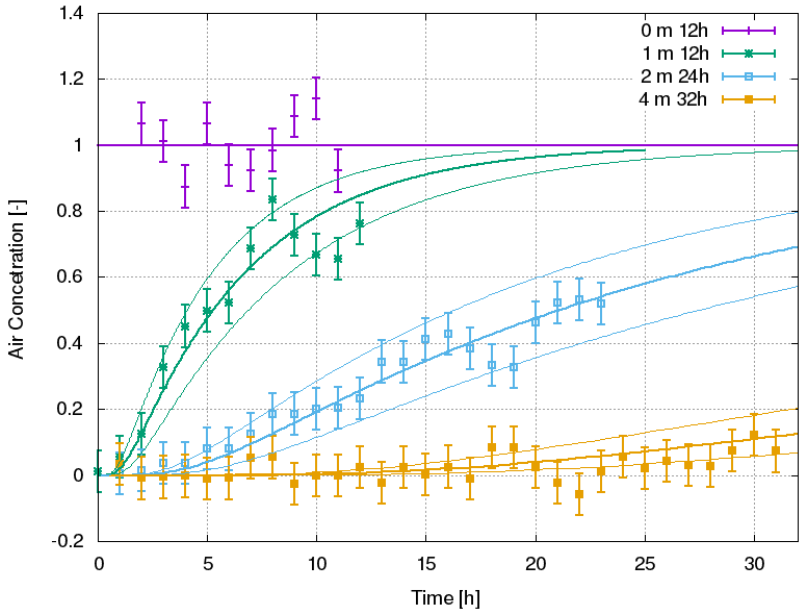

Figure 3.19: Air concentration at the detector end of the variable length exhaust tubes, obtained from the gain change rate (normalized time derivative) of the last chamber where the test tube connects. 0 m length corresponds to contact with pure air, therefore the gain change rate is constant. Solid lines show prediction with a $D \pm 30\%$ bracket [98].

where L_{diff} is the tube length from the open end. For our measurement, the boundary condition at the detector end of the test tube is such that the flux is nearly zero (the short connection tube is much thinner than the test tube). Using the relevant solution, shown with solid lines in Fig. 3.19, one gets a nice agreement with the measurement at the diffusion constant value $D = 20.1 \pm 0.7$ mm^2/s. Systematic errors up to 30% could not be ruled out (based on the upper estimation from the results). Therefore, dashed upper and lower envelope curves are also plotted. It is remarkable to observe the scaling behaviour: a 4 m long tube takes 16 times longer time to reach the same concentration by diffusion. There is no indication of deviation from the "diffusion-only" behaviour after 30 hours, due to outgassing, radial diffusion, or leaks. In practice, due to diffusion only, the air contamination in a tube – initially filled with pure gas – reaches approximately 1250 ppm after 24 hours, measured at a distance of 6 meters from the open end (or the same contamination level occurs after 6 hours at 3 m distance), according to Eq. 3.3.

Axial diffusion can be significantly reduced by choke elements in the exhaust tube. Fig. 3.20 illustrates a thermal conduction analog simulation of three different choke placement configuration in a 1 meter long exhaust tube. Each choke element has a constriction (1 cm long and 4 mm diameter passage). In the first case, the simulation does not include a choke element, resulting in an equivalent situation to the "1 m" diffusion case in Fig. 3.19. The "1 choke" case consists a choke element at the end of the tube, and the "2 chokes" case consist one in the end and one in the middle.

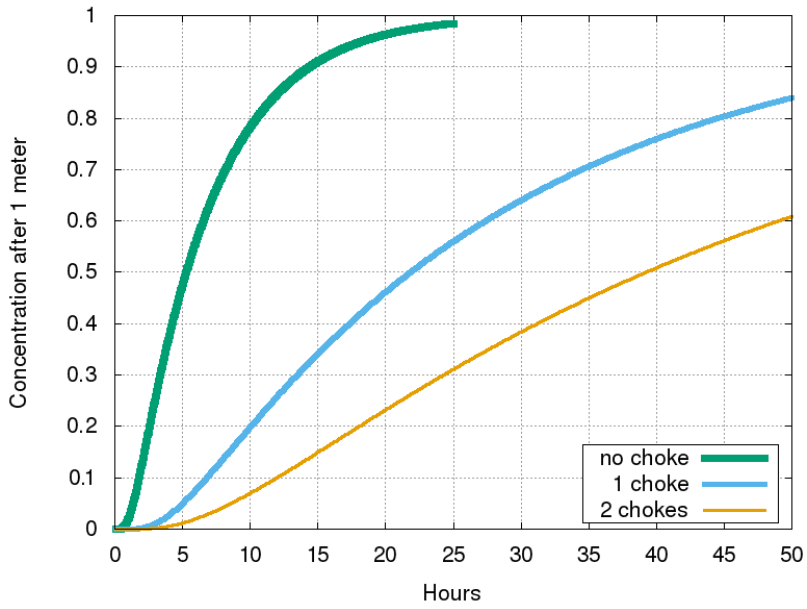

Figure 3.20: Simulations of air concentration if 4 mm diameter choke elements are applied in a 1 m exhaust tube. No-choke element is the same as the 1 m case in Fig. 3.19 [99].

Breathing effect from temperature cycling: Since the pressure and temperature inside the chambers follow the external conditions, the density of the working gas stored in the given detector volume also varies with the ambient parameters. Therefore, without any input flow, the volume of the gas inside the detector shrinks or expands due to the gas laws, resulting inlet or outlet flow at the open end which is referred to as "breathing effect" here. In field applications, the daily temperature fluctuations pose a significant challenge when the input flow is low. If the input does not supply an adequate amount of working gas, external air may be drawn in through the exhaust. I present here my measurements and quantification of this effect.

The measurement setup is shown in Fig. 3.16, which is installed on a flat rooftop outside the laboratory building in a sunny weather in order to affect the system with a high gradient of daily temperature changes. A light box, as well as reflective coverage, was used to protect it from rain and direct sunlight. The eight 120-type detector chambers, each with a 20-liter volume, were operated from a variable flow gas source, fed from the inside of the building. As presented in the schematic figure, the ordering of the chambers in the serial gas line was such that the gas entered at the bottom and then fed the top chambers, with the middle chambers at the end of the chain (exhaust after Chamber 3), this way compensating for possible temperature gradient effects inside the box.

When the temperature drops, it is predictable – or can be derived from the combined gas laws and the continuity equation – at which point the exhaust flow I_{out} (expressed in units of l/h) becomes negative at given input flow I_{in} and temperature change

$$I_{out} = I_{in} + V_0 \cdot \frac{\Delta T' - \Delta P'}{\Delta t}, \tag{3.4}$$

where $T' = (T - T_0)/T_0$ and $P' = (P - P_0)/P_0$ are the relative (Kelvin) temperature and

pressure values, against fixed T_0 and P_0 references, and V_0 is the total gas volume in the detector at reference state. However, the effect of pressure was insignificant, so it was neglected. Thus, the equation means that the exhaust flow turns negative if the volume change over time is greater than the input flow due to relative temperature change. In order to test this prediction, I have measured the gain of the last chamber in the chain without buffer tube (only a negligible volume connection tube attached to it).

Therefore, a sharp gain reduction is expected when the I_{out} turns negative and air rapidly enters into the last chamber. The results of one measurement are shown in Fig. 3.21, indicating the breaking point ("Backflow") where the gain change appears at a given (0.8 l/h) input flow. The breaking point and the corresponding temperature derivative is determined by interpolation. The top panel shows the absolute values (temperature and gain), whereas the lower panel is the numerical time derivative, which carries the quantitative information for Equation 3.4.

The measurement was repeated for multiple days with different input flows, attempting to observe the gain drop, and determine the corresponding critical temperature drop rate for the various gas input flow values. Fig. 3.22 shows the measurements with well identified breaking points as a function of input flow, which indeed follow the direct prediction, and confirm the quantitative parameters of the system.

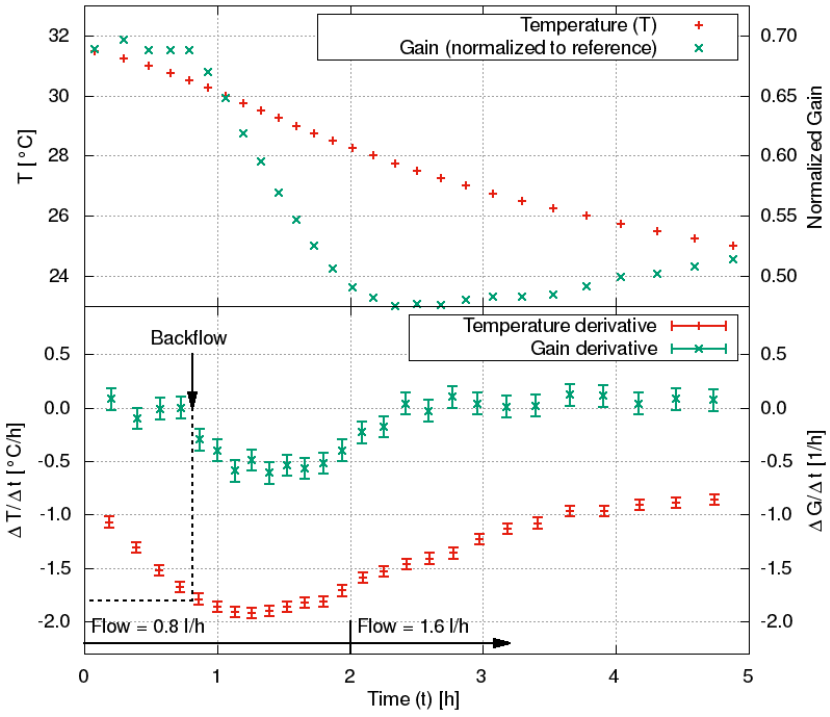

Figure 3.21: Measurement of gain change in the last chamber of the gas chain at 0.8 l/h flow during the period of gradual cooling of the system. The top panel indicates the temperature and gain (normalized) values, and the bottom panel shows the time derivatives of the backflow breaking point (marked by a black dashed vertical line) and the corresponding temperature derivative [98].

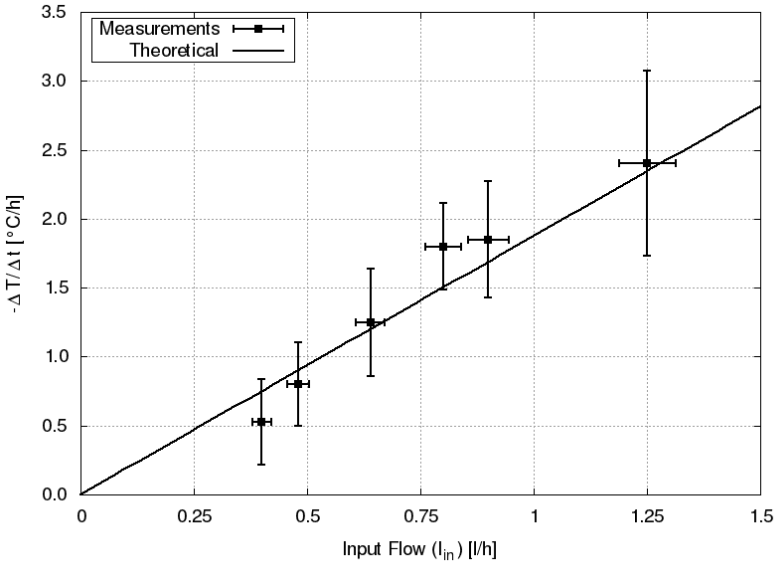

Figure 3.22: The critical temperature reduction rates at different flow values, where the gain drop was observed due to air backflow ($I_{out} < 0$) [98].

In conclusion, the buffer volume must be larger than the total gas volume contraction due to temperature drop, and the length must be greater than the total axial diffusion length during contraction time. The geometric parameters of the buffer can be calculated from the above mentioned equations, assuming that the volume of the detector and the expected highest temperature (and pressure) changes are known.

3.1.4 Stability

I performed several different measurements and analysis for the stability and calibration of the detectors for long term outdoor operation. First, a surface outdoor test of low flow (below 3 l/day) operation is demonstrated with a continuously running measurement that lasted for more than a month. The technical implementation of low flow is not trivial, but it can be achieved by high–precision flow meters, a needle valve with a calibrated static permeation, or timed gas injections with an electronic valve. The test system was the same as the one described in the previous section (Fig. 3.16 rooftop measurement with 160 l detector volume), and a sufficiently long buffer tube has been attached after the last chamber in the gas line, as shown in Fig. 3.23. The required buffer volume can be derived from Eq. 3.4 e.g., by taking an upper estimation with neglected input flow

$$V_{buffer} = V_0 \cdot (T'_{max} - T'_{min}) \,. \tag{3.5}$$

A 50 m long PE-RT tube with an inner diameter of 16 mm was chosen. That has nearly 10 liters of total volume. The maximum expected temperature drop is 15 °C which would correspond to an 8 l volume to be supplied from the buffer tube (40 m), with an extra length (+10 m) to compensate for daily axial diffusion. The purpose of the test was to demonstrate the practical applicability of low flow operation by testing all the contamination effects covered in the previous section at the same time.

Figure 3.23: The 50 m long 16 mm inner diameter PE-RT buffer tube attached to the end of the gas chain containing eight type 120 MWPC chambers [99].

The measurement was 50 days long, during which the system was running continuously. The working gas was supplied from the laboratory through a 10 m long PU connection tube. The overview of the measurement results and conditions is shown in Fig. 3.24. The flow was 2 l/h during the first 3 days, which was constant for a sufficient time before the beginning of the measurements. Then, for 4 days, the flow was set to 0.32 l/h. As the gain did not show signs of significant deterioration (no leak or major flaw), the flow was reduced to 0.12 l/h. For 36 days, the system was running at this input flow, when it was raised back to 2 l/h in order to confirm return to the original gain value. The "normalized gain" is the gain relative to the mean of the first 3 days. The figure shows the environmental conditions on the middle panel, with considerable daily temperature oscillation, as well as stormy periods with high humidity and pressure swings. The dark current of the high-voltage circuit is also monitored, since it has a correlation with the gain which is explained later (Fig. 3.26).

During the low-flow operation for more than a month, the gain was gradually decreasing and saturated at around 87% of the original gain, which is a minor reduction leading to no visible tracking or trigger efficiency loss (as concluded previously). It is also worth mentioning that the last chamber in the gas line, which received gas from the buffer every day due to breathing, was not significantly contaminated compared to the mean gain of all chambers.

The evolution of the corrected normalized gain chamber-by-chamber (Fig. 3.25) corresponds to the expectation from the lab measurements, with a gradual decreasing trend due to outgassing. At this flow value, the equilibration time is long: only 3 liters of gas are supplied each day, or in other words, it takes one week for the gas exchange of the entire volume of one chamber. If only pure intrinsic chamber outgassing would have happened then chambers later in the chain should have lower gains. Since it is apparent that all chamber gains had similar behaviour, this must have been due to contamination received before the detector system in the gas input line, probably due to the long PU connection tube. However, even this was tolerable for the detector system. The gas line integrity is demonstrated by

the sequential cleaning of the chambers after switching to the standard 2.0 l/h flow on 29th August. The measurements indicate that this detector system can be operated safely and without performance loss at a flow of 0.12 l/h (3 l/day) in ambient field conditions with the described gas buffering scheme.

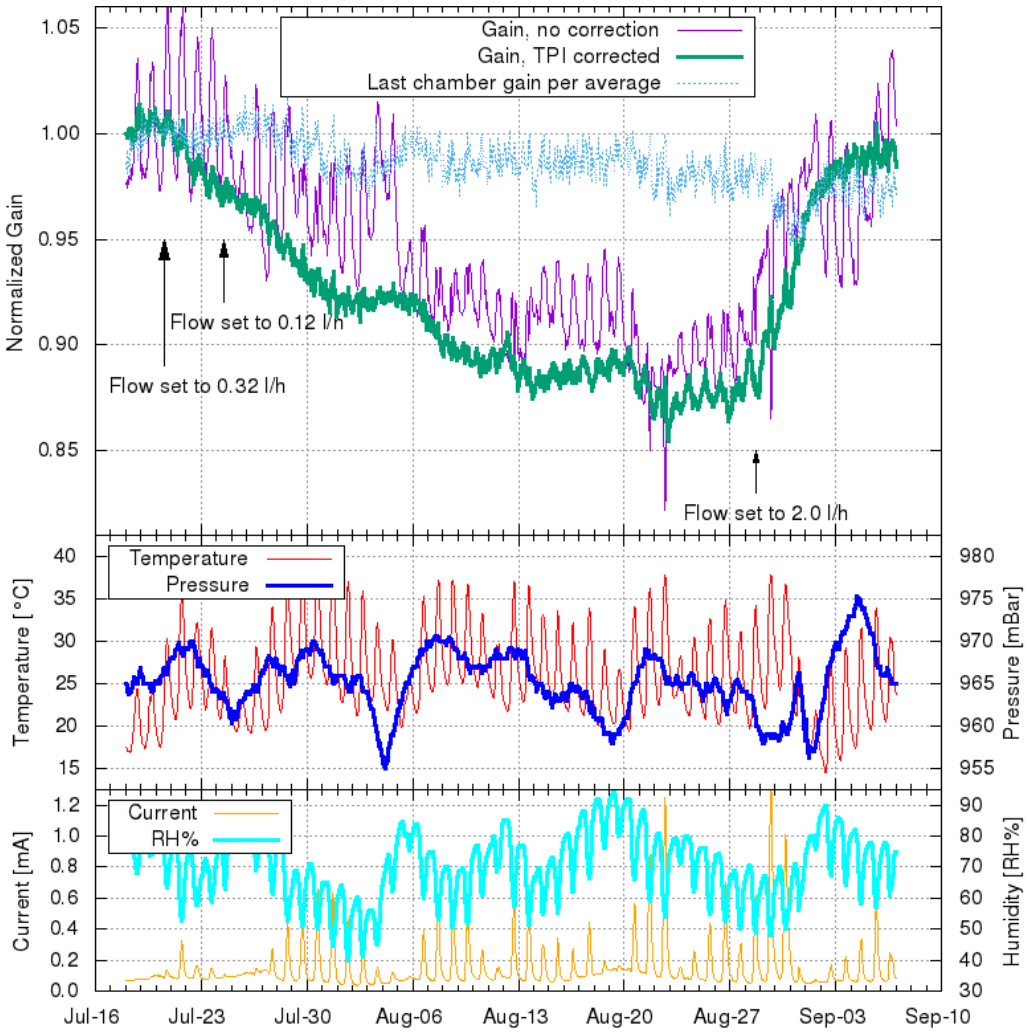

Figure 3.24: Top panel: normalized gains (relative to the gain during the first 3 days), over 50 days of measurement. Purple thin line represents the average gain of all chambers without any correction, and green thick line shows the TPI (temperature, pressure, current) correction. Blue dashed line represents only the last chamber gain (divided with the overall average gain), showing that the air did not reach the detector from the open end (there is no rapid gain drop). Middle and bottom panels: environmental parameters (temperature, pressure and relative humidity) and the anode current in mA. The flow settings are indicated by arrows, the flow was constant at 0.12 l/h during 36 days [98].

The daily gain oscillation due to the correlation with pressure and temperature is evident from the raw data (as the uncorrected gain data shows in Fig. 3.24, purple line). This is mainly caused by the gas density variation which has a direct impact on the Townsend

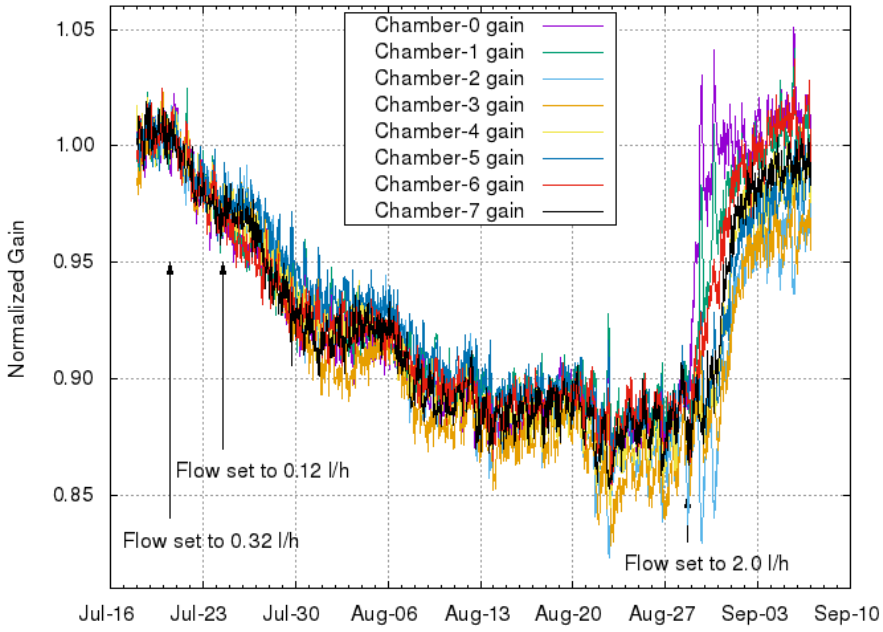

Figure 3.25: Normalized gains (relative to the mean of the first 5 days) for the individual chambers. High gas flow (2.0 l/h) was restarted on 29th Aug, after which gas cleaning proceeds in all chambers resulting in a sharp rise in gains [98].

avalanche formulation [93]. Correcting for this is important for reducing gain uncertainty and to validate, that the gain drop due to outgassing was indeed saturated. In order to calibrate for the dependencies on the environmental parameters, I provide a brief summary about the process of electron avalanche in wire chambers and a simplified model of the governing effects.

The gas gain ($G = N/N_0$) is defined as the ratio of the number of electrons after the development of the Townsend avalanche (N) to the number of primer electrons (N_0). The exponential growth of the avalanche over a unit length of path (ds) can be described as

$$dN = N\alpha ds, \tag{3.6}$$

where $\alpha(E, \rho)$ is the Townsend empirical coefficient which depends on the electric field E and the gas density ρ (for a given gas composition). So, basically the gain depends on α, and the path length of the avalanche. The starting point of the electron multiplication process depends on the minimal electric field ($E_{\min}$) derived from the energy needed to accelerate the primer electron so it can ionize further gas molecules, divided by the mean free path between collisions (therefore $E_{\min}(\rho)$ is proportional to the gas density). The electric field near an anode wire is given by the charge per unit length (λ), as a function of the radius (r)

$$E(r) = \frac{\lambda}{2\pi\epsilon_0 r}, \tag{3.7}$$

where ϵ_0 is the vacuum permittivity. By integrating Eq. 3.6 from the starting point of the avalanche ($s_{\min}$) to the anode radius (a), and inserting Eq. 3.7 one gets

$$G = \frac{N}{N_0} = \exp \int_{s_{\min}}^{a} \alpha(s)ds = \exp \int_{E_{\min}}^{E(a)} \frac{\alpha(E)}{dE/ds} dE = \exp \int_{E_{\min}}^{E(a)} \frac{\lambda\alpha(E)}{2\pi\epsilon_0 E^2} dE. \tag{3.8}$$

From here, multiple different methods are outlined in the literature. I summarize briefly the formula from Diethorn [100], which assumes α to be proportional to E (a reasonable assumption typically in the case of MWPCs with heavy noble gases such as argon). The proportionality is related to the average energy required to produce one more electron (ΔV). The number of generations (Z) of doubling the electrons in the avalanche ($G = 2^Z$) relates to the potential difference between a and $s_{\min}$. Thus,

$$Z = \frac{\Phi(a) - \Phi(s_{\min})}{\Delta V}, \tag{3.9}$$

which corresponds to Eq. 3.8. Therefore, putting together what we have, the the gain dependence can be derived as

$$\ln G = \frac{\ln 2}{\Delta V} \frac{\lambda}{2\pi\epsilon_0} \ln \frac{\lambda}{2\pi\epsilon_0 a E_{\min}}. \tag{3.10}$$

As we stated earlier that the $E_{\min}(\rho) = E_{\min}(\rho_0)\frac{\rho}{\rho_0}$ is proportional to the density, the variance of the gain can be expressed as

$$\frac{dG}{G} = -\frac{\lambda \ln 2}{\Delta V 2\pi\epsilon_0} \frac{d\rho}{\rho}. \tag{3.11}$$

In practice, the variation of gas density typically results in a factor of 4 to 8 variation in the gain. In our case, we identified three parameters affecting the gain which can be measured separately: relative temperature (T'), relative pressure (P'), and dark current (I). Consequently, the measurable linearized correction factors can be written as

$$\ln G = \ln G_0 + c_T \cdot T' + c_P \cdot P' + c_I \cdot I. \tag{3.12}$$

Note, that the value of pressure correction factor is negative (since it is linearly proportional to the density), and the temperature correction is positive but not equal in absolute value with the pressure correction due to the temperature dependence of the amplification of front-end electronics. Furthermore, the current correction also negatively correlates with the gain, because the dark current reduces the effective anode voltage and thus the electric field strength.

I determined the correction factors, shown in Fig. 3.26, by taking reference data from the measurements where all the parameters are constant besides the examined parameter. The left panel shows that the normalized measured gain change depends linearly on the the relative pressure change, where $P' = (P - 966)/966$ (here P is measured in mbar). The middle panel shows the correlation with the relative temperature change, where $T' = (T - 293)/293$ (here T is measured in Kelvin). The correction factors can be translated as 0.7% gain change per °C, and 4.4% gain change per 10 mbar pressure variation. We have identified an additional variable which affects the measured gain: this is the current (I) drawn on the high voltage (anode) as it decreases the operating voltage due to the high output resistance of the used HV unit. This dark current originates from temperature-dependent resistance of the construction materials of these chambers, and is significant above 35 °C (though not leading to efficiency loss). The gain correlates linearly with the current, as shown in the right panel of Fig. 3.26, which matches with the output impedance of our high-voltage power supply. Since all these

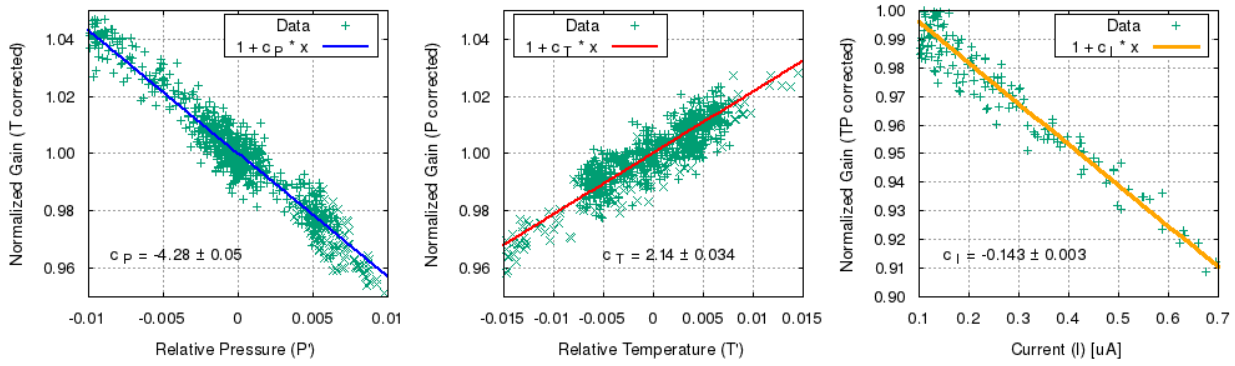

Figure 3.26: Measured correlations between the relative pressure (P'), relative temperature (T') and current (I) and the measured gain. The straight line fits (blue, red, yellow, respectively) are used for the correction [98].

correlations (T, P, I) could be quantified, the measured gain has been corrected for, as shown on the top panel of Fig. 3.24.

In addition, we performed some further important stability checks including temperature resistance, and static and dynamic mechanical stress tests. Required tolerances of mechanical stability are a key question for practical outdoor measurements to ensure resilience against transportation, or accidental hits in harsh environments, and to avoid cracks, leaks, inhomogeneity, or efficiency loss, or any malfunction that may jeopardise the whole measurement. Therefore, we traced the performance of the detectors during extreme conditions. The gain map (the mean signal amplitude over the sensitive surface) of a type 80 MWPC is measured with cosmic data and shown in Fig 3.27. In the first case (left), a normal condition are observed without stress. The second case (middle) shows a 1.5 mbar overpressure in the chamber. A slight bulging is expected which is held against by the support pillars. Overpressure could occur in practice during very high flushing flow (above 10 l/h) e.g., at the beginning of a measurement to quickly clean the detector gas volume, or if the gas line is unintentionally choked somewhere. The third study (right) involves placing two 1 kg weights on the surface of the detector. The results show robustness against these stress tests which is mainly due to the support pillars.

The strength of the epoxy resin has also been tested where potentially weakest material joints are used in the MWPC construction [69]. The measurement of the tensile strength between the G10 and copper plated FR4 glass reinforced epoxy has been conducted. These materials are bonded together using the Uverapid-5 two-component epoxy resin, contributing to the overall structural integrity of the detector. Furthermore, the joint between the ABS-based polymer pillars and copper plated FR4 has also been tested. The results are shown in Fig. 3.28 left, both cases repeated three times so that the measurements strictly and reproducibly support the result. The adhesive area between the pillar and FR4 plate were 22.4 mm^2, and 200 mm^2 between the G10 element and the FR4 plate, which indicates the pressures of 5.7 MPa and 1.5 MPa, respectively. It is worth drawing attention to the fact that the tensile strength is much higher for the 3D printed pillars due to the special design of the adhesive surface which also realizes a shape-locking connection. After careful modal analysis

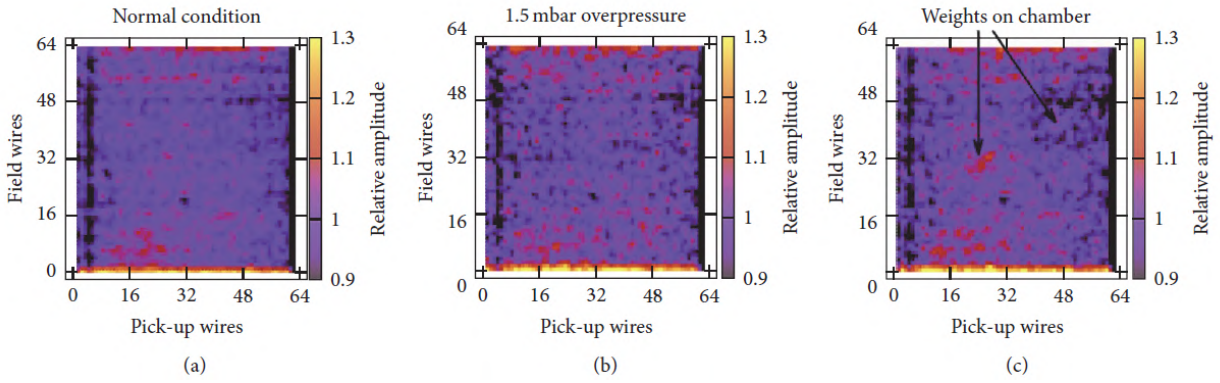

Figure 3.27: Gain map of an MWPC detector layer in horizontal configuration, under various test conditions. (a) is the reference and (b) shows the map for 1.5 mbar overpressure, (c) with two test weights (1 kg each) placed directly on the top of the detector [87].

measurements and finite element simulations, the stress caused by random vibrations of transportation has been examined, applying the ASTM D 4728 standard [101]. The results showed that the pillar-FR4 and G10-FR4 glue joints have a safety factors of 3 and 10, respectively, on the highest level of assurance. Therefore, the chambers can be transported without a problem. This played a role to develop the world's largest muographic volcano monitoring system operating in Japan but produced in Hungary.

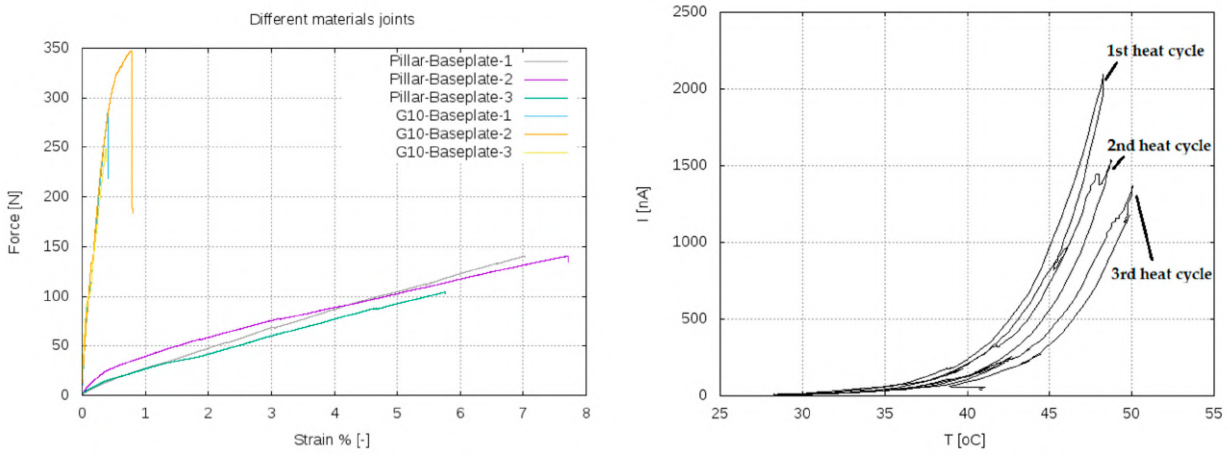

Figure 3.28: Left: The tensile test of the different material joints. Right: The "tempering" effect. After every heat cycle the total current is getting lower at higher temperatures. This can be used to prepare the chambers for field applications where temperature fluctuations are high [69].

The upper boundary of temperature resistance of the MWPC chambers has also been tested by a dedicated "heat box" setup: chambers have been operated inside an insulated box with heating circulation where temperature can reach up to 60°C. As mentioned before,

dark current can appear in high temperatures, depending exponentially on the temperature (Fig. 3.28 right). This current have no effect on the detector performance until reaching 1000 nA, and it only becomes significant above 2000 nA, but for the safe long-term operation, it is recommended to keep it below 1000 nA. As shown in the figure, this level corresponds to at least 45°C temperature.

To check the stability, we exposed the chambers to heat treatment multiple times, and we actually observed a significant decrease of the dark current after each heat cycle. This must be due to the applied epoxy resin which acts as an insulator between the ground and the high-voltage elements of the detector circuit, which can allow leakage current at high temperatures similarly as semiconductors. However, the high temperature can also cause a "tempering" effect, since at the chamber construction the polymerization of the epoxy glue is usually not perfect, but the high temperature can catalyze this process improving the polymerization and resulting in a higher resistivity against leakage current. This is evident in Fig. 3.28 right, after three heat cycles this chamber could be tempered so it can be safely operated even up to 50°C.

3.1.5 Applications

The first application of the advanced MWPC detectors was at the Sakurajima volcano, Kyushu, Japan, in collaboration between Wigner Research Centre for Physics, the University of Tokyo, and the NEC corporation starting from 2016 (patented as MMOS: MWPC Muography Observation System [91]).

The structure of one MMOS surface muograph detector module was shown previously in Fig. 3.12, and a photo of multiple modules is shown in Fig. 3.29 right. The structure of the MMOS modules, background suppression, and the first results obtained from the Sakurajima Muography Observatory (SMO) are described in [74].

The joint Hungarian-Japanese SMO facility has been developing ever since, and the number of MWPC modules reached 11 in the SMO so far (8.7 m^2 sensitive area) [102, 68, 89, 92] resulting in the largest muograph monitoring system in the world. The applied flux calculations and the effect of multiple scattering are shown in [37].

Extensive geoscientific research have been carried out until now, by the muographic imaging of the Sakurajima volcano (Fig. 3.29 left), including the observation of a plug formation beneath active craters [11], hydrogeomorphic changes induced by post-eruptive lahars and erosion [103], machine learning with muographic images for eruption forecasting examination [104, 105], and volcanic conduit imaging to explain the relation between eruption frequency and ground deformation [106].

Further applications of the advanced MWPC detectors are described in the Outlook section (see also, for example, [30]).

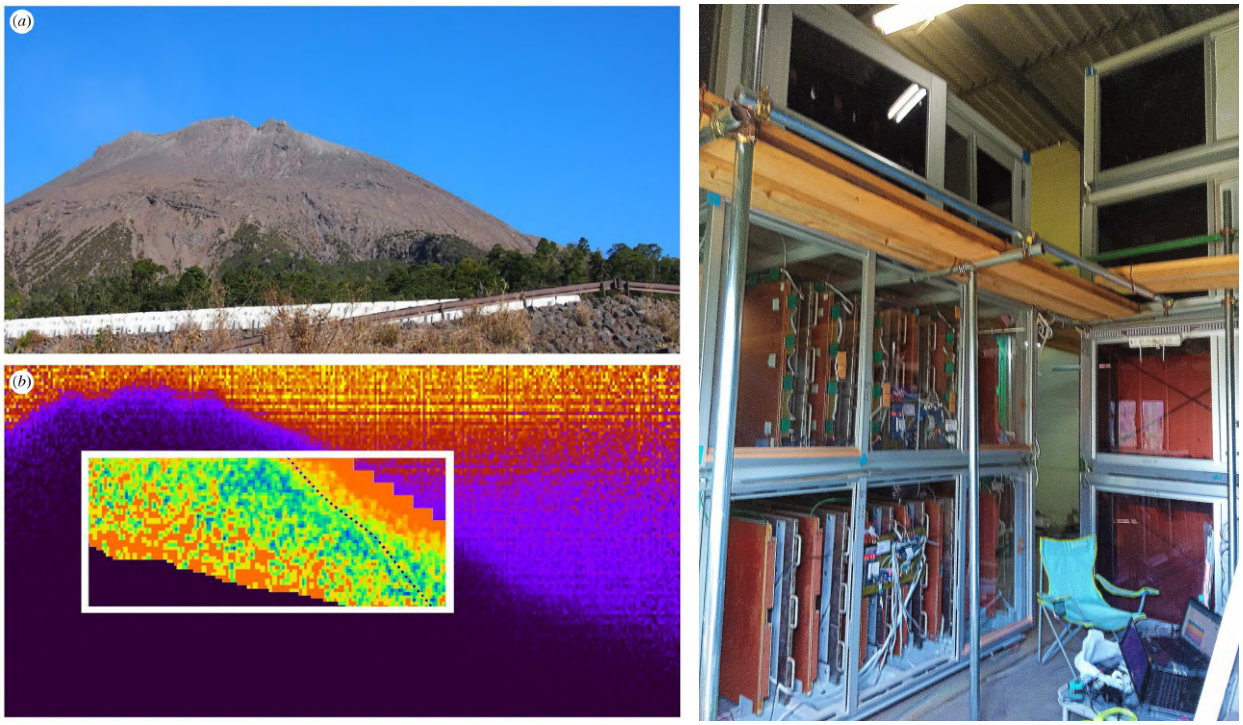

Figure 3.29: High-definition muographic observation of the Sakurajima volcano, Japan. The photograph of the mountain (a) and muon projection image (b) are shown, and the density distribution is superimposed in the latter as an inlet [10], (c) a photo of the MWPC based detector modules.

3.2 Micro-Pattern Gaseous Detectors

The Micro-Pattern Gaseous Detector (MPGD) is currently one of the cutting-edge technologies for large-size tracking, triggering, or even Cherenkov detectors [107] by taking advantage of the rapid development of PCB, photolithography, and microelectronics industries in the 90s. Most important advantages over the MWPC technology are high resolution and high rate capability. The MWPC technology has reached its physical limit since wires cannot be positioned closer without sparking, and the high particle rates demanded by high-energy physics could not be handled due to a relatively large space charge from avalanches resulting in relatively long dead times. One innovation, developed in CERN (European Organization for Nuclear Research) and later in the RD51 collaboration[2], is to apply high electric field not by wires, but micro-structured gas-amplification devices. In general, MPGDs have a rate capability above 100 kHz/cm^2 due to the reduced ion backflow, and a spatial resolution even below 100 µm thanks to the micro-structures that act as a preamplification stage, thus anode segmentation can be placed in close geometry with lower voltages without the risk of sparks.

Many different micro-pattern structures have been developed over the decades to optimize the technology, but I only describe two wide-spread branches that affect my work presented

[2] https://rd51-public.web.cern.ch/ (Accessed: 2023-05-30)

here: the Gas Electron Multiplier (GEM) [108], and the Micromegas [109], shown in Fig. 3.30. On the left, there is a microsopic image of a GEM layer and a schematic cross section showing the process of avalanche formation and electric field structure. The GEM is a perforated kapton or PCB with two metallic side on different high voltage potential. Due to the high electric field strength inside the holes, the electrons are multiplied as they approach the readout, which can be a conventional multi-wire or cathode strip structure. Multiple GEM layers can be employed to reduce even further the ion backflow.

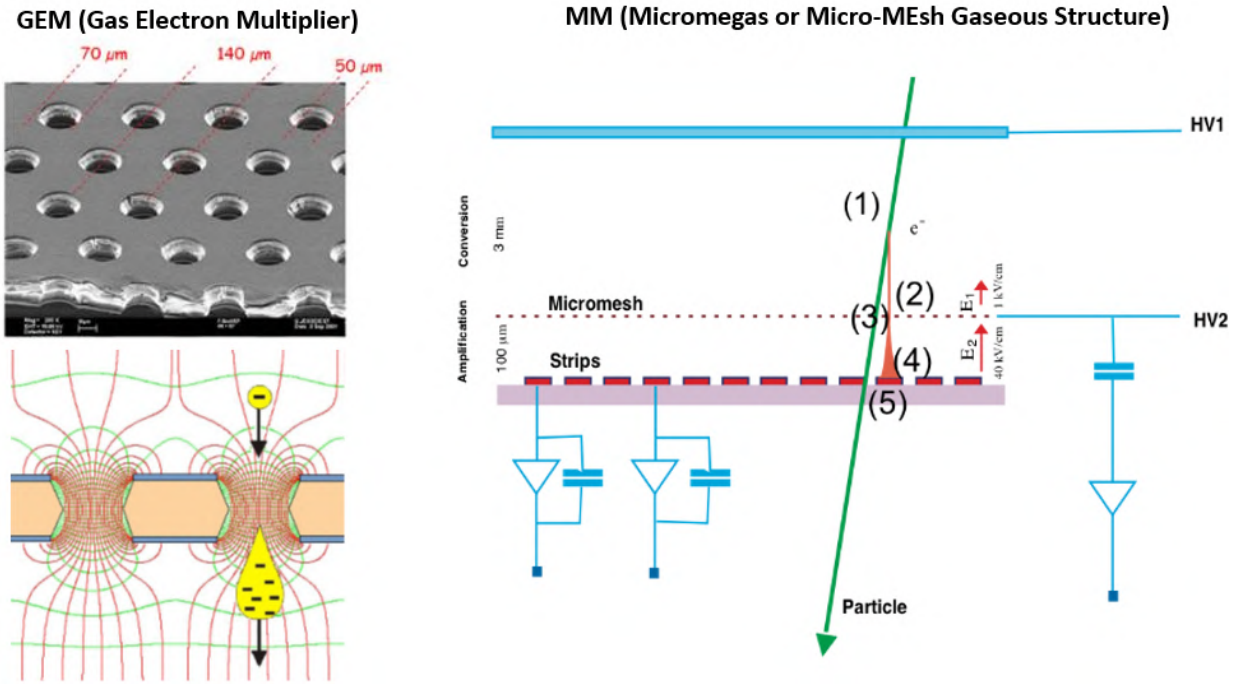

Figure 3.30: The two main technological branches of MPGDs: the GEM on the left is a perforated thin amplification layer, where the potential difference between the two sides of the GEM drives the avalanche through the holes. On the right, in the Micromegas a metallic mesh separates the amplification stage from the conversion region, which allow very high electric fields and thus gains.

Fig. 3.30 right shows a scheme of the Micromegas detector. A metallic wire mesh (Micromesh) separates the conversion drift region from the amplification stage. In the drift region, the ionization electrons drift with a constant speed towards the mesh due to a relatively low homogeneous electric field, and after the mesh they are multiplied in a high electric field. Finally, the signal appears on the corresponding anode strip after a 10^5 gain in the amplification region. It is also necessary to mention here, that not only 2D track detecting chambers providing the two coordinates by perpendicular readout channels, but also the so-called Time Projection Chambers (TPC) [107]. The principle of operation of the TPC is that by utilizing the constant speed of electrons in the drift region, the third coordinate can be calculated by measuring the time difference between the readout channels and an independent fast trigger signal. This way the 3D particle track can be projected back into

Table 3.2: A list of some applications of MPGD technology in high-energy particle physics.

Experiment	Physics	MPGD application
ALICE[3]	Physics of strongly interacting matter at extreme energy densities (e.g., quark–gluon plasma)	About 90 m^3 volume with TPC in the forward region
CMS[4]	Exploring TeV energy scales (e.g. Higgs boson, searching evidences for Beyond Standard Models	1000 m^2 planned surface with triple GEM in the forward region
ATLAS[5]	Confirmations or improved measurements of the Standard Model (Higgs boson), and beyond	1200 m^2 planned tracking system with Micromegas in the forward region.
COMPASS[6]	Investigation of the nucleon spin structure and hadron spectroscopy.	Detecting particles scattered at small angles with both Micromegas and GEM.
PHENIX[7]	Heavy ion physics, electron tagging.	Hadron Blind Detector (HBD) with GEM.
TOTEM[8]	Measurement of total cross section, elastic scattering, and diffractive processes.	Extended tracker system formed by circular GEM trackers.
T2K[9]	Neutrino experiments (e.g.: discovery of the neutrion oscillation)	The readout of the near TPC detector is based on Micromegas

the drift space. The drift length can reach even meters, and the readout can be realized with MWPC or any MPGD technology, providing an excellent but low material budget tracking method with economic channel numbers and particle identification capabilities.

Without claiming to be complete, I listed some applications of MPGD detectors in high-energy physics in Tab. 3.2. The extended use and future plans with MPGDs in basic research show a high potential of applications with this technology. Indeed, I demonstrate some ongoing and planned spin-off uses outside the high-energy physics research in the next section, focusing more on the muography implementations.

[3] https://alice-collaboration.web.cern.ch/
[4] https://cms.cern/
[5] https://atlas.cern/
[6] https://wwwcompass.cern.ch/
[7] https://www.phenix.bnl.gov/
[8] http://totem-experiment.web.cern.ch/
[9] https://t2k-experiment.org/

3.2.1 Review of MPGD detector applications for muography

MPGD-type muon detectors are well suited for muography applications, if high resolution or volume detectors are required [110]. A recent collaboration, ScanPyramids, has successfully measured several unexplored cavities in the Khufu pyramid, Egypt, where Micromegas-based detectors were also used (CEA, France) in combination with emulsion (Nagoya University, Japan, and Cairo University, Egypt) and scintillator detectors (KEK, Japan) [24]. In the imaging surveys of the Khufu pyramid all detectors encountered rough environmental conditions for long periods of time from outside the pyramids (surface muography), and provided useful data for the discovery [111]. The applied detectors are shown in Fig. 3.31. The CEA

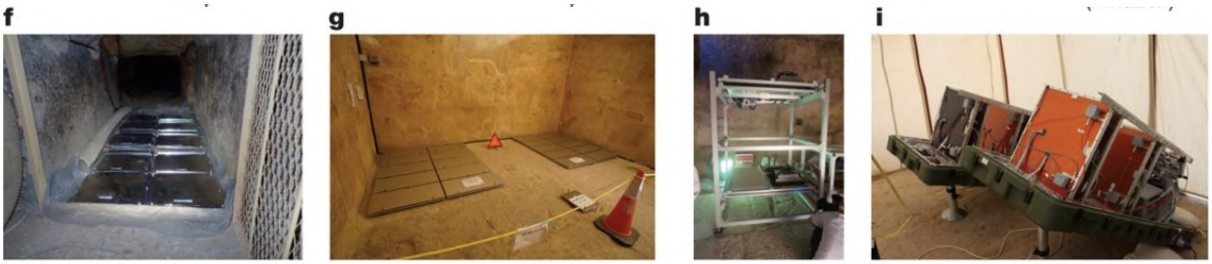

Figure 3.31: The applied detectors at the Khufu pyramid in the ScanPyramids collaboration. **f** and **g** show emulsion detectors in two different positions inside the pyramid, **h** shows the scintillator detector of KEK, and in **i** the Micromegas detectors provided by CEA are shown [24].

team is also working on a Micromegas-based TPC detector for borehole applications [112], with the main advantages of a bigger acceptance with a single telescope, and a compact size which can fit in medium-size (15 cm in diameter) boreholes for mining and civil engineering purposes (Fig. 3.32).

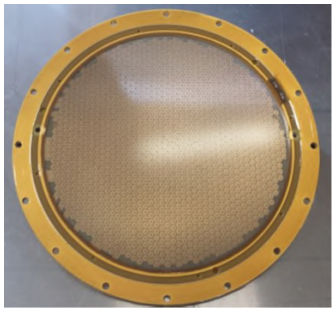

Figure 3.32: The Micromegas base of a borehole TPC from the CEA team [112].

In the Low Background Noise Underground Research Laboratory (LSBB) of Rustrel, France, the monitoring of the water level behind a dam has been demonstrated with Micromegas-based TPC detectors. The objective of the T2DM2 project (Temporal Tomography of Density by Muon Measurement) is to characterize the dynamics of water transfer processes in the critical zone, and in particular that of the Fontaine-de-Vaucluse (world's fifth largest karst aquifer) [113]. The advantages of the application of MPGD technology is the high position resolution in confined environment (underground) with a large acceptance and compact detector size (small telescope length). In Fig. 3.33, the muon flux measurement is shown in correlation with the linear regression of the water level as the dam is emptied (daily oscillations are due to temperature variation).

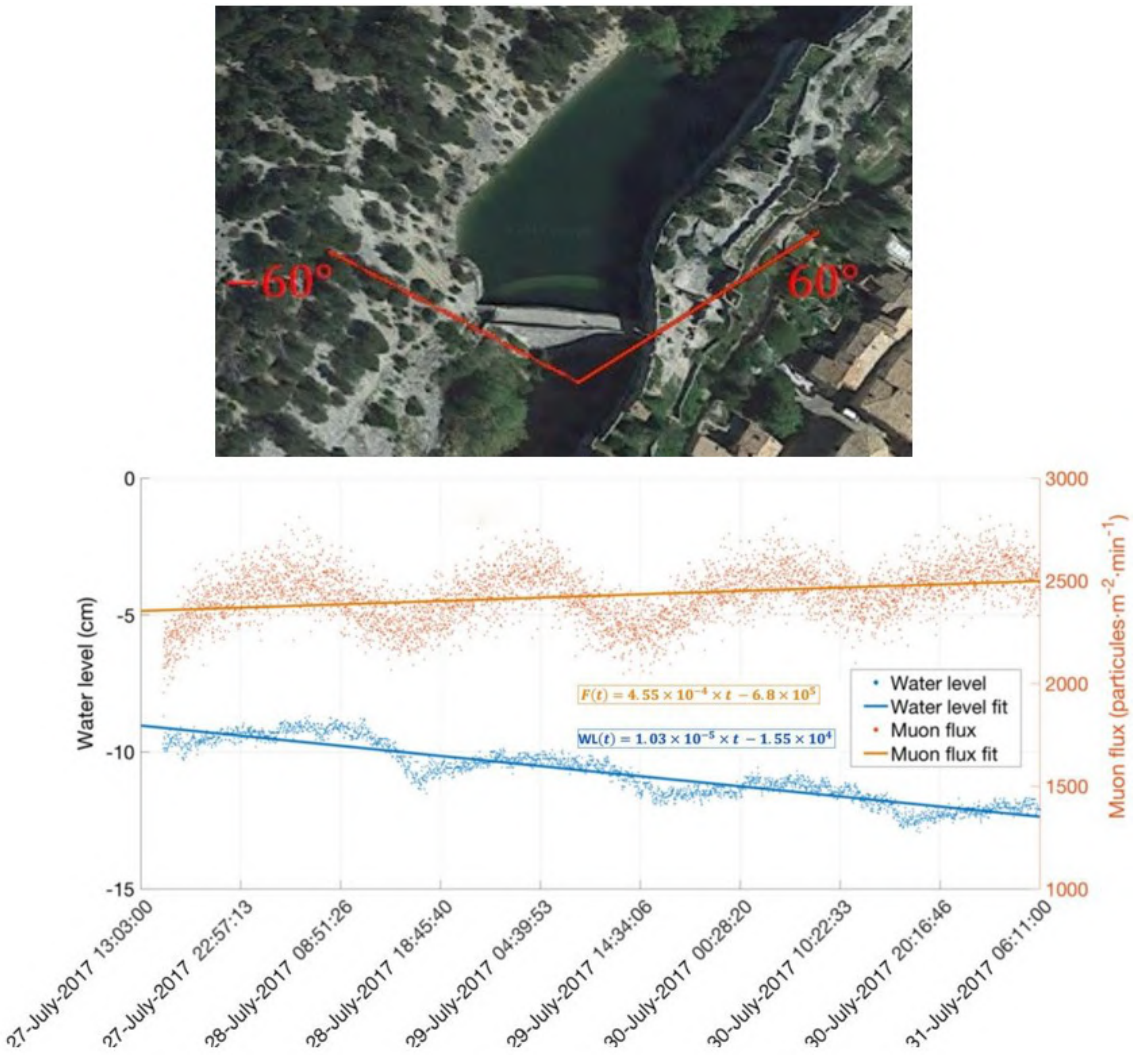

Figure 3.33: Temporal evolution of water level (blue) of the dam and the recorded muon flux (orange) [113].

Besides absorption muography, scattering muography is also a promising area for MPGD applications. MPGDs has generally high resolution which is needed for efficient scattering measurement. The high angular resolution is needed for the precise energy discrimination of the intermediate-energy muons by measuring the scattering angle in different materials. A team at the Florida Institute of Technology has applied GEM detectors to test the imaging capability of high atomic number materials (Fe, Pb, Ta) by this non-destructive imaging method [114]. The small size prototype (30 cm × 30 cm detector surface) is shown in Fig. 3.34.

Based on the technological advancement and above examples, I would recommend the application of MPGD detectors in muography when high resolution and/or monitoring is required, especially in compact sizes (e.g., in borehole muography). Scattering muography with MPGD in smaller sizes (cargo imaging up to a cubic meter) is also a very underutilized application gap, which chould be considered due to the provided high resolution for scattering angle measurements.

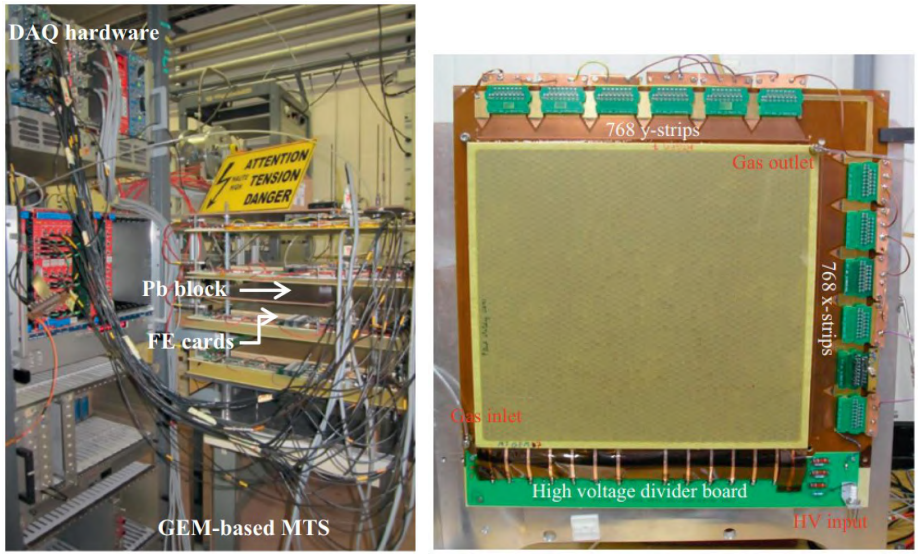

Figure 3.34: The GEM detector prototype for muon scattering tomography [114].

3.2.2 Quality assurance for GEM detectors

The REGARD group is actively conducting the research and development of MPGD detectors for multiple scientific purposes. The TCPD (Thick GEM + CCC Photon Detector) has been developed to unite the features of the micro-pattern GEM technology and the stability of the CCC wire chamber as readout [115]. This provides a robust and efficient detector concept for single photoelectron detection in Cherenkov detector applications. Our group is also developing a double-GEM Tandem TPC with 1 dm^3 drift volume and custom designed FPGA (Field-Programmable Gate Array) data acquisition for particle beam diagnostics [116]. We also took part in the TPC upgrade project of the ALICE experiment for Quality Assurance (QA) of GEM detectors, which means that approximately 32 m^2 of four-layer GEM detectors (130 m^2 of GEM foils) has been subjected to quality control.

The complex geometry of micro-structures make the optimization of parameters challenging, while the detailed investigation is still an active part of recent R&D. MPGDs use production technologies which are under continuous development, leading to a steady improvement in the detector quality. Such measures of quality include operational stability (sparking rate), gain uniformity, and production defects. It is often unclear how these are related: do these defects lead to destructive instability, or simply to a minute loss of efficiency. A Gain Scanner detector has been developed [117] for the QA of ALICE TPC upgrade to control GEM production defects and gain uniformity. Together with an optical scanning system (measuring precisely the GEM hole diameters), developed by the Helsinki Institute of Physics (HIP) [118], the Budapest Quality Center has been established with a cleanroom and supplementary equipment [119] which contributed to the selection of the best GEM foils for the ALICE detector system. The system is shown in Fig. 3.35.

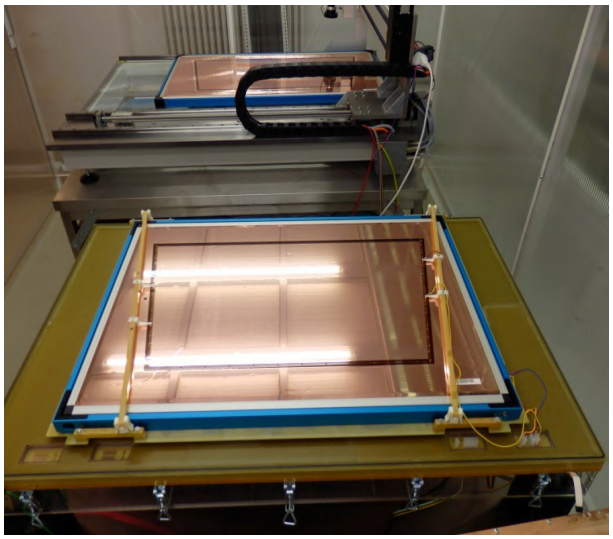

Figure 3.35: The Helsinki Optical Scanner in the back and the Wigner Gain Scanner in front in the cleanroom of the Budapest QA Center.

The problem with the previously existing GEM examination tools is that they are not able to provide precise local gain information below the resolution of the micro-structure segmentation, which are important data not just for QA, but also for the optimization of the micro-structures, the validation of simulations, and the effective improvement of the GEM detectors. Based on the fact that GEM (first demonstrated in the so-called 'Thick GEM'[120]) is applicable for Cherenkov detection [121], a high resolution surface scanning system of Thick GEM with focused UV light for single photoelectron detection has been developed in our group [122]. The Thick GEM layer under study is hosted by a TCPD detector (but it was also tested with

Micromegas readout [123]) and through a fused quartz window, a scanning system excites a photoelectron from the surface of the Thick GEM by a pulsing UV light. This way the scanning system can measure separately the GEM gain (order of 10–100) and the photoelectron detection efficiency unlike in the case of continuous illumination. The scanning system, nicknamed 'Leopard', maps the gain and the detection efficiency in sufficiently high resolution to identify the micro-structures and measure local detector properties individually hole-by-hole. Therefore, the Leopard is a promising tool for GEM QA (gain homogeneity, stability, and defect effects) and for micro-structure optimization. Optimization can result in the prevention of sparks and the mitigation of edge-effects (systematically different gains near edges) by well designed micro-structures which could be tested by the Leopard. I was motivated by the opportunity to join the research and development of this cutting edge technology, and the examples shown previously that MPGD detectors can be useful in muography as well. I further developed the Leopard scanning system to be able to measure standard GEMs as well, and within the framework of the EU funded AIDA-2020 (H-2020) and RD51 common project, we demonstrated a large-size prototype which is able to host ALICE and COMPASS GEMs, and now the Leopard is part of the Budapest Quality Center. In the following, I describe the current Leopard system, my development work, and the main results (effect of edges and defects in different GEM types) which can contribute to the improvement of the GEM detectors.

The schematic figure of the key components and a photo of the actual large-size Leopard system is shown in Fig. 3.36. The optical system is equipped with a UV source (pulsed LED or continuous deuterium lamp), a pinhole (with a diameter of 30–100 µm, depending on the desired size of the focused light spot), a focusing lens, and a digital USB microscope (for fast optical checking, and calibration). The optical system is movable linearly in three perpendicular directions, driven by 2.5 µm resolution stepper motors and ball spindles.

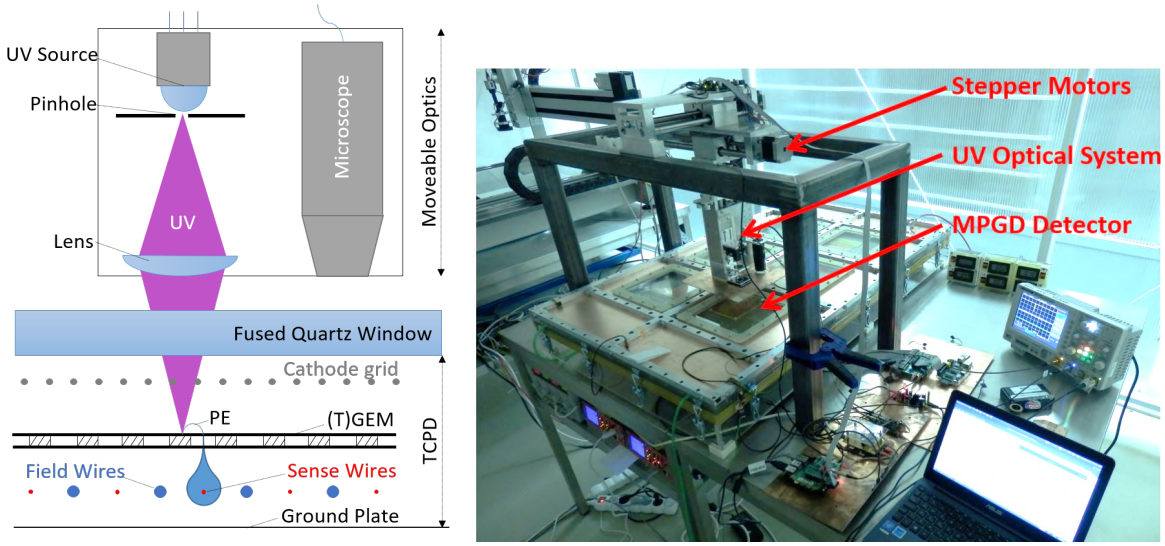

Figure 3.36: Left: Schematics of the main components of the UV optical system of the Leopard scanner. Right: Photo of the large scale prototype in operation with a Thick GEM from COMPASS RICH Hybrid [124].

The UV light is focused on the surface of the GEM inside the TCPD detector and the emitted single photoelectron is amplified in a hole. A CCC based post-amplification (amplification region after the GEM) and readout with a single channel is used after the GEM layer, but as mentioned before, Micromegas can also be used. There are two options for UV source: pulsed LED, or continuous deuterium lamp. My comparative analysis yielded the following results: using a pulsed LED the light intensity is lower, in exchange the signal reading can be triggered by a pulse signal (typically with 130 kHz) so the electrical noise is clearly separable and detection efficiency can be calculated. In continuous illumination with a deuterium lamp, we use self-trigger. Therefore noise separation requires extra calibration but the signal readout is significantly faster due to the higher UV light intensity.

The DAQ system coordinates the movement of the actuator, the LED pulsing, the data collection, and the analysis. The photoelectron spectra (signal amplitudes) are recorded in every pixel of a predefined 2D region on the GEM with custom designed PCB boards [125] responsible for power supply, signal shaping, ADC, and a RaspberryPi which collects the digitized data. Several thousands of events are recorded in each point, but the light intensity and duration is calibrated so that only ca. 1% of them are photoelectrons (to avoid multi-electron events). By analyzing the histogram data, the photoelectron yield and the detector gain can be determined. Photoelectron (PE) responses are shown in Fig. 3.37 with varying photon yields. The noise (zero PE case) is clearly recognizable as a Gaussian distribution around the pedestal. The distribution has an exponentially decaying tail with a good approximation, as expected from the avalanche statistics [93].

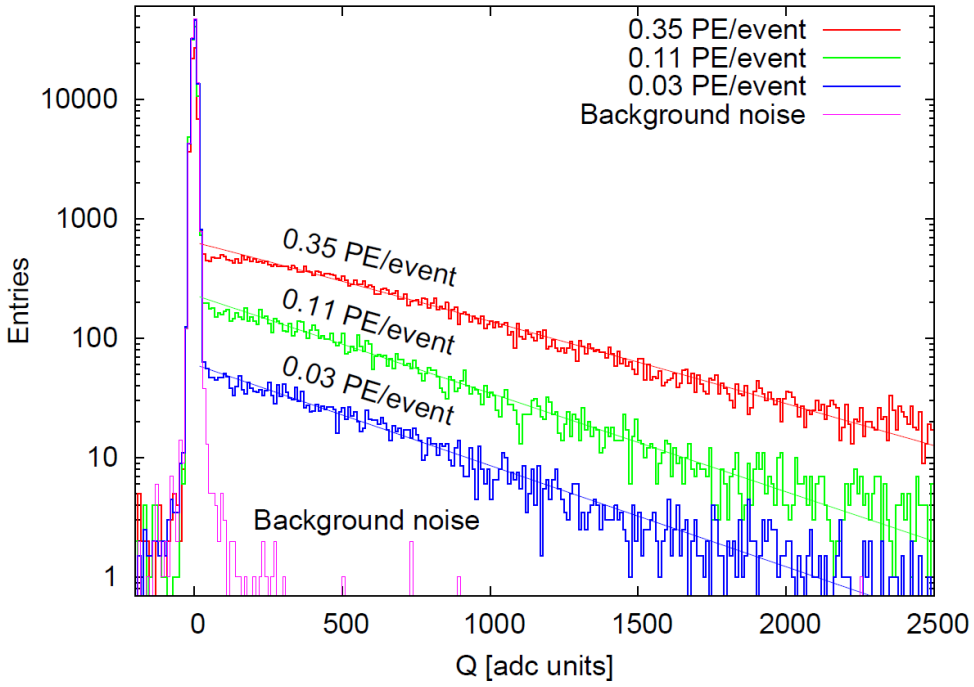

Figure 3.37: Example spectra of single photoelectron (PE) responses with different UV light intensity. The Gaussian noise is clearly distinguishable from the exponential photoelectron signal [122].

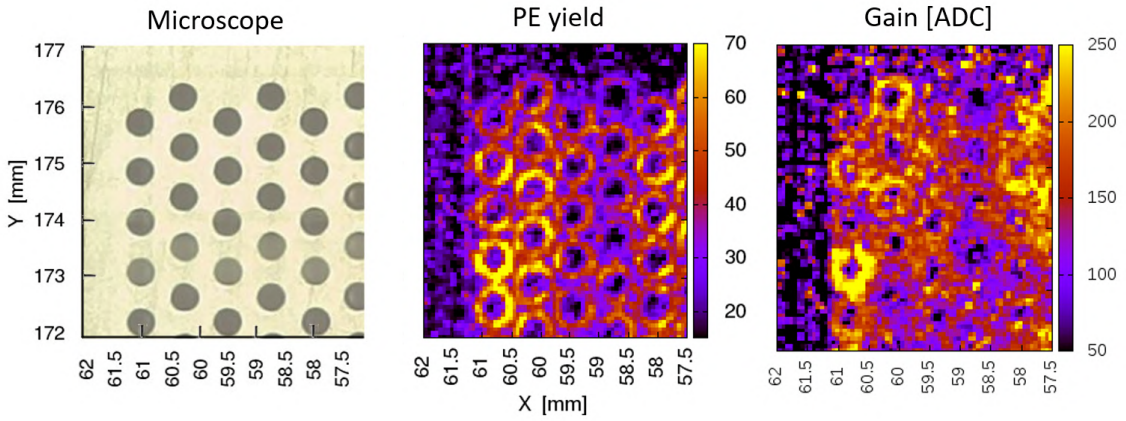

Figure 3.38: A gold-plated Thick GEM corner scan (800 µm pitch, 400 µm hole diameter). The holes can be identified in the PE yield map and the gain is constant around each hole [124].

The GEM gain and PE yield can be computed by cutting the Gaussian noise from the spectrum and fitting an exponential function on the histogram ($f(Q) = \frac{Y}{G}\mathrm{e}^{-Q/G}$, where Y is the PE yield, G is the gain, and Q is the Coulomb charge of the signal). The photoelectron yield is computed as the integral of the density function above the cut (that is, the total number of photoelectrons during the measurement). The gain is independent from the yield, as Fig. 3.37 indicates (the slope does not change in different light intesity). To obtain purely the GEM gain, the effect of the post-amplification stage can be eliminated from the total detector response with a preliminary measurement by applying low voltage (around 50 V) on the GEM. This way the PE is amplified only in the post-amplification region.

The results of the GEM gains and PE yields over the scan region are visualized as colormaps where colors represent the resulting quantities. Such maps are shown in Fig. 3.38 with comparison of a microscope photo of the examined area of a gold-plated thick GEM. As it is evident in the maps, the micro-structures are well recognisable (PE yield map looks similar to the spotted pattern on a leopard's fur, hence the nickname of the scanner) and quantities describe the local behaviors: no yield in the center of the holes, also inconclusive in the symmetry centers, and the gain is uniform around a hole but fluctuates from hole to hole. The results are pointing to the fact that the gain depends more on the hole geometry and less on the position where the electron enters.

The optical system needs careful calibration and focal adjustments for the best performance. I designed adjustable 3D printed optical elements, so the optimal object-image distances of the UV light spot can be fine-tuned. My developments aimed to enhance the system resolution so not just Thick GEMs (300–400 µm hole diameter) but standard GEM foils (50–70 µm hole diameter) could be scanned. Furthermore, not just gold plated surfaces but the widespread copper-plated ones (much lower quantum efficiency, thus PE yield) could be measured efficiently due to the enhance photon densities. I achieved these developments by applying an aspheric lens, smaller pinhole, focused UV source, optimized focal length, and covering aluminum elements which can blur the imaging due to reflection.

Next I describe the focal calibration which validates my efforts for higher scanning res-

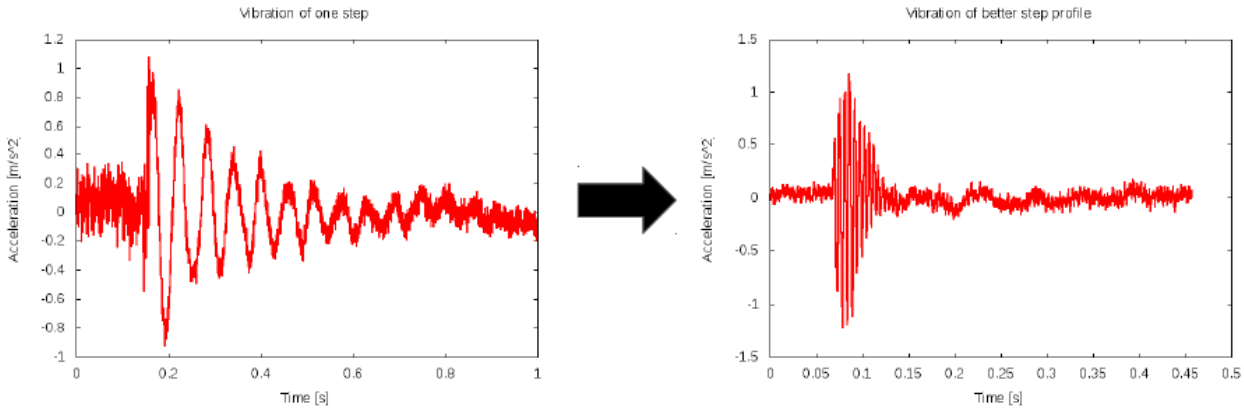

Figure 3.39: An optimal delay time profile for the stepper motors was determined by modal analysis to achieve faster vibration decay. The figures show the damping of the vibrations after stopping the optical head, measured with accelerometers, without (left) and with (right) the application of vibration damping step profile.

olution. First, I considered the vibration of the system due to the scanning steps which blurs the image. As a result of the modal analysis of the system (which was carried out by P. Sántha under my supervision[10]), we could determine the optimal delay time after a step when the vibrations subside, and an optimal speed profile has been determined to increase the damping (Fig. 3.39).

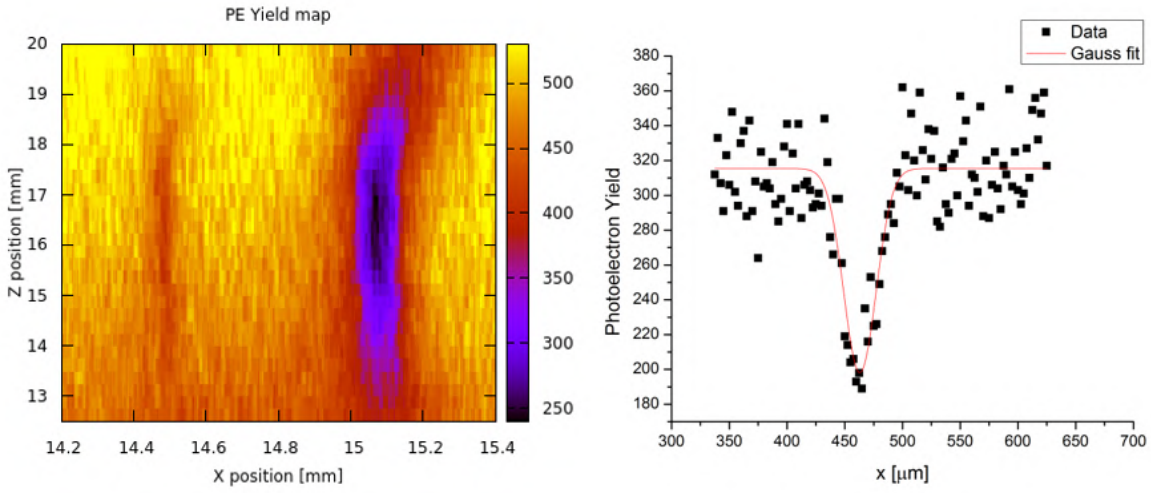

Figure 3.40: Left: An X-Z measurement of the photoelectron yield to determine the focus and resolution. Right: Photoelectron yield as a function of X position on the focus level of the X-Z map (Z = 16.5 mm), with a Gaussian fit. The highest resolution of the Leopard system is presently 30 µm FWHM as extracted from the fit.

[10] https://regard.wigner.hu/Publikaciok/Disszertaciok/ P. Sántha, BSc Thesis, HU (Accessed: 2023-05-30)

These upgrades proved to be useful to reduce the scan time and to sharpen the measured images. The scanning resolution must adapt to the size of the light spot. I used thin wires (thickness of 25 μm and 100 μm) horizontally above the detector to quantify the resolution (size of the light spot) [122]. The photoelectron yield is measured perpendicularly (X direction) to the wires at different vertical positions (Z direction). An example of a measured X-Z photoelectron yield map is shown in Fig. 3.40.

The focus level is where the FWHM of the shadow of the wires is the lowest. The resolution of the Leopard system, by definition, is the FWHM of the photoelectron yield drop of the 25 μm wire when the system is in focus. It is practical to adjust the focal level of the microscope camera to the same level so one can find the focus easily with the video stream of the microscope. As shown in the figure of the focus measurement, 30 µm FWHM resolution could be achieved which is below the standard GEM hole sizes. Thus they can be examined as well.

In the following, I describe in a few words the regular operation of the Leopard, considering the measurement time and important steps required for the setup of the Leopard. First of all, the GEM to be tested must be installed into the TCPD in a cleanroom, and the hardware and cabling must be assembled. The detector must be flushed with gas for a sufficient time and high voltage must be applied to the GEM and to the anode. After the system is fully operational and the focus is set, a reference point must be found on the GEM with the microscope camera from where the optics can be navigated to the measurement area. The stability of the measurement must be ensured with a few minutes of continuous illumination. When the measurement parameters are selected, the stepping resolution, the size of the statistics, and the scan area needs to be considered depending on the size of the micro-structures. The surface material also influences the procedure, because different materials have different quantum efficiencies (for example, copper has lower quantum efficiency than gold resulting in fewer photoelectrons). The duration of each measurement strongly depends on the selected parameters and the surface quality. It is given by the statistics per trigger frequency multiplied by the number of pixels (movement time is approximately 10% of the total data collection time). One pixel is measured in around 0.2—2 s. The time required for a good quality scan time strongly depends on the above mentioned aspects, but typically it takes about 5–30 minutes with a deuterium lamp. We have two variations for readout detector chamber. A small-scale prototype chamber can host GEMs and Thick GEMs up to the standard 10×10 cm^2 (Fig. 3.41 left) for R&D purposes, or in the case where high signal-to-noise ratio is needed.

The new large-scale prototype chamber has an active area of 90×48 cm^2 in which the GEMs from CERN ALICE TPC1[118], and Thick GEMs from CERN COMPASS RICH Hybrid [126] (Fig. 3.41 right) can be measured. The MPGD layer is held in place via an interchangeable layer (the Support Plate), to any shape and size within the limits that can be investigated. The cathode top box is interchangeable and has six openings for UV transparent quartz windows (Fig. 3.36 right).

Finally, I present my results about some of the relevant GEM examinations. I demonstrated the practical application of the achieved high resolution on standard geometry GEM detectors. Fig. 3.42 shows that the micro-pattern structure is still clearly identifiable even on this scale, the scan can effectively be carried out on relatively large areas (not just a few holes), and the detector response (PE yield and gain) remains stable.

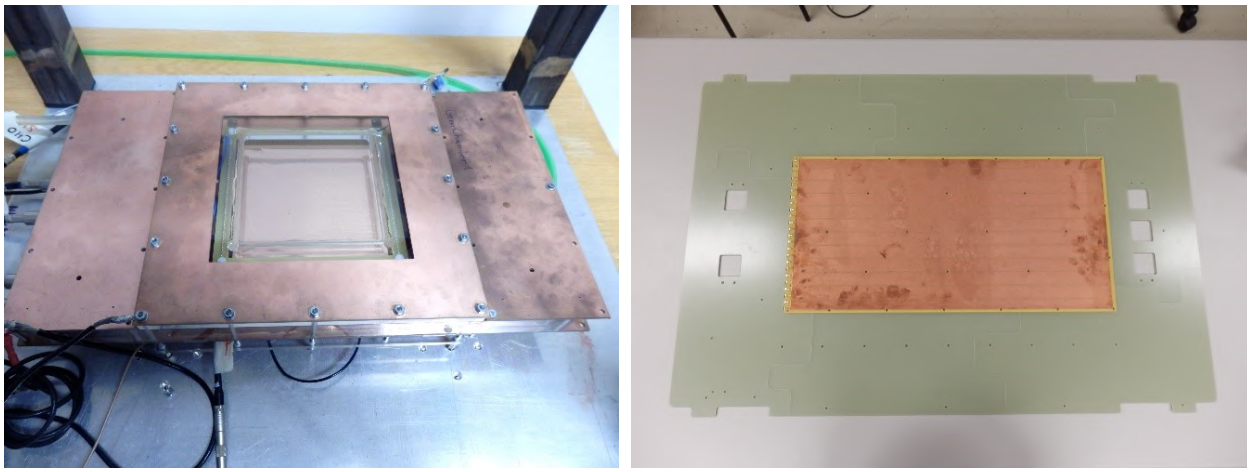

Figure 3.41: Left: Photo of the small scale Leopard detector containing a standard 10 × 10 cm^2 GEM. Right: Thick GEM from COMPASS RICH Hybrid on the Support Plate.

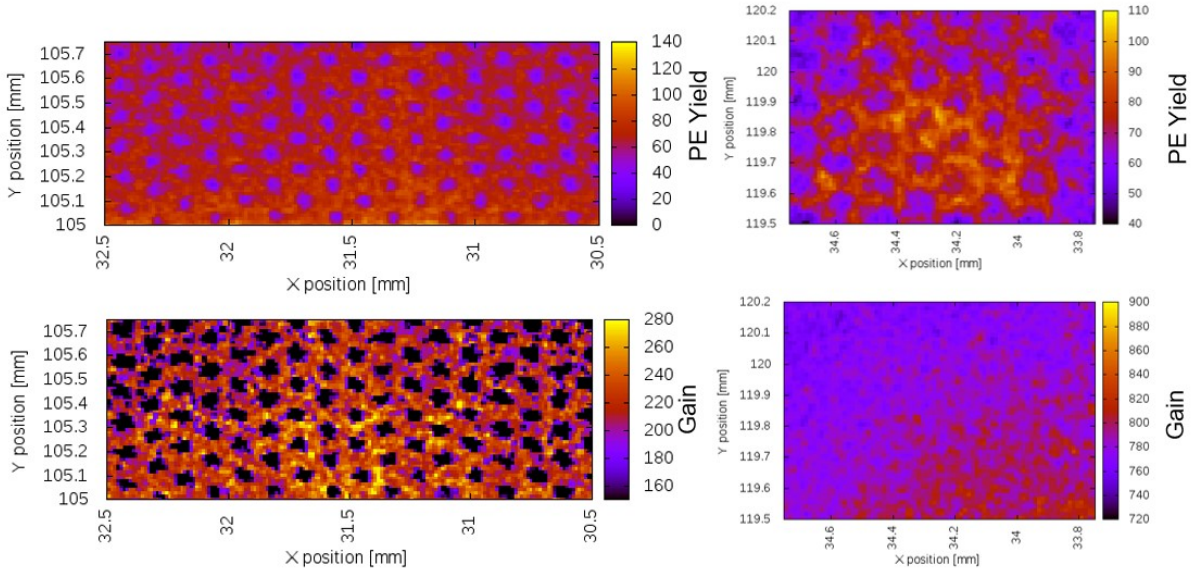

Figure 3.42: Leopard scan on standard geometry (60 µm hole diameter) GEM layer, PE yield map (top) and GEM gain (bottom). Left is a a gold-plated, the right is a copper plated GEM scan. This demonstrates the imaging applicability of the Leopard in this scale.

I also checked the spatial and time stability of the GEM measurement system. The local gain variation has been measured in a one dimensional line scan repetitively using different optical arrangements to check the spatial reproducibility of the measurements. As shown in Fig. 3.43, the gain values fluctuate equally within the significance level with different light intensities. The time stability is checked by standing in one point above the GEM active surface with the Leopard, and consecutive one-minute measurements has been performed without movement. The possible gain time instability is also a known issue with GEM

detectors. The phenomenon is called "charge-up" [107] which means that due to high rates, the insulator inner wall of the GEM holes can electrostatically charge up as a result of adhering ions, and this distorts the electric field inside the hole where the electron avalanche takes place. On Fig. 3.44 right, a charge-up measurement shows that gain variation is small (with this particular GEM), and this variation also saturates over time. One of the strengths of the Leopard is that this effect can be examined on different GEMs or within a particular GEM location independently.

However, an even more interesting phenomenon has been observed with the Leopard: the photoelectron yield can also change over time. This practically means that the quantum efficiency of the electron release from the surface in continuous UV illumination is growing, as shown in the time dependent PE yield plot during the charge-up measurement in Fig. 3.44 left. This effect is not yet fully understood and needs more investigation, especially because effects increasing quantum efficiency may be very useful in multiple applications. I observed this effect in different GEMs and Thick GEMs with Cu and Au surface materials in Ar:CO_2 (FC18) gas mixture, which generally inhomogenous in terms of the PE yield change distribution. Preliminary it can be stated that the PE yield is growing in time due to UV illumination, and surface treatment (cleaning with propanol and polyester wipers) homogenizes this effect, so it is expected that some kind of surface deposition charge-up is behind this effect. Nevertheless, increase in the PE yield is not significant (until single PE excitation occurs) from the point of view of gain measurement, because it is measured independently.

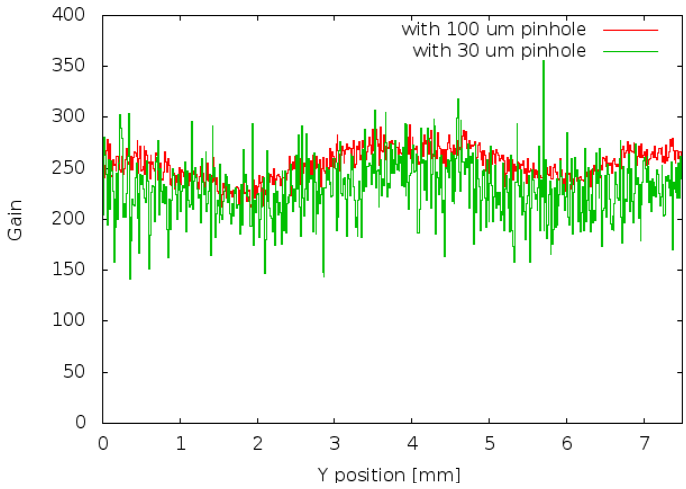

Figure 3.43: Spatial gain reproducibility measurement. The gain is measured to be approximately the same in two different light intensity scans (but the noise level with 30 um pinhole is larger than that in 100 um)

The high resolution gain map allows us to directly measure the "edge-effect", i.e., the gain of holes located near an edge compared to the middle ones. According to simulations it is expected, that the electric field differs in the edges, because of the lack of holes in one side, but the extent of the distortion and its effect on the gain remain unknown. This so-called "edge-effect" can be examined with the Leopard system which is demonstrated in Fig. 3.45 that exhibits a Cu GEM with four different hole size segmentations. This shows gain

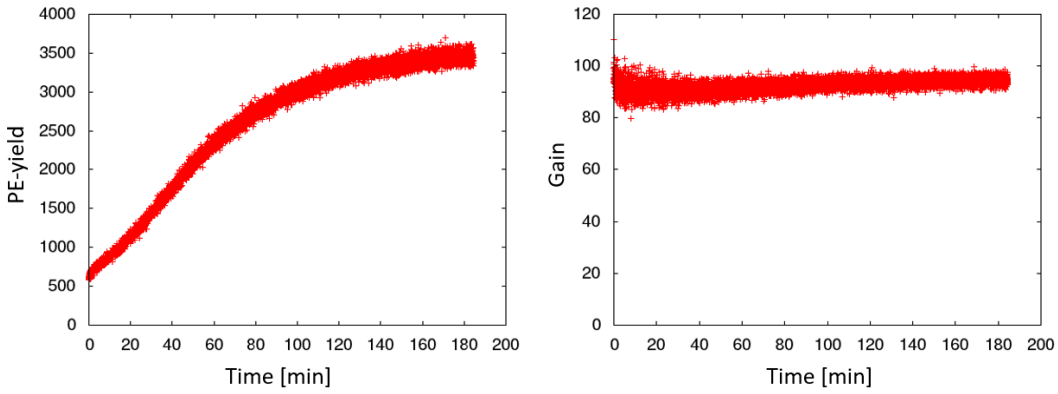

Figure 3.44: Time stability of PE yield and gain under continuous UV illumination of a GEM surface. Left: the PE yield change. Right: the gain charge-up is shown.

dependence on the distance from corners and edges which also varies on the shape of the hole arrangement and size. A more detailed study is expected about the edge-effects in the future, with the aim of designing an optimized MPGD geometry to reduce gain inhomogeneities.

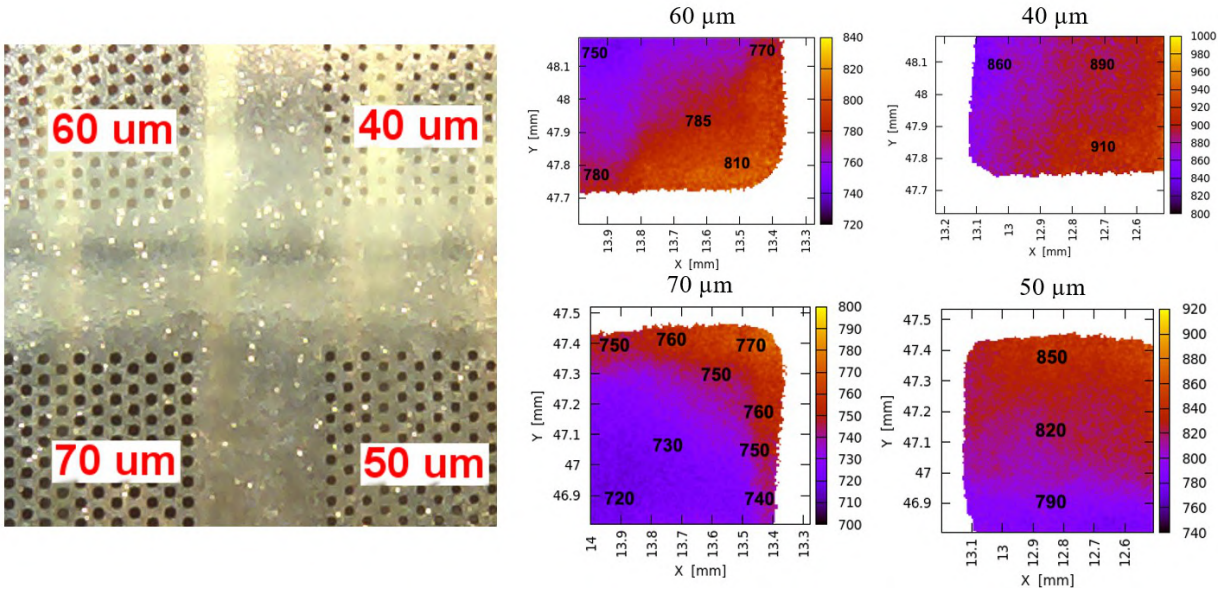

Figure 3.45: Cu GEM measurement with four different hole diameter segmentations.

Another important goal of the Leopard system is to measure GEM defects resulting from manufacturing. The Leopard system offers a possibility to measure the effect of these defects on the microscopic scale. Fig. 3.46 shows an example scan of a rip in the GEM (due to over-etching), and the corresponding PE yield and gain maps around the defect. The PE yield and gain drop down drastically in a few hole surroundings around the defect. However the hole GEM is still operational in this case. In the future, the Leopard can join quality assurance task even for large-scale industrial applications.

In summary, the Leopard high–resolution gain scanner is a powerful tool for comparison

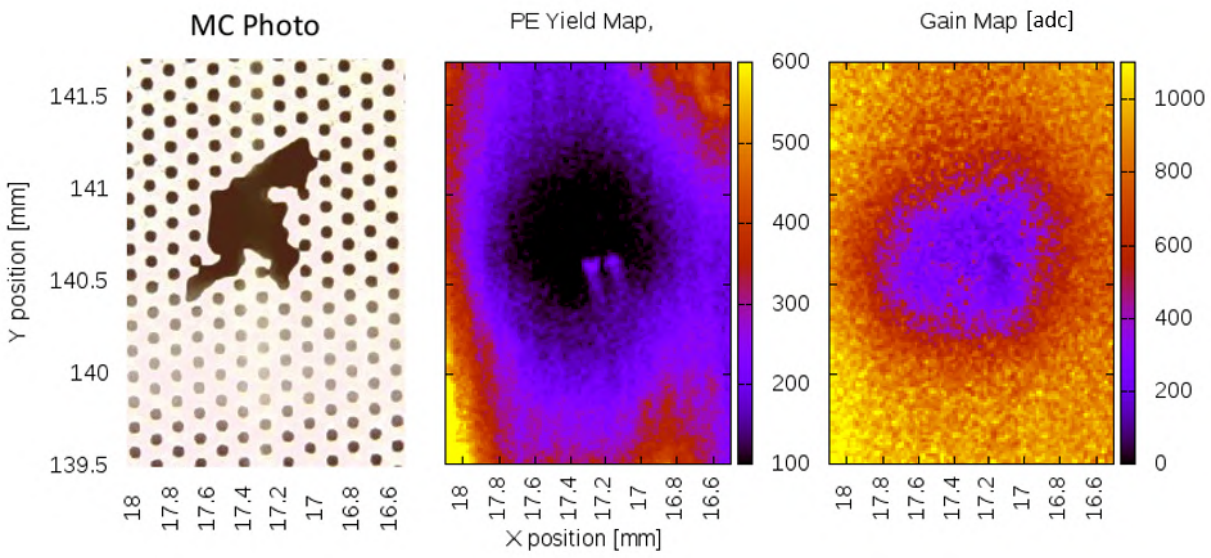

Figure 3.46: Example measurement around a large over-etching defect on a standard GEM foil showing the microscope photo, the PE yield map, and gain map [124].

of MPGD geometries, GEM quality control or for the studies of local detector effects. The basis of operation is single photoelectron PE emission from the GEM surface by a spot UV light. The close-to-exponential PE spectra are measured and the PE yield and gain are calculated for each pixel of a 2D region with a RaspberryPi based DAQ system. The results are visualized as a map of the measured quantity. Thick GEM and standard GEM scans demonstrated that holes are identifiable and gain is constant around each hole. Example high–resolution gain maps showed the effects of edges and local production defects. The Leopard system is applicable for large area MPGDs as well. Thus it can enhance the quality control of mass production.

Chapter 4

Muographic imaging data evaluation

4.1 Radiographic image production

In the previous chapter, we discussed the hardware developments of contemporary gaseous detector systems which resulted in high performance detectors (tracking efficiency, stability, resolution, homogeneity) detectors with low cost, low gas and power consumption, and low weight, which are well applicable even on the field. Now we row on the topic of the data evaluation provided by the muon tracking detectors to produce muographic images which can be interpreted by geoscientists, archaeologists, or civil engineers. In the first section of this chapter, we elaborate on producing a muon flux image from one detector view: a 'projectional radiographic' image that is related to the integrated material density in the given directions of the image pixels. This can already provide useful information concerning the interior of the imaged rock layer by temporal imaging (e.g., magma dynamics, water level monitoring) or directional observation of relative density anomalies compared to a reference region.

The process of a radiographic image creation is discussed in this section: calculation of the muon flux from the raw tracking data, converting the muon flux to the density-length (opacity), taking into account the errors, and comparing the results with *a priori* information. The data processing is also important in "reverse mode" for the planning of a muographic survey. Furthermore, for the determination of the spatial distribution of rock density (the distance from the detector, not just the direction), we need multi-view measurements concerning the observed object (e.g., a cavity or high density ore body). The tomographic methods we tested are discussed in the next section.

4.1.1 Muon flux calculation and conversion to rock density

As a first step I introduce the tracking algorithm by explaining some tips and tricks to determine the muon flux, i.e., the normalized muon rate in a given direction, as defined in Eq. 2.2. Recalling that the basic tracking data provided by the DAQ from Sec. 3.1 consist of 6–8 layers of 2D hit patterns (clusters) for each track event if at least 3 or 4 coincidence are detected, and the tracking software calculates the 3D straight line tracks (after preprocessing) which are later grouped into angle bins for muon flux calculation. In more detail, a linear fit can be decoupled into X and Y projections (where Z axis is generally perpendicular to the detector layers) with possible fine-tuned chi-square cuts separately due to the slightly

different nature of signal pickups. Different filtering algorithms are also applied to reduce noise and secondary electrons which tend to have a large-size cluster. The track selection is quite conservative due to a combinatorial algorithm: finding the sequence of K out of N (usually 6 of 8) hits providing the best straight line fit disregarding the most outlying point, if exists. Thereby, even a higher tracking efficiency can be ensured for the total detector system than that of a single chamber. A linear fit on the hit combinations produce the track candidates – the smallest chi-square is favoured – and if it is below the chi-square threshold that is selected as the reconstructed muon track [74]. Track candidates with higher number of clusters (chambers) could be favoured with non-equal chi-square thresholds. In the next step, the "fiducial area" of all detector chambers are defined, such that the local efficiency is above 75% (excluding, e.g., the wire support regions or malfunctioning channels). Finally, only those tracks out of the reconstructed tracks are selected which crossed the fiducial area of all the 8 detectors. The reason for the rather strict selection criteria are the reduction of the systematic errors from the estimated efficiency, at the cost of reduced statistics and viewing angle because the tracking efficiency affects the muon flux calculation. Therefore, the data are used to continuously monitor the performance (depending on both hit location and time) of the chambers by excluding any chamber from the tracking and then perform the tracking without it, this way checking the efficiency of the excluded chamber (being an independent entity) [87].

Since all tracks are summed over the detector surface when the muon flux is calculated for a given angle bin, the calculated muon flux must be normalized. The detector acceptance is defined as the active surface of the detector system for incoming muons at a given angle [82]. The acceptance can be described in a simple case for 8 point tracks

$$A_{\text{eff}} = \varepsilon \cdot \max(L_x - d \cdot s_x, 0) \times \max(L_y - d \cdot s_y, 0), \tag{4.1}$$

where $s_x = \cos\beta \cdot \tan\alpha$; $s_y = \sin\beta \cdot \tan\alpha$ are the tangent slopes (α is the angle with the Z axis, and β is the rotation angle around the Z axis), L_x, L_y are the detector side dimensions, d is the telescope length, and ε is the total tracking efficiency. Note that the acceptance is slightly larger if the required number of track points is reduced [127].

Assuming the detector is placed horizontal or close to horizontal, the muons are measured coming from a ∼90°cone, and discretized (binned) into disjoint solid angle ranges ($\Delta\Omega$, steradian) – on which the detector integrates the muon arrivals – with the geodesic direction angles of zenith (θ) and azimuth (ϕ) in the center. The size of these solid angles depends on our choice, considering the required statistics or the most convenient gridding, but limited by the detector angular resolution. The final ingredient to determine the muon flux from the detector data (Eq. 2.2 left) is to normalize with the measurement live time (total time minus dead time), which can be estimated from the distribution of the event time differences. Therefore, the measured muon flux $\Phi(\theta, \phi)$ is the total number of muon counts in the given measurement live time τ, solid angle bin $\Delta\Omega$, and effective detector surface $A_{\text{eff}}(\theta, \phi)$ corrected with the tracking efficiency ε. If we are interested in time-dependent effects (muon flux variations, or checking the stability of the tracking efficiency), the time bins of the data allocation must be chosen adequately.

This is where my work is involved in the muographic data processing. In the next step, I provide an overview concerning strategies how to derive conversion between the muon flux and the density-length of the imaged rock ($\Phi \leftrightarrow \varrho$) in a given direction. The reason for the

plural is that unfortunately we cannot obtain an exact formula because of the complexity of the issue. First of all, the function of the density-length and the muon flux is nonlinear and strongly depends on the zenith angle (θ) of the arriving muon ($\cos^2\theta$ tendency at lower muon momenta and secant-like in higher energy ranges). Thus, a simple formulation of the function is not resulting in an an accurate conversion method. The problems are compounded by the presence of multiple potential systematic uncertainties which must be checked or corrected. These are discussed later in this section. A direct measurement of the function, or the direct validation of the model is also unfeasible because of the high range of the parameters usual in muography applications (10–1000 m path lengths, 0–80°zenith angles). Therefore, only indirect measurements can validate a specific muon flux calculation method, usually in a specific muon energy range.

There are two different main approaches for muon flux estimation in the muographic literature: the integrating methods and simulation tools. The integrating methods are based on a cosmic muon spectrum $\varphi = \varphi(E_0, \theta)$, depending on the initial muon energy (E_0) and zenith angle (θ), and a function of minimum muon energy ($E_{\min}(\varrho)$) required to survive a given density-length (ϱ). Thus, the integrated muon flux can be derived as follows

$$\Phi(\theta, \varrho) = \int_{E_{\min}(\varrho)}^{\infty} \varphi(E_0, \theta) dE_0. \tag{4.2}$$

The muon spectrum can be obtained from cosmic ray physics based computations or empirical parametrizations. Based on literature research, I outline the most frequently occurring models, which I found to be accurate enough for muography and later implemented to create my own flux-opacity converter software. One of the most common base models is from Gaisser [128]. It is widely used for cosmic background estimation for underground measurements, but the model is only valid if the curvature of the Earth is neglected, i.e., the initial zenith angle $\theta < 70°$) and the muon decay is negligible ($E_\mu > 100/\cos\theta$ GeV). Therefore, in muography applications, some kind of modification is required. One of the modified Gaisser models is from Guan [129], where the muon spectrum is described as

$$\frac{d\Phi}{dE_\mu} = 0.14 \left[\frac{E_\mu}{\text{GeV}} \left(1 + \frac{3.64\text{GeV}}{E_\mu (\cos\theta^*)^{1.29}}\right)\right]^{-2.7} \times \left[\frac{1}{1 + \frac{1.1 E_\mu \cos\theta^*}{115\text{GeV}}} + \frac{0.054}{1 + \frac{1.1 E_\mu \cos\theta^*}{850\text{GeV}}}\right] \tag{4.3}$$

with θ^* taking into account the curvature of the Earth (due to the geometric difference of the zenith angles between the surface of the Earth and higher altitudes where the muon is produced)

$$\cos\theta^* = \sqrt{\frac{(\cos\theta)^2 + P_1^2 + P_2(\cos\theta)^{P_3} + P_4(\cos\theta)^{P_5}}{1 + P_1^2 + P_2 + P_4}}, \tag{4.4}$$

where the coefficients are:

$$P_1 = 0.102573\ P_2 = -0.068287\ P_3 = 0.958633\ P_4 = 0.0407253\ P_5 = 0.817285. \tag{4.5}$$

Another strategy to derive the muon spectrum is an empirical fit to the experimental data. Reyna [130] found a simple parametrization covering all zenith angles and a wide range of muon momenta (1–2000 GeV/cosθ). He based his formula on Bugaev [131] where a

parametrization was derived from nuclear cascade models for the propogation of high-energy nucleons, pions and kaons in the atmosphere. Reyna enhanced this work by introducing

$$\varphi(E_\mu, \theta) = \cos^3(\theta)\varphi_V(\zeta) \tag{4.6}$$

angle relation, where $\zeta = E_\mu \cos\theta$ and φ_V is the vertical muon flux formulated by Bugaev

$$\varphi_V = c_1 \zeta^{-(c_2 + c_3 \log_{10}\zeta + c_4 \log_{10}^2\zeta + c_5 \log_{10}^3\zeta)}, \tag{4.7}$$

and the coefficients

$$c_1 = 0.00253\ c_2 = 0.2455\ c_3 = 1.288\ c_4 = -0.2555\ c_5 = 0.0209 \tag{4.8}$$

are improved by fitting to six different experimental cosmic ray data sets. The comparison of the Guan and Reyna spectra is shown in Fig. 4.1.

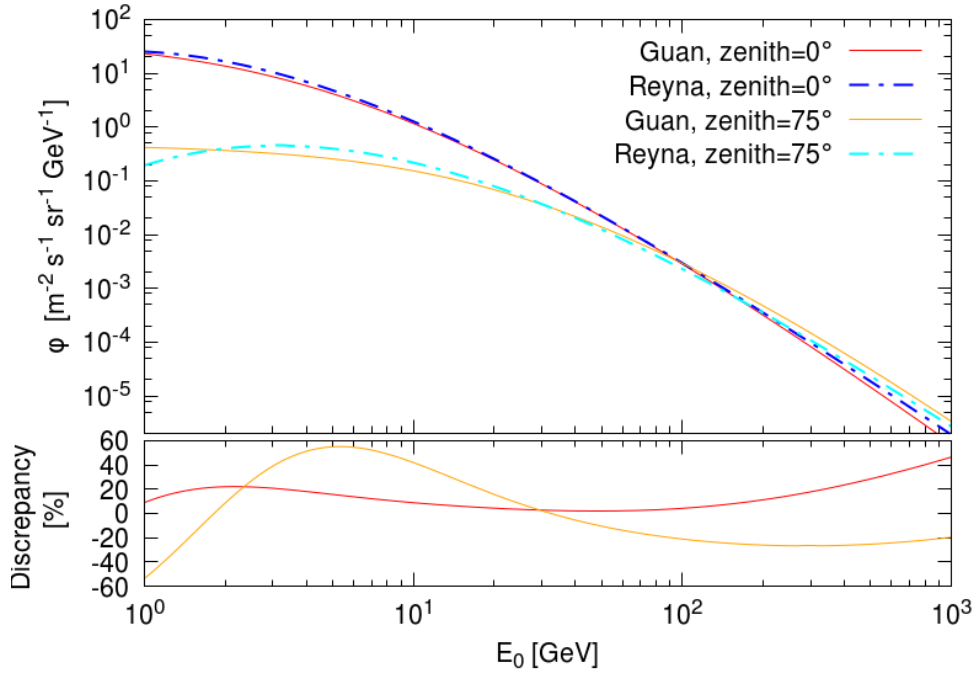

Figure 4.1: Differential muon spectra at sea level from the Guan and Reyna parametrizations at 0 and 75 degree zenith angles. The discrepancies (ratio between the two calculation methods) are shown in the bottom figure.

The minimum energy function can be derived from the energy loss for standard rock, governed by the ionization interaction of muons and the rock, provided by the Particle Data Group[1], for a variety of materials and a wide range of energy. I applied the parametrization

[1] http://pdg.lbl.gov (Accessed: 2023-05-30)

by Lesparre [5] which uses the so-called 'standard rock' ($\langle Z/A \rangle = 0.5$ and $\rho_{sr} = 2650$ kg m^{-3}), and a fourth order polynomial fit to the energy deposition function

$$\frac{dE_{sr}}{d\varrho} = -10^{l_4 y^4 + l_3 y^3 + l_2 y^2 + l_1 y + l_0}, \tag{4.9}$$

where $y = \log E_{sr}$, with E_{sr} in GeV, the parameters are:

$$l_4 = 0.0154 \; l_3 = -0.0461 \; l_2 = 0.0368 \; l_1 = 0.0801 \; l_0 = 0.2549, \tag{4.10}$$

and the relative error never exceeding 2% (Fig. 4.2 left). After that, the minimum energy required for a muon to reach a given density-length is derived by

$$E_{\min} = E_{\mu_0} + \int_0^{\varrho} \frac{dE_{sr}}{d\varrho} d\varrho, \tag{4.11}$$

where E_{μ_0} is the muon rest energy. This provides the association between minimum energy and density-length which is essentially used in Eq. 4.2. Fig. 4.2 right shows $E_{\min}$ as a function of the standard rock thickness. Note that this kind of minimum energy assumes a sharp cut of the surviving muons (zero muons are assumed to be detected after a given density-length if their initial energy is lower than the cut), but more sophisticated models can be obtained by simulations [103].

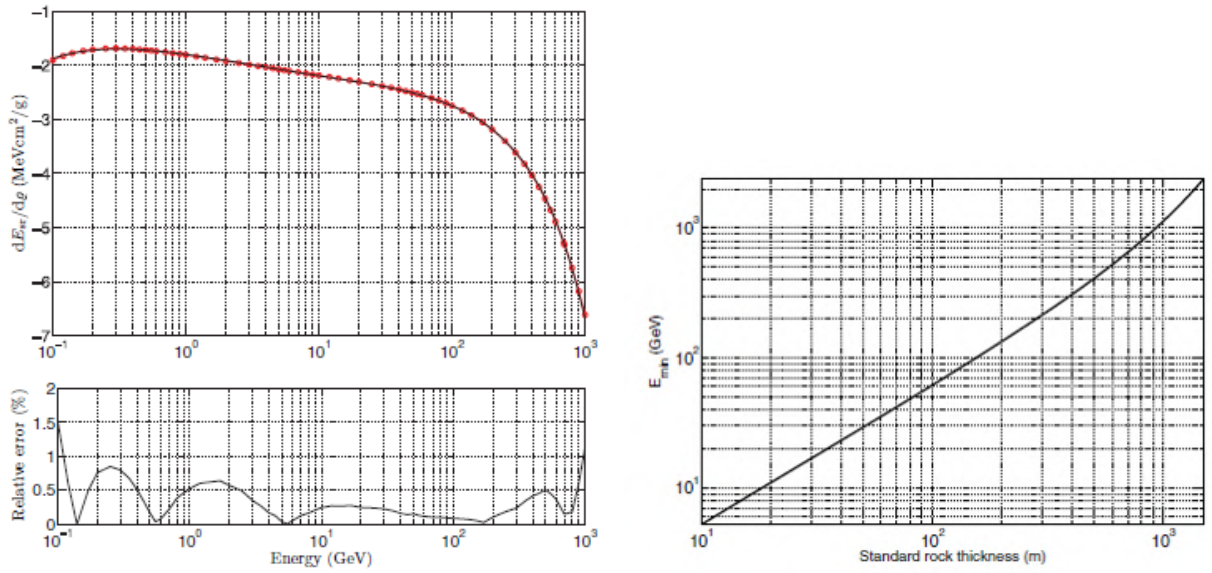

Figure 4.2: Left Top: energy loss for standard rock provided by the Particle Data Group (symbols) and fourth-order polynomial fit (solid line). Left Bottom: relative error between Particle Data Group values and the polynomial approximation. Right: Minimum energy obtained by solving Eq. 4.11 as a function of the standard rock thickness [5].

Due to the extensive literature of muon flux spectrum measurements and parametrizations, this review is not supposed to cover all calculation methods but only those that I tested

and applied to our detectors so far. Eq. 4.2 provides the relation between the density-length and the muon flux. The representation of the integrated muon fluxes at different zenith angles and opacities are shown in Fig. 4.3 right.

Monte Carlo simulations are a more sophisticated, but also more complicated method for the flux calculations. The different stages of the muon's life can be simulated separately or altogether, beginning from the high-energy proton collisions in the upper atmosphere, through the cascade decay processes of particle showers in air, the attenuation of muon in the atmosphere (considering detection altitude, atmospheric pressure and temperature effects, geomagnetic effects, etc.), energy deposition and multiple-scattering in material, background particles, and detector response [3, 47, 48]. For example, CORSIKA software package is one of the state-of-the-art simulation tool for the production of extensive air-showers[132]. Simulation tools are especially profitable answering complex questions, or applying in unknown situations, but building up and verifying a model takes a lot of time and resource.

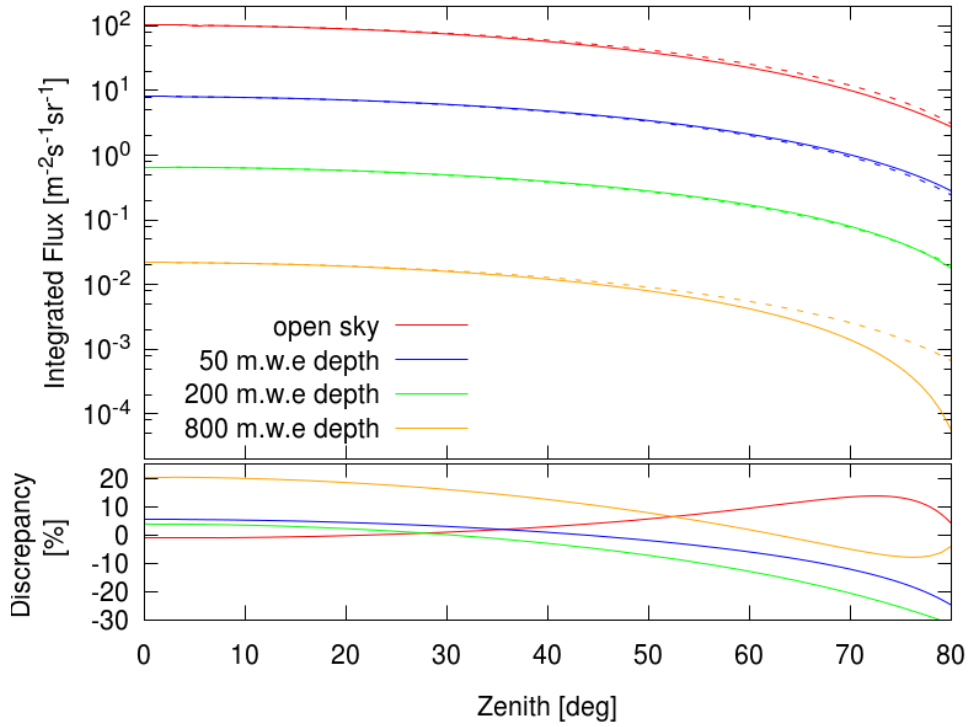

Figure 4.3: Integrated muon fluxes are shown in different depth, depending on the arrival zenith angle of the muon, calculated by the Guan method. A particular depth means a simplified detector placement scenario underground, assuming homogeneous rock density and a plane surface. Note, that the given depth is valid only in the zenith 0 direction, and the thickness is growing with the zenith angle by cosine. It is also interesting to note that in most cases the muon flux follows a $\cos^2$ tendency (dashed lines), and only in high angles and at long path lengths differs significantly. The relative discrepancies between the Reyna and Guan methods are shown in the bottom using the same colour notation as in the upper panel.

4.1.2 Muographic image production

Now we can obtain muon flux and density-length information from the directional tracking measurement data. However before we proceed to construct our muography image it is an important last step in most cases to compare the measured data with expectations (this step can be omitted for time-sequential muography but it is still recommended). This means that we must have geodetic information about the examined object, mainly about the surface (for the surface model or topographic corrections) but also underground structures if known as those clear the picture of what is known and what is unknown in the measurement data. Starting this in a simple case when we only have DEM data about the surface, the expected density-length comparable to the measurement in a given direction bin can be produced if we compute the distance between the surface and the detector and multiply it with the average density.

However, this is easier said than done because there is no simple software solution in the market, the DEM data always have to be checked for deviations, missing parts, overhangs, not to mention the dozens of different data and file extension formats or coordinate systems in which DEM data is received. It is also worth noting that some kind of interpolation is needed to determine the average surface intersection distance in the cone of the direction bin.

I have developed a software[2] which can handle the following subtasks for a set of directional vectors (appointed by the measurements) at a given detector location:

(A) Generate rock length from DEM input data (= expected rock thickness)

(B) Generate flux from a density-length value (= expected flux, forward problem)

(C) Generate density-length from a muon flux value (= measured density-length, inverse problem).

The software was written in C programming language, and it was developed and tested on Ubuntu operating system.

For subtask (A), the input is a point cloud file with UTM (Universal Transverse Mercator) X, Y, Z data or any similar coordinate system (like the Hungarian EOV 'Egységes Országos Vetület'), in metric dimensions. Note that different Digital Elevation Models exist, as the Digital Terrain Model (DTM) which describes the shape of the ground surface, or the Digital Surface Model (DSM) which includes landmarks like vegetation or infrastructure. For my software, the DTM can be used, since vegetation has insignificant impact on the muon flux (relative density-lengths are negligibly small), and the building structures are usually much more complex than the DSM data suggest. Therefore infrastructure needs to be considered in a different way (see CAD modeling later in this section).

My algorithm calculates rock thickness by integrating in a given directional vector step-by-step, starting from the detector position in the coordinate system of the DEM. At each step, the algorithm determines whether the step point is above or below the closest elevation

[2]Current version: FluxConverter-v20220510.run available on reasonable request.

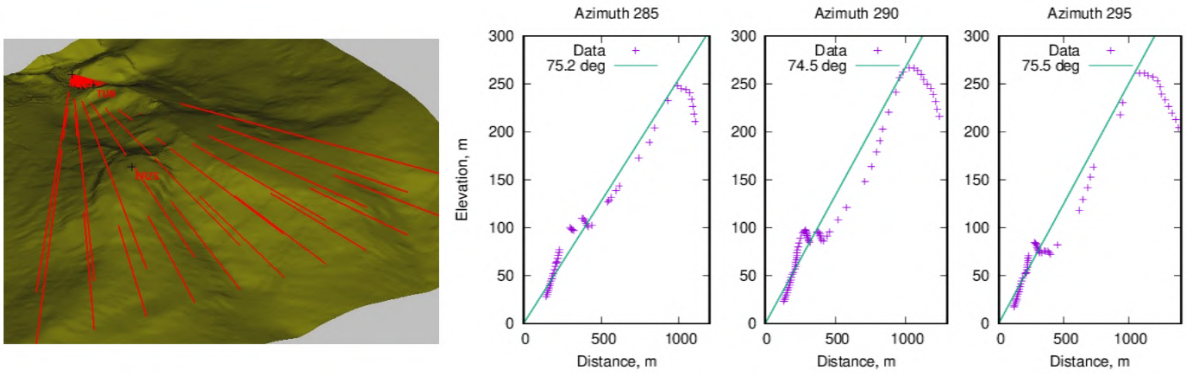

Figure 4.4: Topography around a surface measurement location. The red lines indicate muon trajectories which are detected at the observation site (the convergence point of the lines). In the interesting region, the muons travel in air in the valley between two hills (Tündér-szikla and János Hill, Budapest). The panels on the right show topographic elevation as a function of distance for selected azimuth directions.

points. If the point is below, it is considered to be in rock and the algorithm sums the length of the step size. If the point is above, it is considered to be in air and the integration does not sum. To calculate the most accurate surface intersection point, a function is used which searches the DEM at each iteration step and calculates the altitude data. Specifically, the function finds the distance of the four closest points in the four quadrants of the X-Y plane, and then calculates the average altitude of the surface above or below the iteration, weighted by the reciprocal square distances. A constant distance of 0.1 meter radius is used for smoothing. If the integration goes further than the available data set, the program uses one of the closest available data points. In the step when the surface is just crossed, the rock length is weighted with the distance below the surface. The direction bins can be imported from a measurement data file, or an artificial grid of bins can be generated.

An example about a topography and integration lines from the detector is shown in Fig. 4.4, with three different azimuthial sections showing the actual DTM data and an integration line from side view. Within a cone of direction with a fixed zenith and azimuth angle bin, the surface can fluctuate so it can occur that only one line of integration is not accurate enough. For this reason, multiple – settings dependent and evenly distributed – lines of integration are averaged in one solid angle bin. In conclusion, this algorithm provides a simple method to calculate the rock thickness in meters for a given set of directions. The advantages of this program scheme are the easy parametrization, and the capability for using in not just underground but surface detector setups as well, since it can handle multi-hill cross section scenarios (when the line of sight includes multiple hill-like topography with valleys between them). However, the disadvantage is that it cannot handle overhanging topography or cavities under the surface, since in that case the mapping from the surface to the X-Y plane is surjective, therefore the integration in those parts is undefined.

If complex geometries are to be considered, then my software cannot be used and the rock length calculation (buildings or underground structures) becomes more challenging, but not

impossible. To overcome this problem another rock thickness calculation method has been developed in our group. We have to create a 3D Computer-Aided Design (CAD) model from the available data (laser scanning, technical drawing, or other sources). Automatic triangulation algorithms can generate good quality CAD surfaces or bodies if we have a sufficiently high resolution point cloud, but sometimes it has to be done in the hard way, making a CAD model from sketch manually. The obtained 3D model is then fed into a simulation which propagates the particle through matter (specifically, we use Geant4 [133]). An example of the comparison between the converted muon flux measurement and the expected rock thickness is shown in Fig. 4.5, where the expected rock volume is calculated from a 3D model. The measurement was performed under Royal Palace in the Buda Castle, and the 3D model of the building frame structure has been used to calculated the integrated rock length from the ground level. The "missing rock" of the measurement (the difference of the expected and the measured rock thickness) perfectly (below 0.5°precision) indicates the walls of the palace.

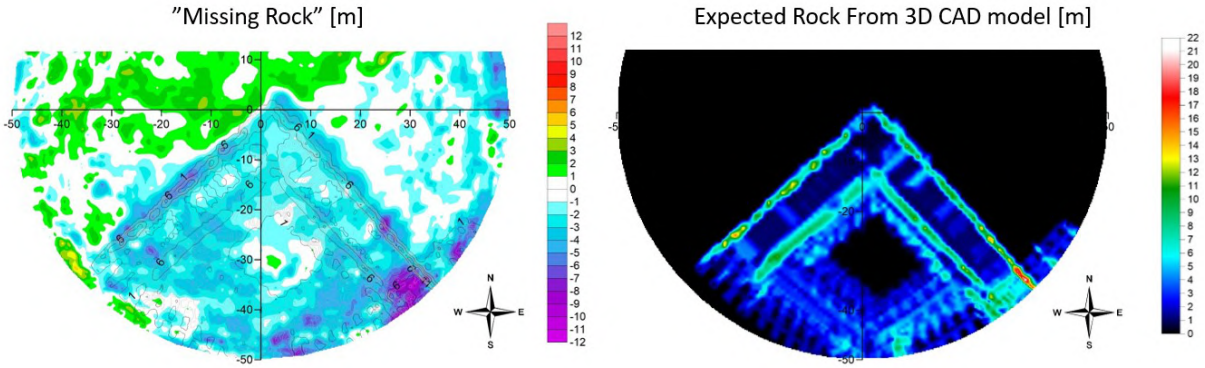

Figure 4.5: Left: the muographic data are shown in the "missing rock" colormap representation with geodesic angle coordinate system (also overlapping the contour lines of expected wall thicknesses). Right: the corresponding expected rock lengths by simulation (integrating from the ground level of the building). Images from G. Surányi.

For subtask (B), the inputs are the rock thickness, a density value, and a zenith angle, from which the algorithm calculates the direct problem of Eq. 4.2. This means that first the minimum energy is calculated from the density-length by Eq. 4.11, using the Lesparre parametrization Eq. 4.9. After that, Eq. 4.2 is solved by the preselected muon spectra (Guan, Eq. 4.3 or Reyna, Eq. 4.6). An extra value can also be added to the minimum energy for the compensation of the energy cut of the detector, since the scattering of low-energy particles is filtered out (the quantity of which must be determined by external calculation or simulation). The subtask (B) computation results in the expected muon flux if a homogeneous compact rock layer is assumed with the input average density. Continuing the calculation with Eq. 2.2, the expected numbers of muon counts can be obtained together with the statistical errors. This conversion is important for the muography survey planning to estimate the required duration of the measurement at the given significance level.

Subtask (C) is the actual muography measurement data processing. To obtain the measured density-length from the muon flux, the subtask (B) computation must be done in "reverse" mode. I solved this by creating a reference parameter table, calculating the direct problem in high resolution (in density-length and zenith angle dimensions as well) in the range of 0–5000 m.w.e. and zenith angles of 0–85°.

As a first step, the density-length value is estimated based on the lookup tables, then the algorithm derivatively iterates one or two steps by calculating the direct problem until the relative difference is under 1%. The statistical uncertainty is also propagated using the uncertainty calculation of the flux. The usual approximation of the expected variance is the number of muon counts ($\sigma_N^2 = N = \Phi(\varrho) \cdot A_{\text{eff}} \cdot \tau$), since it follows a Poisson distribution. Note, that the standard deviation of the flux is therefore $\sigma_\Phi = \sigma_N/(A_{\text{eff}} \cdot \tau)$. The deviation of the density-length is derived from a first-order Taylor expansion of the $\varrho(\Phi)$ function

$$\sigma_\varrho^2 = \left(\frac{\partial \varrho}{\partial \Phi}\right)^2 \cdot \frac{N}{(A_{\text{eff}}\tau)^2} \,. \tag{4.12}$$

Finally we are able to create an image from the muographic data. Gridding the view cone and plotting the results into an image has the same distortion issues as projecting a spherical sector onto a flat plane (like mapping the surface of the Earth). At a raw data level, we usually apply coordinates which are natural for the detector system: tangent slope of the angle bins (s_x, s_y, unit length divisions in X,Y axes).

A case example is shown in Fig. 4.6, where I processed a muographic data and the different processing stages are presented as a summary of the methodologies explained above. The data are from a one month measurement with the MTL-4 detector from the survey in the Buda Castle for civil engineering and archaeological purposes (see Sec. 5.2 for more details). The first step is to produce a map of integrated muon fluxes in each direction from the tracking data, as it shown in Fig. 4.6 left, where color scale indicates the flux values and X,Y axes represent the tangent slopes of each angle bin. In the next step, my software computes Eq. 4.2 inversely, thus providing an density-length map from the measured muon fluxes (Fig. 4.6 middle). The density-length map extracted from the measurement can already provide useful interpretation for relative or dynamic muography analyses.

For the estimation of the "missing rock" or the measured mean density in a given direction, we need to calculate the expected path lengths in the examined medium. This can be carried out either by CAD modeling and simulation (recommended in case of complex topography), or by integrating the line of sight from the detector under the surface (recommended in simple cases, using DTM data) with my algorithm. The ratio of the measured density-length and the expected rock length results in the measured mean density distribution obtained from the muographic measurement. If we have a reliable average density expectation in a region, we can derive the lengths of "missing rock" by dividing the measured density-length with this assumed density, and subtract it from the expected path length (Fig. 4.6 right). This way we get a map of probable rock length anomalies such as cavities or high-density bodies. The uncertainty calculation originates from the raw number of counts in one angle bin, and this is propagated throughout the calculation processes by Eq. 4.12 (note, that the systematic effects add up).

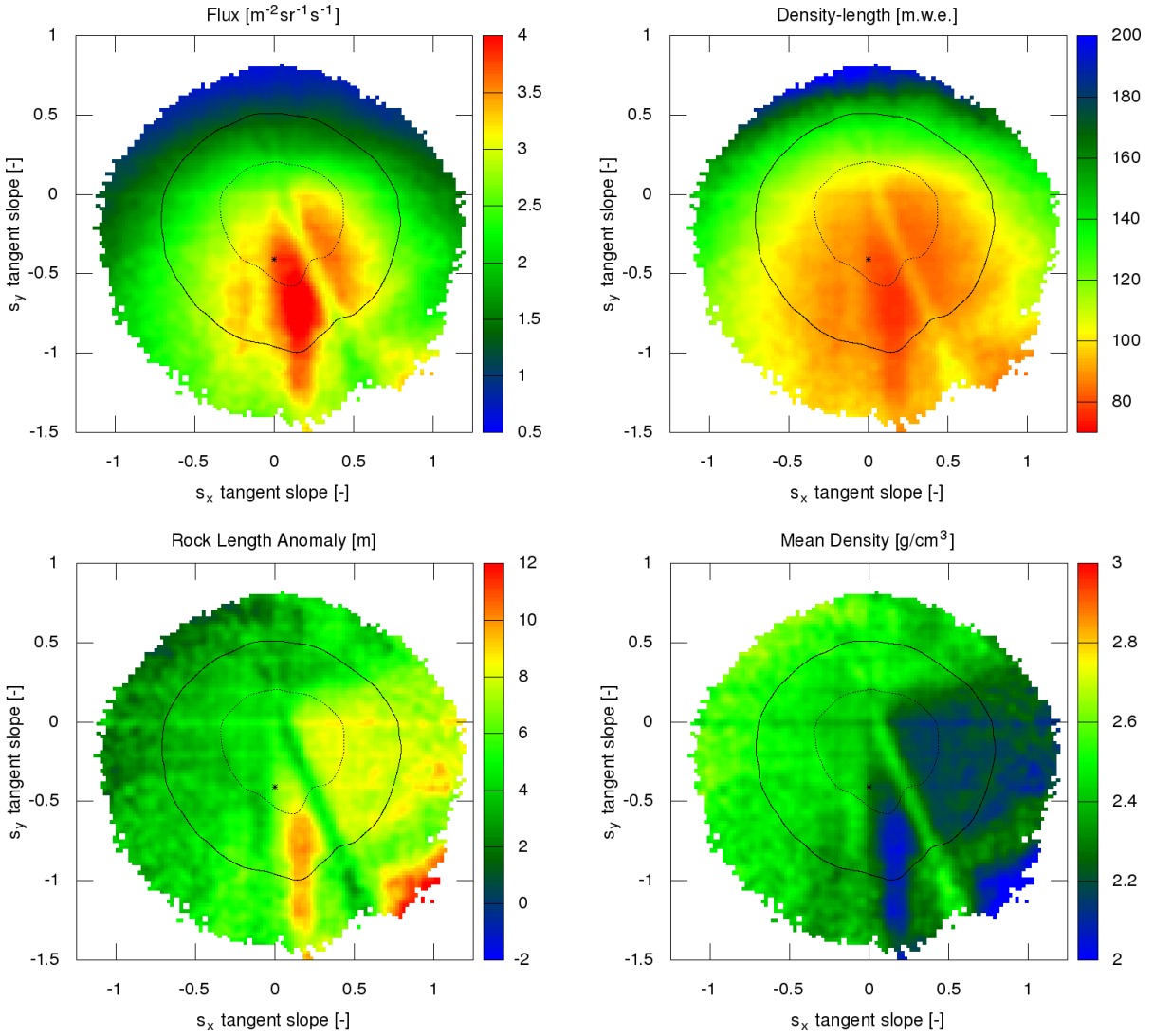

Figure 4.6: Example image series of the muographic data process, where the color coded data are represented in the tangent slopes of detector direction angles. Solid and dashed lines showing the boundaries of 5% and 3% uncertainties, respectively. Top Left: first, the muon flux is obtained from the raw detector data. Top Left: the muon flux must be converted to density-length for geological density analysis. Bottom Right: rock length anomalies can be interpreted as the "missing rock" from the measurement compared to the expected one. Bottom Left: mean density is the ratio of the density-length and rock length.

Of course, multiple other representational combinations can be created from these above mentioned muography data, depending on the questions we want to be answered. For example, we could plot the ratio of density-length and expected rock thickness to derive the measured average density angular distribution, the representation of the rock length anomaly in the dimension of statistical significance (ratio of missing rock and σ_ϱ), or cutting off the data in any representation below a given statistical significance in order to emphasize only the anomalies.

4.1.3 Systematic uncertainties

To a first approximation, the open-sky muon flux of high-energy muons in a given direction is constant day and night, throughout the year. Less than a few percent time dependent fluctuation of the integrated muon flux of high-energy muons (meaningful for muography, i.e., $E_\mu > 1$ GeV) could exist due to the following reasons:

- Geomagnetic effect: When the low energy primary cosmic rays propagate through the magnetosphere of the Earth, it acts as a cut-off rigidity (threshold) filter depending on the latitude. This is negligible at high geomagnetic latitudes (near the geomagnetic poles), but at low altitudes, this affects the low energy part (< 5 GeV) of the muon energy spectrum [5].

- Solar wind: The solar activity (wind velocity) modulates the low energy proton spectrum that interacts with the atmosphere. On the surface of the Earth, this results in a 1% variation in the differential muon flux at a momentum of 10 GeV (and 10% variation at 1 GeV) between minimum and maximum solar activity cycles [5].

- Atmospheric temperature: As mentioned in Sec. 2.1, the creation of muon after the high-energy collisions in the atmosphere strongly depends on the density of the air. This can be translated to an average T_{eff} temperature where the creation takes place. The dependence can be written as $\Delta\Phi = \alpha_T \Delta T_{\text{eff}}$, where $\Delta\Phi$ is the observed relative muon flux change in %, the temperature is in Kelvin, and the coefficient $\alpha_T = \left(1 + \frac{70}{E_{\text{min}}}\right)^{-1}$ depends on the minimum energy of the initial muon. This means that this effect is relevant at higher energies. For example, $\pm$(5–10) K seasonal effective temperature change causes $\pm$5–10% integrated flux change below 300 m of rock underground [5]. This effect has been also examined in [103] for muography applications.

- Atmospheric pressure: The barometric pressure (measured around the detector) affects the flux due to the atmospheric absorption of the muon. The quantity of the effect reported in the literature are in the order of 0.5% decrease per 1 mbar increase for energies around 10 GeV, and becomes insignificant above that [5].

Further time-independent systematic errors could arise in the flux determination due to:

- Altitude: The dependence of the muon flux on the detector distance above sea level (h [m]) is driven by the length between muon creation and observation point, since a longer path length gives room for absorption and decay. The differential muon flux increases with the altitude by $\varphi(E_\mu, \theta, h) = \exp(-h/h_0) \cdot \varphi(E_\mu, \theta, h = 0)$, where $h_0 = 4900 + 750 \cdot E_\mu$ is an empirical characteristic length and is valid above 10 GeV minimum energy and between 0 and 1000 m altitude [134]. This causes an 8% integrated flux increase in extreme cases (around 50 m.w.e. if the altitude is 1000 m instead of 0 m), and becomes less than 1% above 300 m.w.e. The correction for this effect is included in my Flux Converter software.

- Discrepancies in the different muon spectrum data and parametrizations: As I showed earlier, the discrepancies in Fig. 4.3 and Fig. 4.1 between two different flux calculation

methods which describe most accurately the muon spectra relevant for muography, can reach even 20% difference in the integrated flux in certain cases, not to mention other muon spectra and minimum energy calculation. For a simple muon spectra parametrization, there is currently no accurate method available but detailed Monte Carlo simulations are needed for the realistic estimations. My conversion algorithm calculates by both Reyna and Guan methods, and if the absolute value of the muon flux is to be calculated, then the systematic uncertainty of the parametrization can be estimated from the discrepancy.

- Detector energy cutoff: At some point of the tracking algorithm must decide if a muon trajectory was a straight line or it is only some noise or low energy particle scattered in the sensitive volume (in our case, we use a chi-square threshold as it was described in Sec. 4.1.1). This inherently means that there is an energy cutoff for the detection of the incoming muon spectra. I implemented in my software an effective energy cutoff (adjustable) parameter which is added to the minimum energy during the calculation, but this parameter must be calculated in advance (e.g., by detector simulation [11]), in any case the estimation of the energy cutoff is an additional systematic uncertainty for the muon flux calculation.

- Chemical composition of the imaged objects: As already mentioned for the minimum energy calculation at Eq. 4.9 the exact energy deposition depends on the material, and a so-called 'standard rock' is used for the Lesparre parametrization. However, it was shown that the integral of Eq. 2.1 Bethe formula to find the total "continuous slowing-down approximation" [4] can significantly differ from Geant4 simulations at 1 TeV muon energy for silicon dioxide [103, 135]. Furthermore, different paramterizations of the minimum energy function on density-length exist for different materials [136]. For example, Reichenbacher [137] showed that the minimum energy function of the rock composition in the Soudan iron mine in northern Minnesota, US ($\rho \approx 2.85$ g/cm^3, $Z = 12, A = 24$) significantly deviates from the standard rock. The latter parametrization is also implemented in my software as an optional minimum energy calculation method.

These effects generally mean a first order homogeneous base line shift for the muon flux map. They may result in a few percent uncertainty in the absolute value of the flux, but the relative value between different angle bins are not affected. However, the following issues may result in angle-dependent flux errors.

- Multiple scattering: The muons are deflected in the material of the object due to a series of Coulomb scatterings on the nuclei of the medium. The distribution of scattering angles after a small amount of medium follows a zero-centered Gaussian distribution with a root mean square approximated as

$$d\sigma_{\mathrm{MS}} \approx \frac{13.6\mathrm{MeV}}{E_\mu}\sqrt{\frac{L}{X_0}}\left[1 + 0.038 \ln \frac{L}{X_0}\right], \tag{4.13}$$

where E_μ is the energy of muons, and L/X_0 is the ratio of density-length of the medium and the radiation length [37]. The total scattering of the muon across the medium is obtained by the sum of small scatters along the path. As the muon loses its energy

through the medium, scattering angles are increasing. The total scattering in usual muography applications is mostly below 10 mrad, and is significant especially at low muon momenta (< 2 GeV) which can be suppressed with appropriate filtering (see Sec. 2.3.2 for details). The effect of multiple scattering is noticeable when the contour edge of a density anomaly (high gradient in the flux map) is about to be determined. For example, the shadow of walls in Fig. 4.5 areblurred by the scattering.

- Geodetic and geologic deficiencies: Although somewhat trivial it needs to be mentioned for the sake of complete picture that the DEM data, the detector position, and pointing direction angle measurement also include errors, which must be considered for uncertainty calculations but should be as precise as possible.

- Detector efficiencies: Last but not least, we should not forget about the tracking accuracy (for angular resolution) and efficiency (for flux determination) inherited from the detector system. The angular resolution measurements of our detectors are shown in Fig. 3.15 with the discussion of potential detectorphysical issues (segmentation inequalities, discretization errors, channel cross-talk, missing or noisy channels, etc.). The effective detector surface computation, and tracking efficiency are discussed in Sec. 4.1.1. The latter is continuously monitored during data collection, and these effects are included in Eq. 4.1.

4.2 Tomographic inversion for spatial density distribution reconstruction

Muography measurements used for tomography, involving the three-dimensional reconstruction of density distribution from two-dimensional muon flux maps resembling radiographs, present distinct challenges. The optimization of the detector's field of view and coverage becomes crucial, taking into account the reduction in muon flux at greater zenith angles and the available options for detector placement. The equation system of the inverse problem – from directional muon fluxes to 3D density map – is usually underdetermined (more density values are desired than available measurements) which can calculation instability due to the partial coverage and uncertainties. These problems can be solved by simplifications, linearizations, and geologically relevant Bayesian constraints. While the Bayesian principle can lead to parameter bias and artifacts, utilizing back-projection of measurement uncertainty weights can effectively remove blind spots in a specific measurement setup, and any artifacts can be assessed through point response analyses. Consequently, this approach allows for the mitigation of most parameters that contribute to instability.

In section 4.2.1, I cover some of the important issues in the absorption-based muography inversion which is transmission tomography in nature. In the following section Sec. 4.2.2, I present some strategies to obtain the spatial location of a density anomaly, in more details with the application of a linearized (density length based) Bayesian inversion method. After testing the procedure on simulated data, I processed an actual high-quality muography measurement data set with my flux calculation software from 7 positions in the Királylaki tunnel, Budapest (Sec. 4.2.3), which was used as an input for the inversion. The result

demonstrate the tomographic imaging of a complex karstic crack zone and provides details on the complicated internal structures of the rock layers above the tunnel. The existence of low-density zones in the imaged space was verified by samples from the core drills.

4.2.1 Summary of the muographic inverse problem

An inverse problem is the process of calculating from a set of observations the causal factors that produced them. For example, imaging the structure of human tissues with X-ray computed tomography (CT), source reconstruction in acoustics, calculating the density distribution of the Earth from gravitational field measurements, or unfolding distributions from particle interaction measurements. They are called inverse problems because the inputs are the effects and the aim is to calculate the causes.

The topic of inverse problem theory and methods for model parameter estimations, especially in geophysical applications, is well covered in the book from Tarantola [138]. The introduction of the basic mathematical concepts is also included there and not the subject of this dissertation. However, muography inversion – being a very young scientific field in geophysical applications (Sec. 2.2) – faces special challenges which are active part of recent R&D, and this is discussed in the followings.

A tomographic muon measurement is rather complex and requires not only high statistics of data, but systematic errors need to be well controlled from the multiple points of views. A simplified linear matrix equation, as a base to describe the muograph data inversion, is

$$\boldsymbol{\varrho} = \mathbf{F} \cdot \boldsymbol{\rho}, \tag{4.14}$$

where $\boldsymbol{\varrho}$ is the combined vector of directional density-length measurements, $\boldsymbol{\rho}$ is the combined vector of the searched densities in all the voxels of the domain space, and $\mathbf{F}$ is the matrix of mapping from the voxels of the imaged space to the directional measure bins (integral projection along the cone of solid angle). If put simply the inversion problem of muography is to find the inverse of matrix $\mathbf{F}$.

The linear inversion based on the least squares method was introduced for the muography application by Nishiyama et al. [139], adopting a Bayesian approach in order to incorporate *a priori* information, and the method has been successfully used for volcano imaging, in a joint inversion with gravity data [140].

Filtered back projection of muographic images was described by Nagahara and Miyamoto [141]. The filtered back projection algorithm is based on the Radon and Fourier transformations and commonly used in medical applications, such as X-ray CT. The adaptation of the method has been demonstrated in [142].

Muographic surveys may invoke other measurement techniques for a comparison or joint inversion, such as gravity [140, 143, 144, 145] or electric resistivity [146].

Muon tomography has been successfully applied earlier, for instance to identify underground density increase by an ore body [147] and decrease by cavities [148, 149, 150], and to image the internal structure of a volcanic cone [151] or nuclear reactor [152].

The most straightforward way to determine the spatial location of an anomaly is, however, to look at the data with the naked eye before turning to the mathematical formalisms of inversion. If an anomaly is identifiable from different viewpoints, the distance of the recognised feature can be estimated by the angles and the distance of the detector positions by

triangulation, similarly as our two eyes can sense the depth and distances. Similar consideration led to the assumption of the size and location of a previously unknown big void in the Khufu Pyramid (Egypt) [24], or the discovery of a corridor-shaped structure in the same pyramid [111]. Triangulation has been used to find new chambers in the hellenistic necropolis of Neapolis (Naples, Italy) [153].

The above mentioned tomographic methods were all based on the attenuation of the cosmic muons, but it is worth reminding the reader here that 3D imaging based on multiple scattering or the secondary radiation production of the cosmic muons also exist, as introduced in Sec. 2.2.

Now I briefly summarize my thoughts about the issues and challenges arising in absorption muography inversion which must be controlled or regularized in order to obtain usable reconstructed density data:

- Relatively low statistics (compared to e.g., medical imaging), which is heavily zenith angle dependent.
- Strictly limited detector positioning (constrained by the surface or accessible underground facilities) and inherently one-sided imaging, since the detector altitude always has to be lower than (or equal to) the examined object (muons do not arrive from below the detector horizon).
- "Dead zones" appear in the mapped space, because the cones of the full detector views do not overlap the entire examined object, but these zones which are observed only by one detector also affect the inversion. The problem is outlined in Fig. 4.7 left.
- The system of equations for inversion is usually underdetermined considering the above mentioned issues, and the angular binning of the radiographic imaging is under a trade-off relationship between size of the anomaly, density contrast, and exposure time. Therefore the spatial voxels outnumber the directional muon flux measurements.
- Discretization error occurs, since the projection cones widen with the distance from the detector. Therefore the voxels of the mapped space can never be perfectly assigned to unique projection cones (the covariance matrix is not entirely diagonal resulting in artifacts).
- The detector size is not negligible (Eq. 4.1) if the imaged feature is of similar magnitude in size and distance as the detector. The solid angle bins of directions are overlapping, causing a parallax error as it is outlined in Fig. 4.7 right. Note however that we can actually turn this to our advantage by applying a 'back-projection' algorithm [148], providing a method for object distance estimation from single detector position.
- There may be systematic uncertainties as reviewed in Sec. 4.1.3.

4.2.2 Inversion methodology developments for muography

The forward problem, that is, the muon flux estimation based on the expected rock thickness and assumed average density in a given direction, has been well covered previously in Sec. 4.1.

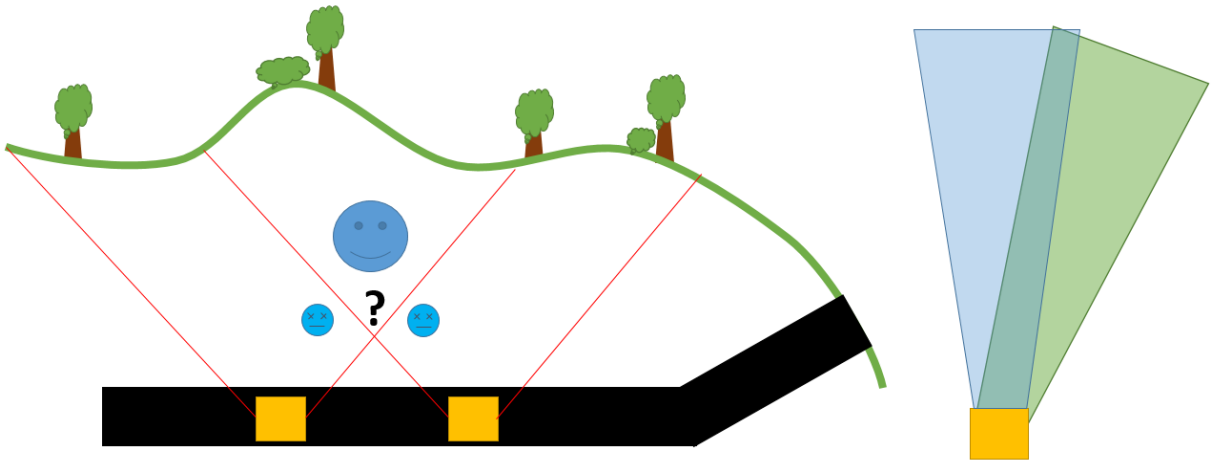

Figure 4.7: Left: A scheme for the "dead zone" issue in an underground muography example when the detector viewing cones do not overlap entirely in the examined region. Therefore, the location of the anomaly (e.g. a cavity) is underdetermined after the mapping to the detectors (yellow squares): is it one larger anomaly in the center (represented with larger dark blue circle) or two smaller in the dead zone (light blue circles). This problem can be overcome by adding extra views. Right: the parallax error is outlined when the size of the detector is not negligible and therefore the solid angle bins are overlapping.

In this section, I show my efforts to solve the inverse problem, particularly a triangulation method, a maximum-likelihood based iterative method, and a linear matrix inversion with Bayesian constraints. Furthermore, I present a certain (2+1D) slicing of the imaged domain in order to reduce the number of parameters by an independent sum of 2 dimensional problems, and the testing of the procedure on synthetic data is demonstrated. The application of the inversion methods for a case example in the Királylaki tunnel, Budapest, with the geological relevance and the validation is presented in the next section 4.2.3).

Triangulation method: Manual triangulation, that is, editing the cross-section of spacial directions of the same anomaly from different detector views, can be feasible in muography if the geometry is not too complex, since usually not too many detector view is available. In the previously cited examples (Khufu Pyramid, Neapolis), the editing of spatial lines happened along well-recognizable features of the anomaly (edges, corner points), and the intersection of these determines the location of the feature.

However, such well-defined shapes cannot be found in all cases. Therefore, my approach was slightly different for triangulation. I used a CAD software to create drawings of the detector positions. In each of these positions, I placed all the measurement direction vectors with the lengths of the "missing rock". An example is shown in Fig. 4.8 with three detector positions and three anomalies, where the data were taken from a real-case muography survey (Királylaki tunnel) for cavity search. The drawings indicate inclusion and exclusion zones in which the cavity can or cannot be, the center of the identified anomalies, and the most probable zone of anomalies (ellipses) based on the cross-section of "missing rock" lengths.

This method only works if each anomaly is uniquely identifiable, and no positive and negative "missing rocks" are overlapping.

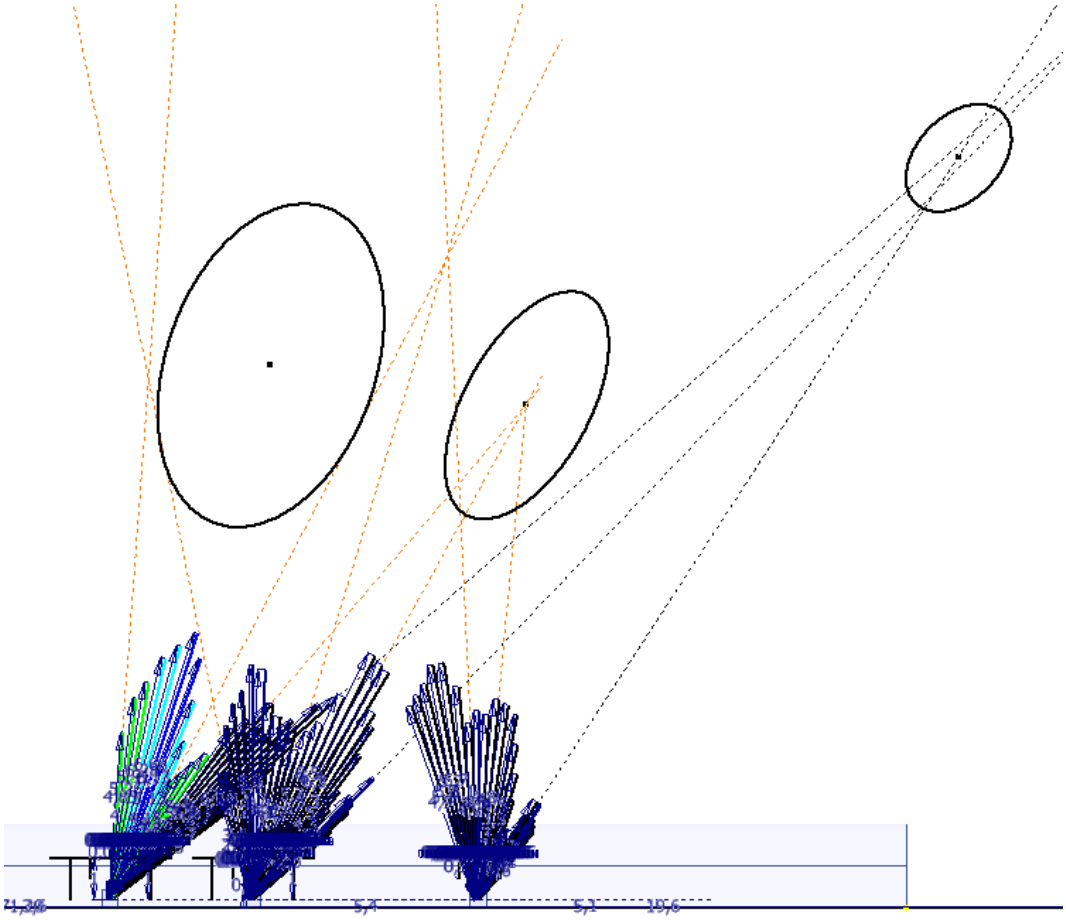

Figure 4.8: Triangulation method for anomaly distance estimation. "Missing rock" direction vectors drawn from the detector locations are guiding the editing of the most probable location of the anomalies.

Iterative method: I also experimented with the evaluation of Eq. 4.14 by a Maximum Likelihood (ML) based iterative reconstruction method called 'Expectation Maximization' (EM), known in medical imaging [154]. The method is originally developed for emission tomography (such as Positron Emission Tomography, PET) to reconstruct the isotope distributions in organs. A simple formula can describe the iteration steps [155] (the derivation of which can be found in the cited book chapter, or also described in the lecture notes of D. Légrády[3])

$$\rho_k^{n+1} = \rho_k^n \frac{1}{\sum_i^N \mathrm{F}_{ik}} \frac{\sum_i^N \varrho_i \mathrm{F}_{ik}}{\sum_m^M \mathrm{F}_{im} \rho_m^n}, \tag{4.15}$$

where i index denotes the measurements, the k index runs over the volume elements (voxels), and the m index denotes a section of the measurement line in a voxel. This calculation

[3] https://dtk.tankonyvtar.hu/xmlui/handle/123456789/7835 (Accessed: 2023-05-30)

process essentially means that the algorithm steps through the voxels and "corrects" the previous concentration estimate by re-integrating the line of response corresponding to the given voxels.

I used this algorithm for muography with the consideration that the concentration of isotopes can be translated to the concentration of density, but it is important to note that the ML-EM method is not valid for uncertainty calculation in this translation. So, in the future, the formula must be definitely upgraded for this purpose if is to be used. Nevertheless, I still experimented with this algorithm to test the muographic applicability and convergence of an iterative approach. For this purpose, I examined what kind of solutions I can get in a synthetic example of an underground muography case where the imaging is only one sided, so basically a Limited Angle Tomography (LAT, when only a limited number of two-dimensional projections are available). In Fig. 4.9, a cavity corresponding to 20% density anomaly is simulated in a homogeneous medium (the original distribution is shown in subfigure A), and in the following subfigures the reconstructed distributions are shown. In subfigure B, the inversion has been performed after a Radon transformation of the original distribution with a 180°rotational angle of detector around the object. Subfigure C is similar but the synthetic data is randomly scattered with a Gauss of 5% standard deviation, and the last figure (D) shows the most realistic case with 90°rotation angle and 5% uncertainty. The algorithm converged in around 50 steps in each case. The conclusions are that iterative methods may also be used in muography, since they can provide results even in underdetermined cases (artifacts can arise as subfigure D) shows), but I also had the important observation that the inversion (as all inversion) is very sensitive for the rotation angle in LAT cases, so the widest possible coverage of viewpoints is more advantageous than better statistics or more detector positions in smaller rotation angles.

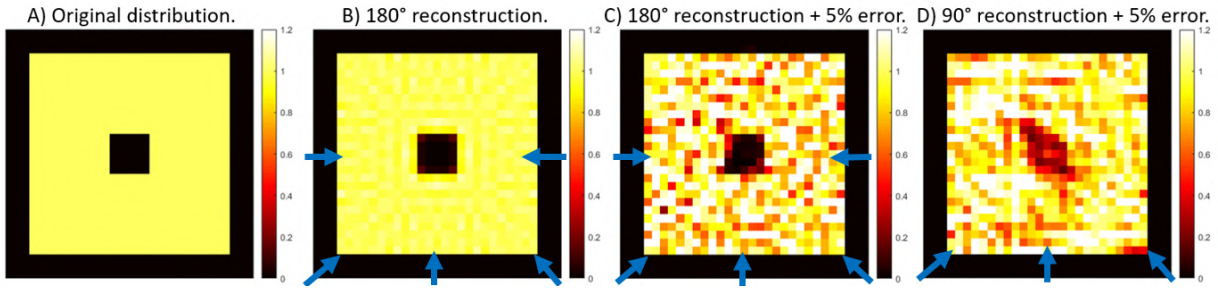

Figure 4.9: ML-EM iterative reconstruction algorithm tested using synthetic data with different detector direction vectors and data uncertainty.

Bayesian linear matrix inversion: In the following, I describe our adaptation of a linear inversion, based on weighted least squares fitting method and Bayesian approach for regularization [156]. The derivation of the mathematical formalism and the calculation of the inversion with this method is the credit of my colleague L. Balázs and is described in full detail in [156], but I summarize the basic points below.

The distance of the reconstruction from the measurement $\boldsymbol{\varrho_m}$, that is, the vector norm of $\Delta\boldsymbol{\varrho} = \boldsymbol{\varrho}_m - \mathbf{F}\boldsymbol{\rho}$ (derived from Eq. 4.14), is the basis for the inversion. Using density-length $\boldsymbol{\varrho}_m$ instead of muon flux Φ_m as measurement input data do not only result in an easier

interpretation by geoscientists, but linearizes the inversion problem since the density-length is an additive quantity.

The method of parameter fitting (density reconstruction) is determined by the error model associated with the imaging. It also determines the functional (quadratic form, Q) to be minimized during parameter fitting process. The error of the measured data can be considered as Poisson distribution, of which the maximum likelihood principle leads (approximately) to the weighted least squares fitting, minimizing the following functional

$$Q_\rho = (\boldsymbol{\varrho}_m - \mathbf{F}\boldsymbol{\rho})^T \mathbf{W}_\varrho (\boldsymbol{\varrho}_m - \mathbf{F}\boldsymbol{\rho}) \ . \tag{4.16}$$

The weight matrix elements (taking care of error propagation) are related to the transformation between flux and density length

$$W_{\varrho,i,i} = (A_{\text{eff}}\tau)^2 \left(\frac{\partial \Phi_{m,i}}{\partial \varrho_i} \right)^2 \frac{1}{N_{\text{det},i}} \ . \tag{4.17}$$

The density-length covariance matrix ($\mathbf{C}_\varrho$) is assumed to be diagonal, neglecting the small-scale data correlations (due to the transformation, multiple scattering, or parallax error). Expressing with the weight matrix

$$\mathbf{C}_\varrho = \sigma_\varrho^2 \mathbf{W}_\varrho^{-1} \ , \tag{4.18}$$

where σ_ϱ^2 is the calibration factor for the posterior $\mathbf{C}_\varrho$ which can be estimated from the post-fitting value of normalized Q_ϱ. The first step is to adapt the grid to the geometry of the domain to be mapped. Then a back-projection of the direction-dependent weight of the measurements are prepared

$$w_k = \sum_{i=1}^{N} F_{i,k} W_{\varrho,i,i} \ , \tag{4.19}$$

where the index i runs over the number of measurement bins, and index k runs over the number of volume elements (voxels).

This can be used to filter out blind spots in a given measurement configuration (kernel of Jacobian and grid elements, with negligible contribution). Thus, most parameters causing instability can be eliminated. In addition, changing the grid size locally can also improve the weight of a grid element. The model error from the discretization cannot be estimated during the fitting procedure. It is worth noting that the topographic error appears as a parameter error, a small near-surface density anomaly after the fit. The data can also be checked for the detectability of possible density anomalies before the fit. The feasibility conditions for muographic surveys have been examined in multiple papers (see, for example, [5] and [16]).

A typical muon tomography of cavity exploration sometimes requires even cubic meter resolution if possible. To make the underdetermination issues (thus parameter correlations) mathematically tractable, but also geologically relevant, Bayesian maximum *a posteriori* probability (MAP) principle was used to set up the fitting criteria. Thus, the functional Q_ϱ from the ML principle is complemented by another quadratic form Q_ρ for the parameters to be fitted [138]

$$Q^{(0)} = Q_\varrho^{(0)} + Q_\rho^{(0)} = (\boldsymbol{\varrho}_m - \mathbf{F}\boldsymbol{\rho})^T \mathbf{W}_\varrho (\boldsymbol{\varrho}_m - \mathbf{F}\boldsymbol{\rho}) + (\boldsymbol{\rho} - \boldsymbol{\rho}^{(0)})^T \mathbf{W}_\rho^{(0)} (\boldsymbol{\rho} - \boldsymbol{\rho}^{(0)}) \ , \tag{4.20}$$

where $\mathbf{W}_\rho^{(0)} = (\mathbf{C}_\rho^{(0)})^{-1}$ matrix is the inverse of the covariance matrix of the *a priori* distribution in Bayes' theorem. The above functional provides a dual metric for fitting the density vector. The first part is the criterion for the measurement space, the second part is the *a priori* requirement for the parameter space: $\boldsymbol{\rho}^{(0)}$ centered on the assumed parameter distribution. For the latter, a so-called half-Gaussian distribution is assumed (but other types can be considered, such as bimodal Gaussian, especially for cavity search). Under this assumption, the maximum of the distribution is the density of a well-defined solid rock. Deviation from this towards lower densities is due to screened cavities and fractured zones. The normal equations associated with parameter fitting

$$\partial_\rho Q^{(0)} = -\mathbf{F}^T \mathbf{W}_\varrho \boldsymbol{\varrho}_m + \mathbf{R}\boldsymbol{\rho} + \mathbf{W}_\rho^{(0)}(\boldsymbol{\rho} - \boldsymbol{\rho}^{(0)}) = \mathbf{0} \ , \tag{4.21}$$

where $\mathbf{R} = \mathbf{F}^T \mathbf{W}_\varrho \mathbf{F}$ notation has been applied to the symmetric quadratic matrix in the formula. Hence, the first order estimate of the density distribution is

$$\boldsymbol{\rho}^{(1)} = (\mathbf{R} + \mathbf{W}_\rho^{(0)})^{-1}(\mathbf{F}^T \mathbf{W}_\varrho \boldsymbol{\varrho}_m + \mathbf{W}_\rho^{(0)} \boldsymbol{\rho}^{(0)}) \ . \tag{4.22}$$

The covariance matrix can be derived from the expected values of the dyadic product of density distribution vector variation:

$$\mathbf{C}_\rho^{(1)} = \mathbb{E}\left(\delta\boldsymbol{\rho}^{(1)}(\delta\boldsymbol{\rho}^{(1)})^T\right) , \tag{4.23}$$

where the estimated density vector variation is a function of measured density-length variations and the prior density variation. The above formula combines the effect of these two sources of error in a weighted way. After some rearrangement we get

$$\mathbf{C}_\rho^{(1)} = \left(\mathbf{R} + \mathbf{W}_\rho^{(0)}\right)^{-1} . \tag{4.24}$$

Based on the known top surface (topography) or possible underground structures of the domain under investigation, the efficiency and focal area of a given measurement system can be investigated prior to the measurements, and the parameters of the measurement system can be optimized. A similar study may also be conducted to test the mathematical formulations above, in this section mainly with the aim to verify performance and understand the details of the output. In this example a predefined 3 m diameter cavity (zero density) is located in the measurement environment (homogeneous 2.5 g/cm^3 density) at a depth of 20 m and viewed by intuitively organized series of measurements 50 m below a flat surface.

A key question with the real measurement is finite statistics. Inversion with simulated statistical uncertainty after collecting 1 month data, assuming a 0.16 m^2 detector and 1°angular bins, are shown in the middle panel of Fig. 4.10. The qualitative picture remains the same, and at the cost of the details, the Bayesian approach suppresses oscillations in the inversion resulting from a standard maximum-likelihood fit.

4.2.3 A case study in the Királylaki tunnel

The REGARD group has a long history with underground muography, especially for cavity search in speleological applications with CCC detectors, as it was introduced in Sec. 3.1.

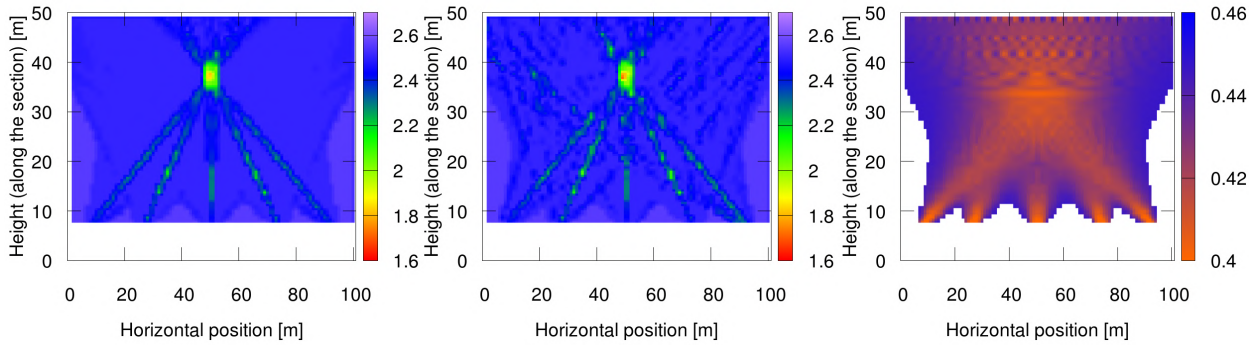

Figure 4.10: Density inversion results with a hypothetical void in a homogeneous rock of 2.5 g/cm^3 density: without uncertainty (left), with uncertainty if 1 month measurements assumed (middle), and the standard deviation of estimated densities (right) in g/cm^3. The scale of axes are not the same [156].

A research survey has also been conducted with first-generation detectors in the Királylaki tunnels in Budapest between 2015 and 2016. This muography survey indicated significant density anomalies, but the detector performance and the first attempts for inversion proved insufficient for the reliable spatial distribution determination. A new survey was prepared five years later with a novel high-resolution detector, named Mts-40 and shown in Fig. 4.11 at the location of the survey. I joined the implementation of new measurements where I studied the optimal detector positions based on the direct problem calculations, and I converted the measured muon flux data with my software for the inverse computations. Based on the reconstruction results, I estimated closest points and directions of the anomaly for exploratory drilling. The core drills validated the existence of low-density fracture zones in the rock [156].

Figure 4.11: Images of the tracking detectors consisting Close Cathode Chambers, installed in the Királylaki tunnel [156].

Survey configuration: Seven measurements were performed along the tunnel using the 0.16 m^2 Mts-40 detector with 1° angular bins. The detector were placed in the straight tunnel to study the density distribution of the overlying rocks for the purpose of cavity exploration.

The measurements were taken over a period of approximately one month per position to reach the proper variance and detection limit. Fig. 4.12 shows the topography of the examined region and the geometric configurations of the measurements, where the coordinates are on the basis of the National Hungarian Grid (EOV). Run numbers and associated arrows indicate each detector position and viewing direction, collecting data in a ∼90°cone in each field of view. These specific configurations have been chosen based on preliminary surveys to focus on the most significant and closest density anomalies.

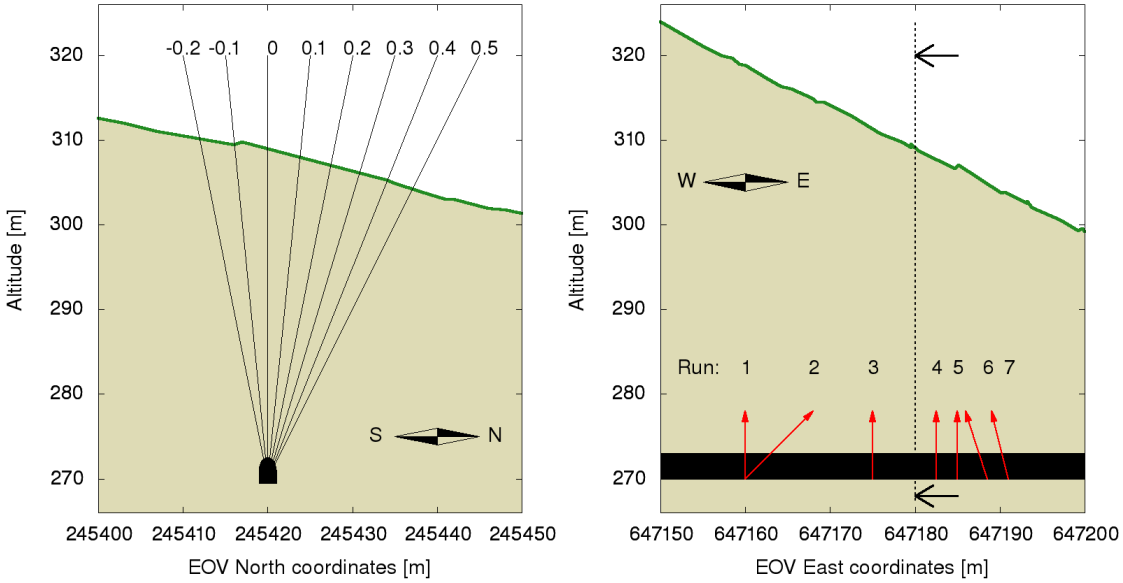

Figure 4.12: Topography and the geometric conditions of the measurements and inversion. Left: the section of the topography perpendicular to the tunnel. The slices (indicated from -0.2 to 0.5 by the tangent of their zenith angles) are the 2D planes in which the density reconstruction were conducted. Right: the section of the topography parallel to the tunnel. Red arrows show the detector positions and orientations (the dashed line indicates the section of the left figure) [156].

The detected density-length anomalies (difference between the measured density-length and that of a homogeneous rock) are presented in Fig. 4.13. The measured density lengths were the inputs for the inversion.

Inversion of a muon tomography measurement is an inherently three dimensional problem, but as the nomenclature suggests ('tomos' derived from Ancient Greek, meaning "slice, section"), some kind of slicing of the domain space is needed for imaging the data. In special cases, such as those having the measurement locations along a line, the parameter configuration can be reduced to an independent sum of 2 dimensional problems, or to the planes

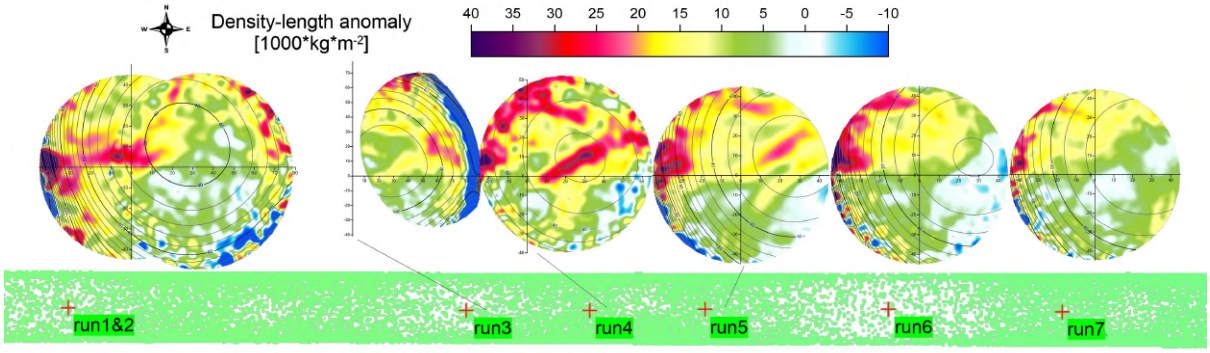

Figure 4.13: The detected density-length anomalies (deviations from a homogeneous density) are shown at the measurement positions in the tunnel, each plotted on a square grid of horizontal coordinate system. Contour lines represent the detector-to-surface rock thicknesses from the given point of view [156].

containing (intersecting) the measurement line. Motivated by the fact that the actual measurements presented here bear such property (carried out along a straight tunnel, as shown in Fig. 4.12), the reconstruction exploited this simplification. In practice, this means that the inversion is solved for each plane independently as a 2–dimensional problem, and the 3–dimensional density distribution is derived by the projection of the solutions to the voxel base of the examined space. The slicing that I applied for the evaluation of the inversion is shown in Fig. 4.12 left.

Density reconstruction: The results of the Bayesian inversion are shown in Fig. 4.14 for each slice with 1.5 m horizontal and 0.5 m vertical equidistant gridding. The coordinates are as follows: the origin on the vertical axis is at the level of the top of the tunnel, the horizontal origin is fixed at the end of the Királylaki tunnel (EOV East 647000). The southern slices (-0.2 and -0.1) do not contain significant anomalies. Accordingly, the resulting density distribution is essentially homogeneous in the middle part (in the focus area). The north slices show density anomalies reaching very close to the tunnel.

The inversion works efficiently in the focus area defined by high values of back-propagated weight (left panel of Fig. 4.15). However, this quantity falsely implies high sensitivity close to the detectors as well, since those voxels are taken into account by multiple measurement lines in this nearer region. The standard deviation of the density values (similar in all slices) are mapped in the right panel of Fig. 4.15.

The proper parameter fit in the measurement space is illustrated in Figure 4.16, where the data for a selected detector location are compared with the density lengths calculated from the fitted densities. The asymmetry of the curves can be explained by the topography. The quality of the fit is similarly excellent at all measurement points. The standard deviation is minimal in the direction of the focus range. With these measurements the detectability is also demonstrated: the anomaly compared to the theoretical measurements calculated with the reference rock density can be detected at the selected 95% confidence level.

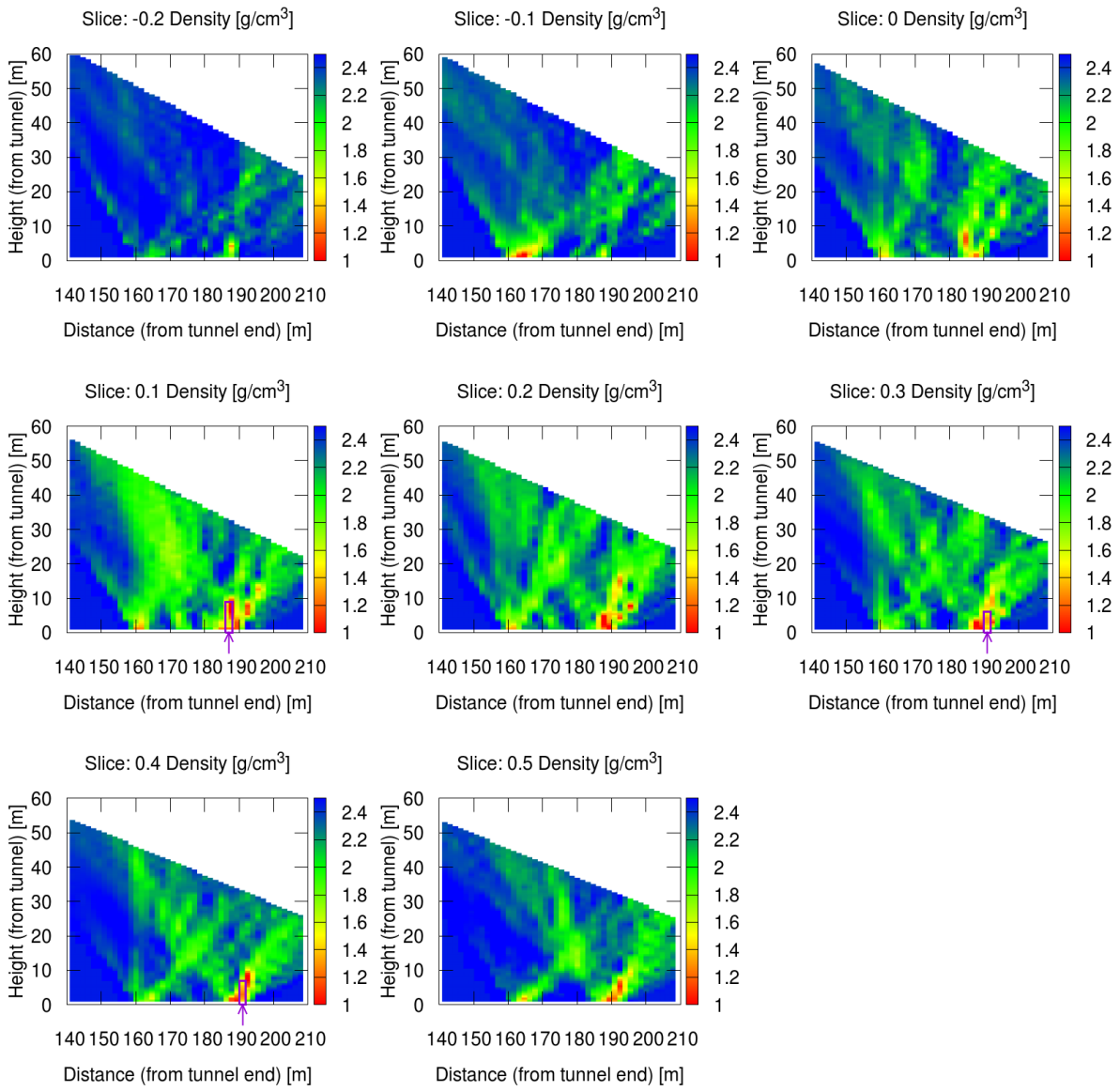

Figure 4.14: The result of the tomographic inversion (*a posteriori* density distributions) is shown in relevant slices (as Fig. 4.12). On the 0.1, 0.3, and 0.4 slices purple arrows show the validation drill locations [156].

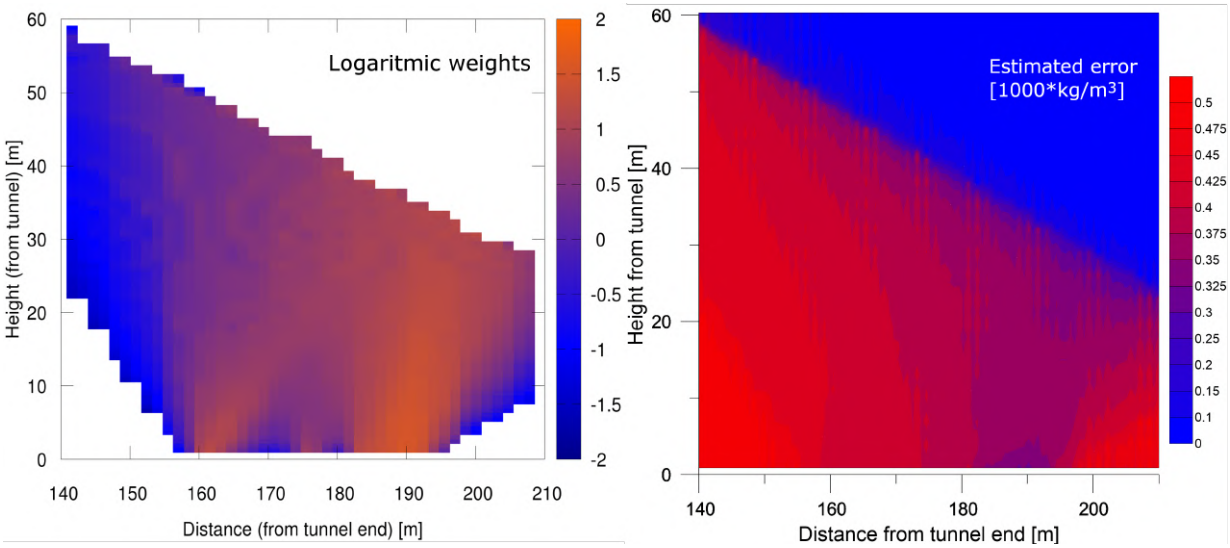

Figure 4.15: Maps of quantities describing the focus area and uncertainties in a chosen 2D slice (0.2 tangent slope). Left: the logarithmic weight factors (sensitivity map) which relates to the sum of number of counts from all the measurement lines crossing the given cell. Right: the estimated errors, propagated by the bias calculations [156].

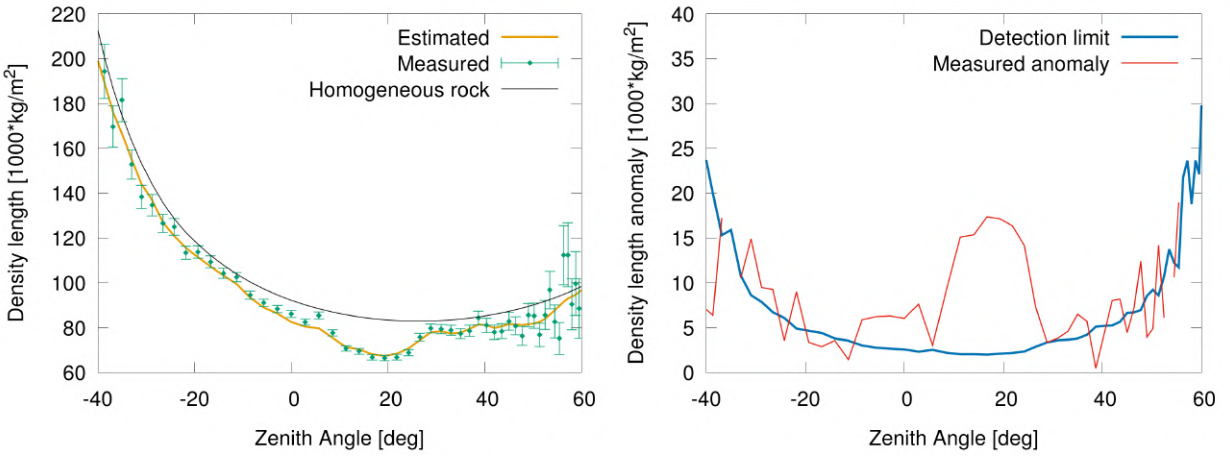

Figure 4.16: Left: The density lengths for a selected measurement (Run 5, -0.1 tangent slope), the result of fitting quality (estimated), and the assumed density lengths for homogeneous rock. Right: The density-length anomalies compared to the detection limit (95% confidence level) [156].

Validation using drill core samples: The measurements, both viewed as transmission images or tomographgic results, indicated large anomalies – decreased density regions – which are promising targets for a direct verification. Drilling seemed possible from the inside of the tunnel, with positions and directions aiming for anomalies close to the tunnel ceiling.

The length of the exploratory drill holes were limited to 10 m due to technical reasons. Altogether, three drill holes were drilled between the zenith angle of 3°and 22.5°with the length of 5.4 m, 5.8 m and 9.2 m, indicated in Fig. 4.14 with purple arrows in slices 0.1, 0.3, and 0.4, respectively. Although none of the drills found empty voids except the 20–50 cm space between the brick wall of the tunnel and the original rock body, the validation of the results were relevant. The low density zones detected by the measurements were large fissures filled up with altered dolomite powder, that has significantly lower density than the intact rock of cherty dolomite (∼1.8 g/cm^3 compared to 2.6-2.7 g/cm^3), see Fig. 4.17. The contact boundaries of the high and low-density zones (the walls of the fissure) were at the position previously predicted by the muon measurements by 20 cm accuracy. One of the drill holes went completely through one of the low-density zones reaching the farther wall of the fissure. Most of the dolomite powder has been washed away by the water of the diamond core driller, making it difficult to even continue the drilling operation. The extent of the low-density zone was the same as predicted within a meter precision. Generally, despite the differences between the predicted and the actual absolute densities measured on the drill cores, the overall geometrical structure of the fissure zones were detectable at very high precision by muon tomography.

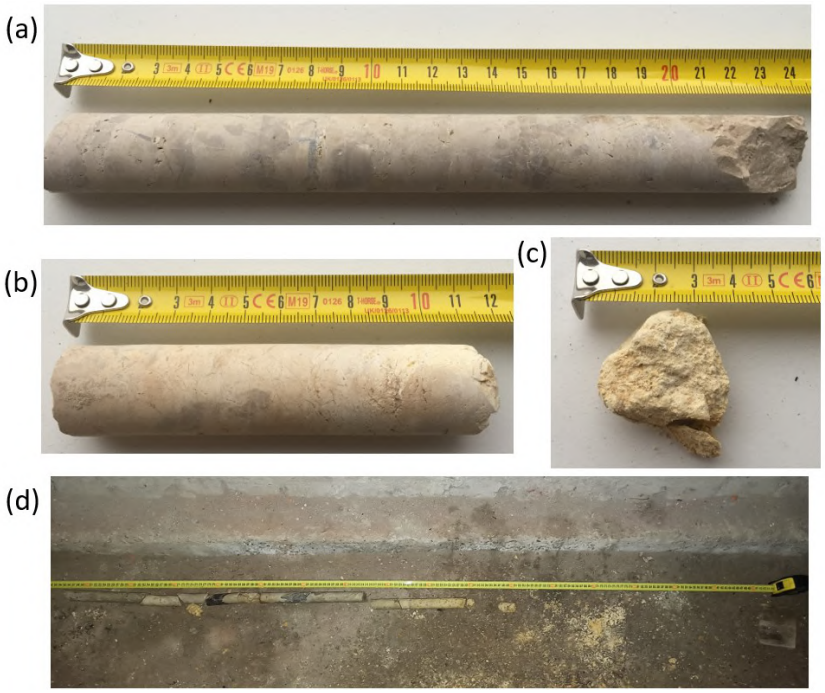

Figure 4.17: Drill cores with different densities: (a) intact cherty dolomite (2.6-2.7 g/cm^3); (b) slightly altered dolomite close to the walls of the fissures (2.4-2.5 g/cm^3); (c) altered dolomite powder (less than 1.8 g/cm^3); (d) the full extent of the last 2 m drill core from one of the drill holes. Dolomite powder only partially recovered [156].

Chapter 5

Outlook

In this chapter, I would like to provide insight into some of the ongoing or completed muography campaigns that I have been involved in (detector developments, installation, muon flux analysis), but limiting discussion only to those which are planned to be published.

5.1 Looking through a mountain: quantification of muographic imaging resolution

The objective of the measurement was to demonstrate the observation of one hill behind an other, in order to see the shadow of the farther hill through the coverage of hundreds of meters of rock. The contour of the shadow (high density-length gradient) can provide quantitative information about the imaging resolution of muography by the determination of the blurring systematic effects (e.g., multiple scattering) by comparing the measured results to expectations. This, along with practical considerations, required a very special location. First, the "target" must be a prominent (background) hill. This should be fully concealed behind an other foreground ridge, with a valley in between the two. The foreground structure should not be too thick (10–200 m in our case) in the target direction, and the target should be at a reasonably high elevation angle, in order to increase the muon flux signal. Accessibility and availability of power supply were also aspects, so was the availability of precision topography information. We were surprised to find such a location in the touristic area of Budapest, and so our target became the highest point within the boundaries of the city, the 'János Hill' (János-hegy, 528 m a.s.l.). The measurement location (250 m a.s.l.) was within a campsite at the feet of the spectacular 'Fairy Rock' (Tündér-szikla, 383 m a.s.l.).

The geometry of the location can also be understood from photographs taken 50 meters above the measurement location by a drone, shown in Fig. 5.1 left. Viewed from just above the measurement site, the prominent rock is visible in the foreground. A section of the topography DTM data, marked with green dashed line in the drone photo, is shown in Fig. 5.1 right. The contour lines of the relevant features are also labeled. The extra DEM data are also plotted around the Fairy Rock which has higher accuracy (DTM algorithm cut off the peak of Fairy Rock, processing it as a building).

The experimental setup was a MMOS type surface detector (Sec. 3.1.2) with 190 cm telescope length consisting of 8 layers of advanced MWPC chambers (a mix of type 80 and

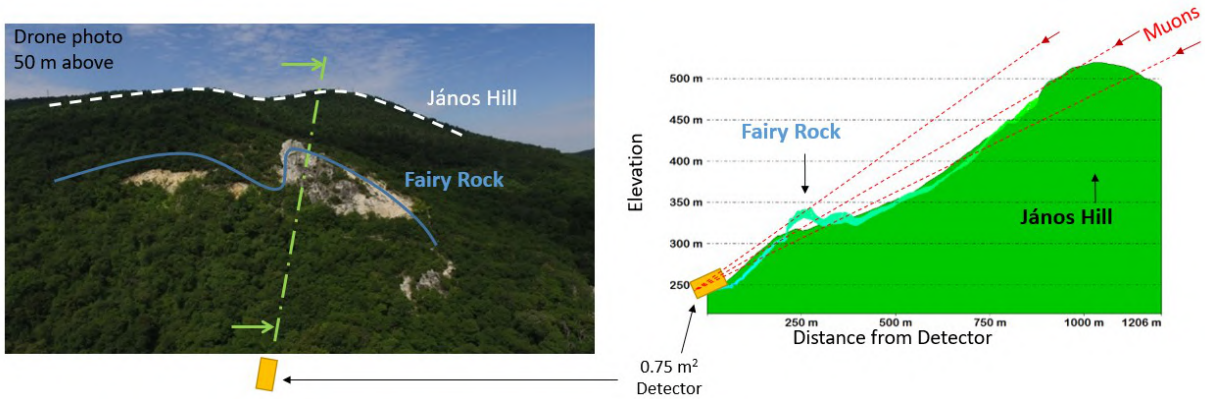

Figure 5.1: Topography of the Fairy Rock (Tündér-szikla, Budapest) measurement. The contour of János Hill is imaged through the Fairy Rock from the detector viewpoint.

120) and two lead walls (400 kg) for the background suppression. The configuration is shown in Fig. 5.2, along with a photograph of the actual system.

The tracking system had to be able to work in outdoor conditions for multiple months. Therefore some environmental protection was needed. For simplicity, a medium sized tent served the purpose, and despite its minor capability of reducing humidity and temperature variations, it proved to be sufficient. The installation time was less than one day in total.

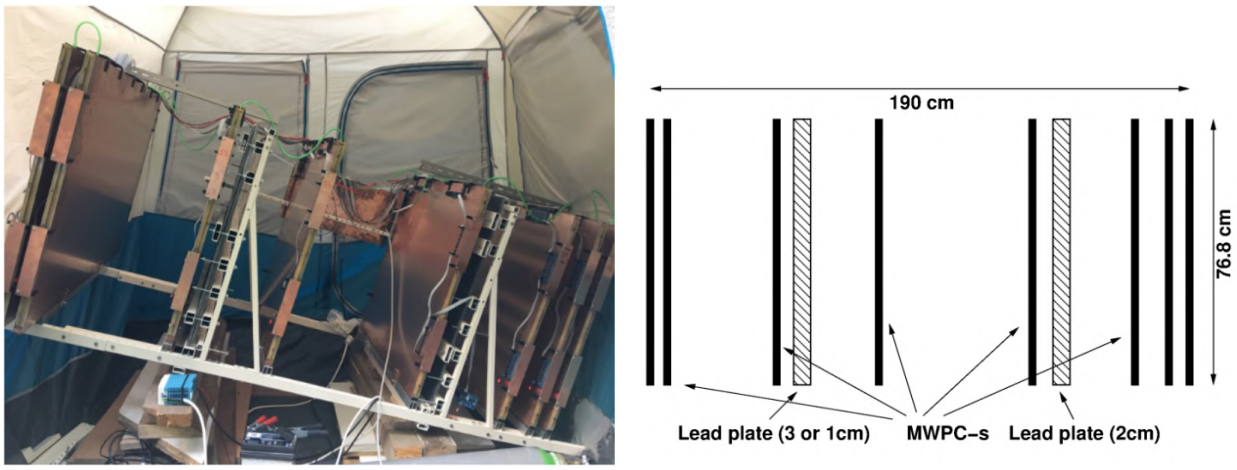

Figure 5.2: The surface detector system constructed for the measurement. On the right, the detector and absorber layers are outlined.

[37]. The total scattering of the muon across the medium is obtained by the sum of small scatters along the path. As the muon loses its energy through the medium, scattering angles are increase. The total scattering in usual muography applications is mostly below 10 mrad but may be significant at low muon momenta (< 2 GeV) which can be suppressed with appropriate filtering.

The muon flux data from a 2 month surface measurement is shown on the left in Fig. 5.3, and the expected muon flux on the right (calculated from DEM data). The contour of János Hill is behind 100–200 m rock, and below that line, the constant flux of 0.01 $m^{-2}sr^{-1}s^{-1}$ (> 500 m rock thickness) implies the background level. A remarkable similarity between the two figures can already be seen, but the quantitative evaluation and publication is in progress.

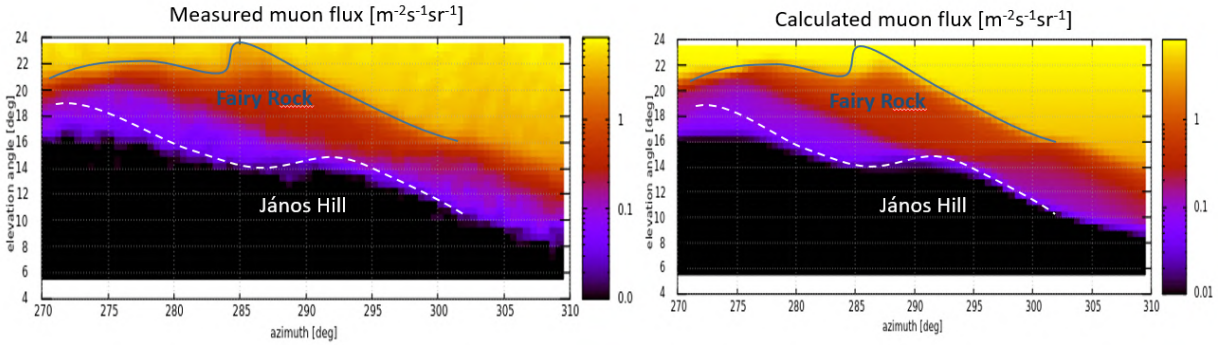

Figure 5.3: The measured muon flux of the Fairy Rock (left), which is well in line with the predicted muon flux (right). The angle bins describe the direction of measurements in the geodesic zenith and azimuth angles, and the color scale indicates the value of muon flux in $m^{-2}sr^{-1}s^{-1}$ [89].

5.2 Archaeology and civil engineering in the Buda Castle

Archaeological utilization of our detectors emerged within the Buda Castle (Hungary), aiming to uncover forgotten medieval tunnels. The imaging of a known tunnel has been demonstrated as Fig. 5.4 shows. After the beginning of the archaeological survey, further applications for civil engineering followed. The renovation works in the Castle require the detailed examination of building foundations. The existing tunnel system below the construction area provides an excellent opportunity for muographic exploration of dangerous cavities or debris zones. The study of missing rock from multiple positions led to the triangulation of a set of unknown underground density anomalies (Fig. 5.5). A detailed archaeological evaluation is expected in the future, but the founding of the examined construction has been confirmed to be stable. For the ongoing Buda Castle surveys, the MTL-1, MTL-2, MTL-4, and MTS-50 detectors have been used with a total of 20 months of data recorded in 31 positions until 2022 (in addition to the measurements of CCC-based detectors).

5.3 The Sicilian Job: archaeology and volcanology

A new collaboration between Wigner Research Centre for Physics, the University of Catania, and the University of Tokyo started in 2022. A MMOS system has been developed in

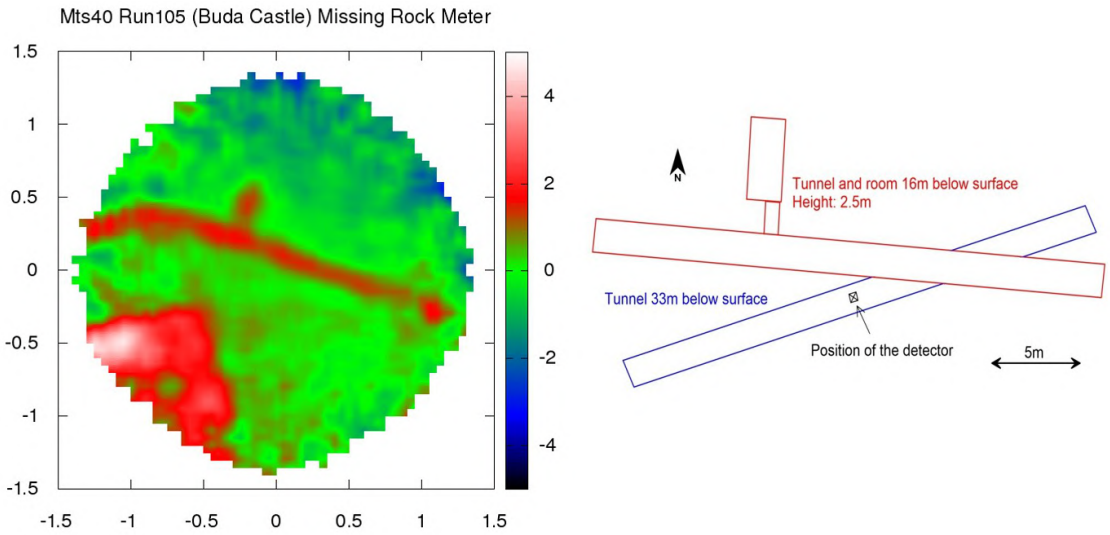

Figure 5.4: Imaging of a known tunnel and an underground room, which was accessible for viewing from below. The left panel shows the 'missing rock' muographic image, and the right panel shows the sketch of the tunnel structure and detector position [30].

combination of a scintillator-based MEV detector [13, 157]. The system was installed at the Castle of Mussomeli in Italy to look for archaeological cavities inside the castle's hill 5.6. Approximately one year data has been collected with excellent performance, and low gas flow (∼0.3 l/h) has been applied during the entire measurement. The system is planned to be installed on Mount Etna for volcanological purposes in the future.

5.4 Mining in Europe

Case studies were carried out for mining applications in Kemi, Finland. In collaboration with Muon Solutions Oy, the MTL-3 detector has successfully demonstrated the muographic imaging capabilities of density contrasts 270 m below the surface during a 6 month muography survey in two detector positions. A contact boundary layer between the lower density granite and the higher density magmatic intrusion and ore body has been located in 3D by the "stereographic" comparison of the two measurement. An even lower density region has been located. These were interpreted as a likely weathering crust.

For testing mining applications with the advanced MWPC technology, the ability of void detection has been proven in the visitor mine of St. Christoph, Germany, in collaboration with Muon Solutions Oy and Saxore Bergbau GmbH, within the framework of the Mine.The.Gap H-2020 project. For validation, a known vertical shaft has been imaged in 40 m depth from two points. In addition to the fact that the shaft was clearly identified and located, also the smaller density anomalies could be located on the surface, probably caused by tailings or waste rock deposits originated from the mine. Further ongoing muography surveys for mining applications (exploration and/or monitoring) are in progress, in the framework of the Horizon Europe projects of "AGEMERA" and "Mine.io".

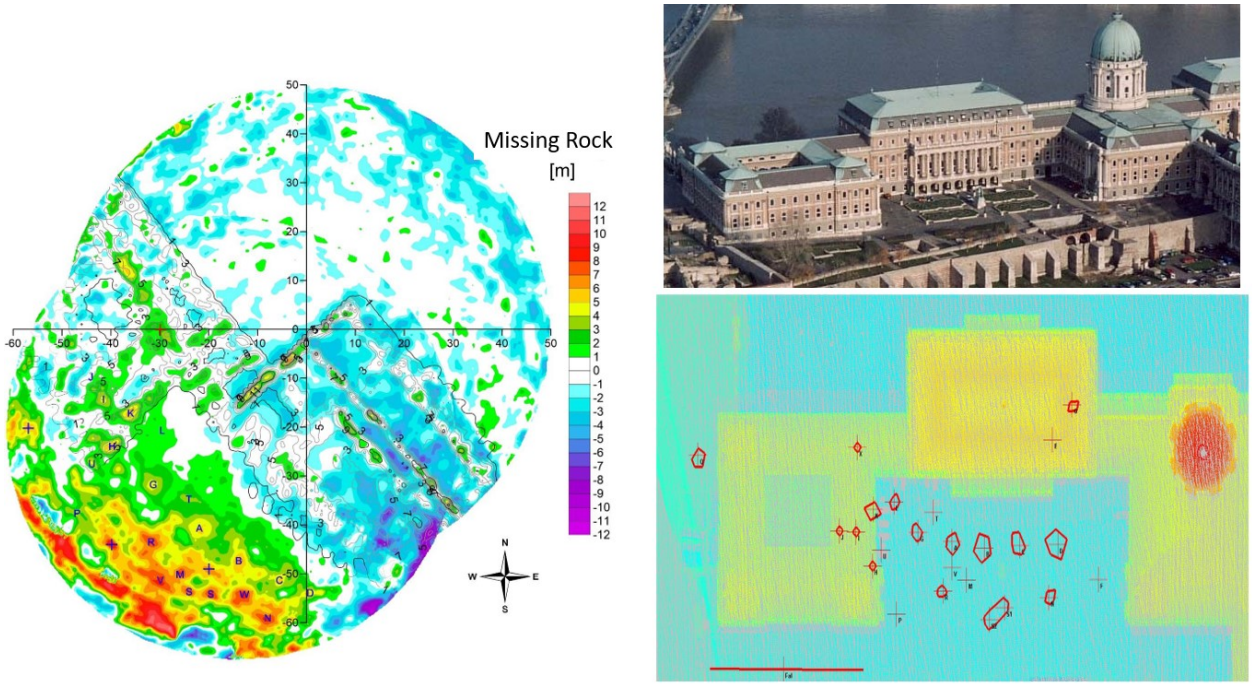

Figure 5.5: Preliminary results from the Buda Castle muography survey. Left: the missing rock muographic image from a viewpoint with the overlap of expected wall thicknesses. Bottom right: the spatially identified anomalies by triangulation (analysis images from G. Surányi, castle photo in the top right panel is from © Civertan Bt.; Wikipedia).

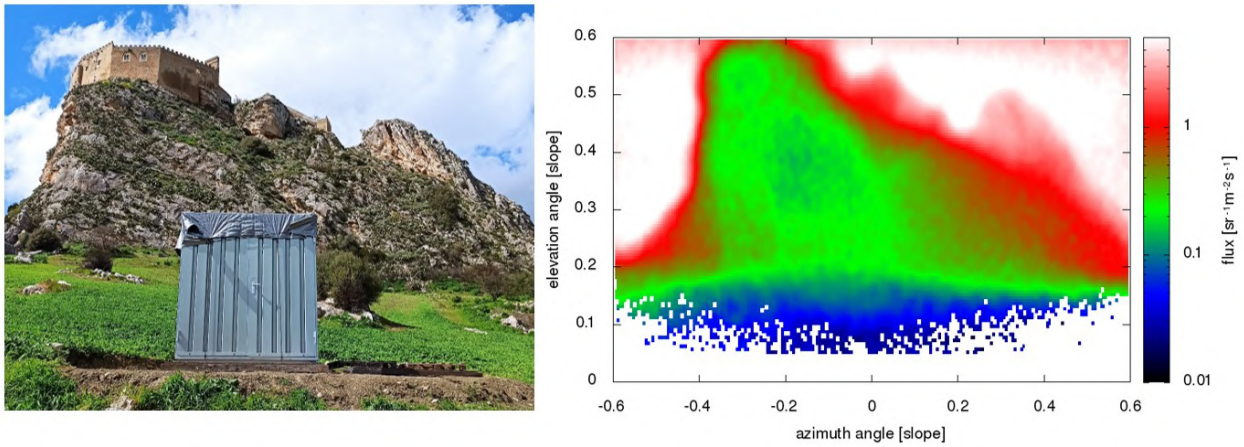

Figure 5.6: Photo and preliminary muon flux data from the Castle of Mussomeli, Italy.

Summary

In my PhD dissertation, I presented my development works related to gaseous detectors and data evaluation efforts for muography applications in the Innovative Gaseous Detector Development Research Group (REGARD) at the Wigner Research Centre for Physics.

At the beginning of my thesis, I summarized the literature which relates to muography and the detector technologies used for imaging with cosmic-ray induced muons. Sec. 2.1 elaborates on the creation of muons in the upper atmosphere due to high-energy cosmic particle collisions, and the physics allowing deep (up to kilometers) muon penetration into the crust of the Earth. Sec. 2.2 describes the muon flux and the imaging applications by attenuation, scattering, and secondary radiation measurement, showing a wide range of multidisciplinary utilization including archaeology, geosciences, or civil engineering. Sec. 2.3 summarized the detector families, sub-types, and the main design factors in case of surface or underground applications.

My detector development works were summarized in Ch. 3. At the beginning of Sec. 3.1 the reader was introduced to the innovative multi-wire detectors such as the CCC and the advanced MWPC detectors, developed by the REGARD group. Sec. 3.1.1 and 3.1.2 expands my first thesis statement, the development of components and supplementary instruments, construction methodology, chamber size and detector assembly variations, and the direct measurement of angular resolution. This essentially contributed to the applicability of the advanced MWPCs across a diverse set of outdoor situations, including long-term underground or surface measurements, fluctuating ambient conditions like temperature, pressure, and humidity, as well as challenges related to transportation.

The autonomy of the detector, and hence the low gas consumption to reduce maintenance, can be crucial in specific muography applications, since the remote data collection can take months. Thus if frequent maintenance required then the survey may be unfeasible in some cases (usually when infrastructure is not available). Therefore, I investigated (Sec. 3.1.3) how to operate the gaseous detectors with the lowest possible gas flow, keeping in mind the simplicity, which still ensures safe detector performance. My second thesis statement concludes that adding a buffer tube at the end of the gas line, which has a sufficiently large volume (necessary due to gas volume variation caused by temperature oscillation), and at the same time long enough to restrict axial diffusion, the advanced MWPC detector can be operated by even as low as 3 liters/day gas input flow.

The stability of the developed MWPC detectors against the above mentioned challenges has been demonstrated in Sec.3.1.4, and the application examples in Sec. 3.1.5, in particular the largest muography monitoring system at the Sakurajima volcano in Japan, shows the results of the developments.

Sec. 3.30 reviewed the cutting-edge technology of MPGD detectors, the application examples in muography, and my research for the quality assurance of GEM detectors. I demonstrated that the Leopard system can scan standard GEMs in 30 µm resolution which allows for the examination of local detectorphysical phenomena such as edge-effect or the effect of production defects (summarized in my third thesis statement). Therefore, the system can contribute to the optimization of the GEM technology.

Chapter 4 includes my fourth thesis statement, which describes muographic data evaluation processes, and methods for spatial density reconstruction from the muon flux data. I detailed the operation of the software I created for multiple tasks in Sec. 4.1.2. The software is able to generate rock lengths from DEM data in given directions, calculate the muon flux from an expected density-length, and compute the density-length from the measured muon flux. Possible systematic uncertainties in muography has been summarized in Sec. 4.1.3.

I described muon-tomographic inversion methods in Sec. 4.2, and our adaptation of a maximum likelihood inversion, based on the weighted least squares fitting method, on a discretized space with the combination of geologically relevant Bayesian constrains for the multi-view muographic measurements. The method includes uncertainty propagation, quantifications for the focus zone determination, and synthetic data test. The applicability for the 3D density estimation is demonstrated for the first time on a high resolution muography survey of a karstic underground crack zone at shallow depth (40–60 m), and validated by drill samples.

Acknowledgements

First, I would like to express my eternal gratitude to my supervisor Dr. Dezső Varga who always supported and guided me when it was needed. It is primarily thanks to him and the REGARD group that this PhD work was created. It is also indisputable to doubt all the help I got from Dr. Gergő Hamar regarding questions about electronics, software, or the Leopard developments.

I would also like to thank all my senior and junior colleagues with whom I worked during my PhD studies. Dr. László Balázs formulated the mathematical expressions for the Bayesian inversion. Ádám Gera supported me with mechanical simulations and designs. Dr. Gergely Surányi provided the geophysical measurement implementations. Dr. László Oláh help me to begin my muon flux conversion software development, and guided the Japan projects. Gábor Galgóczi participated in the Leopard developments. Péter Sántha conducted the modal analyzis of the Leopard. Csaba Marosi and László Tercsi implemented the Wire Dispenser. Dr. András Pál put his drone at my disposal for the Fairy Rock measurement. Last but not least I would like to thank all the members of the REGARD group for the joint work and the family atmosphere which significantly contributed to motivating and achieving the results presented in this PhD dissertation.

I am endlessly grateful for Baba, my family, friends, and teachers, without whom this endeavor would not have been possible.

The PhD studies were hosted by the Wigner RCP, and the Budapest University of Technology and Economics NTI, for which I am grateful. The INFN Trieste group (Italy) provided the deuterium lamp, Burken Kft. provided DEM data, and the Ave Natura Camping and the city of Mussomeli (Italy) hosted measurements for which I am also grateful. I would also like to thank the fruitful collaboration with the University of Tokyo ERI (Japan), the Muon Solutions Oy (Finland), and the University of Catania (Italy).

Financial support was provided from the H2020 project AIDA-2020 GA no. 654168, the "Lendület" LP2013-60 Programme of the Hungarian Academy of Sciences, the Hungarian state-funded scholarship of the BME doctoral school, the Joint Usage Research Project (JURP) of the University of Tokyo, ERI, under project ID 2020-H-05, the "INTENSE" H2020 MSCA RISE project under GA No. 822185, the Horizon Europe project AGEMERA (Grant No. 101058178), the "Mine.io" HEU project under GA No. 101091885, the Hungarian NKFIH research grant under ID OTKA-FK-135349 and TKP 2021-NKTA-10, NKFIH TÉT-2020-00224 Hungarian-Italian fund (2019, 2021), the ELKH-KT-SA-88/2021 grant.

Thesis Statements

1. MWPC detector design and construction for muography purposes

I participated in the development of the first advanced MWPC prototypes [87]. Based on this, I developed underground detector systems, which meet the conditions of long-term autonomous muographic data collection (portability, viewing alignment, dust and water droplet protection). I participated in the geophysical applications of these detectors, and I developed a method for the direct determination of the angular resolution of a detector module [30].

With field applications, I showed that large-surface MWPC-based detectors can be produced with the 3D printed elements and designed construction processes for producing detectors that can perform stable operation in outdoor conditions for long-term remote field surveys. The detectors are able to withstand large natural daily temperature fluctuations (Δ20 °C) and rapid temperature changes, high absolute temperature (40 °C) and high humidity (90% RH), as well as significant mechanical stresses occurring during transportation [98, 68, 89]. The developments significantly contributed to the application of the advanced MWPC detector chambers in the muographic observatory of the Sakurajima volcano in Japan [102, 92].

2. Low gas consumption for MWPC detectors

I showed that gas consumption can be minimized (even below 3 l/day) in the field application of MWPC-based detectors with an open gas system if a buffer tube is attached at the end of the gas line with a non-outgassing material, a volume corresponding to the air backflow resulting from daily temperature fluctuations, and a length to restrict air diffusion [98]. Diffusion can be further reduced with chokes installed in the buffer tube [99].

3. High resolution UV scan of micro-pattern detectors

I showed that with the Leopard detector scanner that the gain-homogeneity of GEM (Gas Electron Multiplier) detectors can be examined with a resolution of down to 30 µm and that the local detector physical properties can also be measured (e.g., edge-effect, effect of production defects) [6, 10, 21-23]. I have demonstrated that Leopard is capable of industrial quality control of large-scale GEMs. I presented the possibilities and limits of using micro-pattern detectors in muography [124].

4. Muographic data processing and density reconstruction

I investigated the conversion methods between muon flux and density-length. These are necessary for the evaluation of muographic data. Furthermore, I developed a software for the application of these calculations. I took part in the muography survey for cavity research in the Királylaki Reservoir in the Buda Mountains, and by processing high-resolution and multi-viewpoint data, I showed that the spatial location of density anomalies can be determined. Based on my preliminary calculations, I planned drilling points for validation, and the drilling validated the location of low-density crack zones underground. Based on the muographic data, I tested the determination of the spatial density distribution using a maximum likelihood-based tomographic inversion method and showed that the 3D muographic density inversion can be performed after appropriate linearizations in 2+1 dimensions in the case of linear measurement positions, i.e., instead of spatial meshing, it is sufficient to perform a two-dimensional inversion in the planes intersecting the lines of the measurement points for more stable convergence [156].

Bibliography

[1] V.F. Hess. Über beobachtungen der durchdringenden strahlung bei sieben freiballonfahrten. *Physikalische Zeitschrift*, **13**:1084–1091, 1912. doi: 10.48550/arXiv.1808.02927.

[2] C. D. Anderson and S. H. Neddermeyer. Cloud chamber observations of cosmic rays at 4300 meters elevation and near sea-level. *Phys. Rev.*, **50**:263, 1936. doi: 10.1103/PhysRev.50.263.

[3] L. Bonechi et al. Atmospheric muons as an imaging tool. *Rev. Phys.*, **5**:100038, 2020. doi: 10.1016/j.revip.2020.100038.

[4] M. Tanabashi et al. (Particle Data Group). Review of particle physics. *Phys. Rev. D*, **98**:030001, 2018. doi: 10.1103/PhysRevD.98.030001.

[5] N. Lesparre et al. Geophysical muon imaging: feasibility and limits. *Geophys. J. Int.*, **183**:1348–1361, 2010. doi: 10.1111/j.1365-246X.2010.04790.x.

[6] H. K. M. Tanaka et al. Cosmic-ray muon imaging of magma in a conduit: Degassing process of Satsuma-Iwojima Volcano, Japan. *Geophys. Res. Lett.*, **36**:1, 2009. doi: 10.1029/2008GL036451.

[7] L. W. Alvarez et al. Search for Hidden Chambers in the Pyramid. *Science*, **167**:832, 1970. doi: 10.1126/science.167.3919.832.

[8] E. P. George. Cosmic rays measure overburden of tunnel. *Commonw. Eng.*, **43**:455–457, 1955.

[9] P. Király. (Hungarian) Kozmikus sugárzás vizsgálata 40 méter vízekvivalens mélységben. *Szakdolgozat*, (ELTE TTK Fizika), 1963.

[10] H. K. M. Tanaka and L. Oláh. Overview of muographers. *Philos. Trans. R. Soc. A*, **377**:20180143, 2018. doi: 10.1098/rsta.2018.0143.

[11] L. Oláh et al. Plug formation imaged beneath the active craters of Sakurajima Volcano with muography. *Geophys. Res. Lett.*, **46**:17–18, 2019. doi: 10.1029/2019GL084784.

[12] K. Jourde et al. Muon dynamic radiography of density changes induced by hydrothermal activity at the La Soufrière of Guadeloupe volcano. *Sci. Rep.*, **6**:33406, 2016. doi: 10.1038/srep33406.

[13] D. Lo Presti et al. Muographic monitoring of the volcano-tectonic evolution of Mount Etna. *Sci. Rep.*, **10**:11351, 2020. doi: 10.1038/s41598-020-68435-y.

[14] R. D'Alessandro et al. Volcanoes in Italy and the role of muon radiography. *Philos. Trans. R. Soc. A*, **377**:20180050, 2018. doi: 10.1098/rsta.2018.0050.

[15] F. Ambrosino et al. Joint measurement of the atmospheric muon flux through the Puy de Dôme volcano with plastic scintillators and Resistive Plate Chambers detectors. *J. Geophys. Res. Solid Earth*, **120**:7290–7307, 2015. doi: 10.1002/2015JB011969.

[16] G. Leone et al. Muography as a new complementary tool in monitoring volcanic hazard: implications for early warning systems. *Proc. R. Soc. A.*, **477**:20210320, 2021. doi: 10.1098/rspa.2021.0320.

[17] J. Peña-Rodríguez et al. Design and construction of MuTe: a hybrid Muon Telescope to study Colombian volcanoes. *J. Instrum.*, **15**:P09006, 2020. doi: 10.1088/1748-0221/15/09/P09006.

[18] V. Tioukov et al. First muography of Stromboli volcano. *Sci. Rep.*, **9**:6695, 2019. doi: 10.1038/s41598-019-43131-8.

[19] Y.P. Cheng et al. Imaging internal density structure of the Laoheishan volcanic cone with cosmic ray muon radiography. *Nucl. Sci. Tech.*, **33**:88, 2022. doi: 10.1007/s41365-022-01072-4.

[20] D. Schouten and P. Ledru. Muon Tomography Applied to a Dense Uranium Deposit at the McArthur River Mine. *J. Geophys. Res. Solid Earth*, **123**:8637–8652, 2018. doi: 10.1029/2018JB015626.

[21] P. Teixeira et al. Muography for underground geological surveys: Ongoing application at the Lousal Mine (Iberian Pyrite Belt, Portugal). *Journal for Advanced Instrumentation in Science*, **2022**:Apr., 2022. doi: 10.31526/jais.2022.287.

[22] G. Baccani et al. Muon radiography of ancient mines: The San Silvestro Archaeo-Mining Park (Campiglia Marittima, Tuscany). *Universe*, **2019**:5, 34, 2019. doi: 10.3390/universe5010034.

[23] Z.X. Zhang et al. Muography and its potential applications to mining and rock engineering. *Rock Mech. Rock Eng.*, **53**:4893–4907, 2020. doi: 10.1007/s00603-020-02199-9.

[24] K. Morishima et al. Discovery of a big void in Khufu's Pyramid by observation of cosmic-ray muons. *Nature*, **552**:386–390, 2017. doi: 10.1038/nature24647.

[25] H.K.M. Tanaka et al. Muography as a new tool to study the historic earthquakes recorded in ancient burial mounds. *Geosci. Instrum. Method. Data Syst.*, **9**:357–364, 2020. doi: 10.5194/gi-9-357-2020.

[26] L. F. Thompson et al. Muon tomography for railway tunnel imaging. *Phys. Rev. Research*, **2**:023017, 2020. doi: 10.1103/PhysRevResearch.2.023017.

[27] G. Saracino et al. Applications of muon absorption radiography to the fields of archaeology and civil engineering. *Philos. Trans. R. Soc. A*, **377**:20180057, 2020. doi: 10.1098/rsta.2018.0050.

[28] H. Fujii et al. Investigation of the Unit-1 nuclear reactor of Fukushima Daiichi by cosmic muon radiography. *Prog. Theor. Exp. Phys.*, **2020**:4, 043C02, 2020. doi: 10.1093/ptep/ptaa027.

[29] L. Oláh et al. CCC-based muon telescope for examination of natural caves. *Geosci. Instrum. Method. Data Syst.*, **1**:229–234, 2012. doi: 10.5194/gi-1-229-2012.

[30] G. Hamar et al. Underground muography with portable gaseous detectors. *J. Phys.: Conf. Ser.*, **2374**:012186, 2022. doi: 10.1088/1742-6596/2374/1/012186.

[31] R. Nishiyama et al. Bedrock sculpting under an active alpine glacier revealed from cosmic-ray muon radiography. *Sci. Rep.*, **9**:6970, 2019. doi: 10.1038/s41598-019-43527-6.

[32] I. Lázaro Roche et al. *Muography: Exploring Earth's Subsurface with Elementary Particles*. Wiley AGU Books, 2022. doi: 10.1002/9781119722748.ch10.

[33] H.K.M. Tanaka et al. Periodic sea-level oscillation in Tokyo Bay detected with the Tokyo-Bay seafloor hyper-kilometric submarine deep detector (TS-HKMSDD). *Sci. Rep.*, **12**:6097, 2022. doi: 10.1038/s41598-022-10078-2.

[34] H.K.M. Tanaka. Muography for a dense tide monitoring network. *Sci. Rep.*, **12**:6725, 2022. doi: 10.1038/s41598-022-10373-y.

[35] H.K.M. Tanaka et al. Atmospheric muography for imaging and monitoring tropic cyclones. *Sci. Rep.*, **12**:16710, 2022. doi: 10.1038/s41598-022-20039-4.

[36] A. Chilingarian et al. Muon tomography of charged structures in the atmospheric electric field. *Geophys. Res. Lett.*, **48**:e2021GL094594, 2021. doi: 10.1029/2021GL094594.

[37] L. Olah et al. Investigation of the limits of high-definition muography for observation of Mt Sakurajima. *Phil. Trans. R. Soc. A.*, **377**:20180135, 2019. doi: 10.1098/rsta.2018.0135.

[38] L. Oláh et al. Development of machine learning assisted spectra analyzer for the NEWCUT muon spectrometer. *J.Adv.Instr.Sci.*, **2022**:264, 2022. doi: 10.31526/jais.2022.264.

[39] S. Botond. (Hungarian) Kozmikus müonok szóródásán alapuló képalkotás vizsgálata. *Országos Tudományos Diákköri Dolgozat*, (ELTE TTK Fizika MSc), 2022.

[40] K.N. Borozdin et al. Radiographic imaging with cosmic-ray muons. *Nature*, **422**:277, 2003. doi: 10.1038/422277a.

[41] E. Niederleithinger et al. Muon tomography of the interior of a reinforced concrete block: First experimental proof of concept. *J. Nondestruct. Eval.*, **40**:65, 2021. doi: 10.1007/s10921-021-00797-3.

[42] P. Checchia. Review of possible applications of cosmic muon tomography. *J. Instrum.*, **11**:C12072, 2016. doi: 10.1088/1748-0221/11/12/C12072.

[43] I. Bikit et al. Novel approach to imaging by cosmic-ray muons. *EPL*, **113**:58001, 2016. doi: 10.1209/0295-5075/113/58001.

[44] G. Galgóczi et al. Imaging by muons and their induced secondary particles—a novel technique. *J. Instrum.*, **15**:C06014, 2020. doi: 10.1088/1748-0221/15/06/C06014.

[45] S.Y. Luo et al. Hybrid model for muon tomography and quantitative analysis of image quality. *Nucl. Sci. Tech.*, **33**:81, 2022. doi: 10.1007/s41365-022-01070-6.

[46] P. Prada et al. Analysis of secondary particles as a compliment to muon scattering measurements. *Instruments*, **6**:66, 2022. doi: 10.3390/instruments6040066.

[47] G. Bonomi et al. Applications of cosmic-ray muons. *Prog. Part. Nucl. Phys.*, **112**: 103768, 2020. doi: 10.1016/j.ppnp.2020.103768.

[48] A. Lechmann et al. Muon tomography in geoscientific research – A guide to best practice. *Earth-Sci. Rev.*, **222**:103842, 2021. doi: 10.1016/j.earscirev.2021.103842.

[49] L. Oláh et al. *Muography: Exploring Earth's Subsurface with Elementary Particles*. Wiley AGU Books, 2022. doi: 10.1002/9781119722748.

[50] G. Hamar. Innovative gaseous particle detector R&D. *Wigner 111 Scientific Symposium*, 2013.

[51] F. Sauli. *Principles of operation of multiwire proportional and drift chambers*. CERN, 1977. doi: 10.5170/CERN-1977-009.

[52] G. Charpak et al. MWPC: The use of multiwire proportional counters to select and localize charged particles. *Nucl. Instrum. and Meth.*, **62**:262–268, 1968. doi: 10.1016/0029-554X(68)90371-6.

[53] C. L. Morris et al. Tomographic imaging with cosmic ray muons. *Sci. Glob. Secur.*, **16**:37–53, 2008. doi: 10.1080/08929880802335758.

[54] S. Pesente et al. First results on material identification and imaging with a large-volume muon tomography prototype. *Nucl. Instrum. Methods Phys. Res. A*, **604**(3):738–746, 2009. doi: 10.1016/j.nima.2009.03.017.

[55] C. Cârloganu et al. Towards a muon radiography of the Puy de Dôme. *Geosci. Instrum. Method. Data Syst.*, **2**:55–60, 2013. doi: 10.5194/gi-2-55-2013.

[56] S. Basnet et al. Towards a portable high-resolution muon detector based on Resistive Plate Chambers (RPCs). *Journal of Advanced Instrumentation in Science*, **2022**:Sept., 2022. doi: 10.31526/jais.2022.299.

[57] X.L. Chen et al. MRPC technology for muon tomography. *J. Instrum.*, **15**:C12001, 2020. doi: 10.1088/1748-0221/15/12/C12001.

[58] D. Bódizs. *(Hungarian) Atommagsugárzások méréstechnikái*. Typotex Kiadó, 2006.

[59] Z. Bay. Electron multiplier as an electron counting device. *Nature*, **141**:287, 1938. doi: 10.1038/1411011a0.

[60] D. Lo Presti et al. The MEV project: Design and testing of a new high-resolution telescope for muography of etna volcano. *Nucl. Instrum. Methods Phys. Res. A*, **904**: 195–201, 2018. doi: 10.1016/j.nima.2018.07.048.

[61] A. Anastasio et al. The MU-RAY experiment. an application of SiPM technology to the understanding of volcanic phenomena. *Nucl. Instrum. Methods Phys. Res. A*, **718**: 134–137, 2013. doi: 10.1016/j.nima.2012.08.065.

[62] K. Morishima et al. *Muography: Exploring Earth's Subsurface with Elementary Particles*. Wiley AGU Books, 2022. doi: 10.1002/9781119722748.ch21.

[63] R. Nishiyama et al. First measurement of ice-bedrock interface of alpine glaciers by cosmic muon radiography. *Geophys. Res. Lett.*, **44**:6244– 6251, 2017. doi: 10.1002/2017GL073599.

[64] M. Del Santo et al. Looking inside volcanoes with the imaging atmospheric cherenkov telescopes. *Nucl. Instrum. Methods Phys. Res. A*, **876**:111–114, 2017. doi: 10.1016/j.nima.2017.02.029. The 9th international workshop on Ring Imaging Cherenkov Detectors (RICH2016).

[65] D. Lo Presti et al. Feasibility study of a new cherenkov detector for improving volcano muography. *Sensors*, **19**:1183, 2019. doi: 10.3390/s19051183,.

[66] J. Bae and S. Chatzidakis. Fieldable muon spectrometer using multi-layer pressurized gas Cherenkov radiators and its applications. *Sci. Rep.*, **12**:2559, 2022. doi: 10.1038/s41598-022-06510-2.

[67] S. Kedar et al. Muon radiography for exploration of mars geology. *Geosci. Instrum. Method. Data Syst.*, **2**:157–164, 2013. doi: 10.5194/gi-2-157-2013.

[68] D. Varga et al. Detector developments for high performance muography applications. *Nucl. Instrum. Methods Phys. Res. A*, **958**:162236, 2020. doi: 10.1016/j.nima.2019.05.077.

[69] Á. Gera et al. Gaseous detectors for field applications: Quality control, thermal and mechanical stability. *Instruments*, **6**:74, 2022. doi: 10.3390/instruments6040074.

[70] L. Oláh et al. (Hungarian) Képalkotás kozmikus részecskék nyomkövetésével. *Fizikai Szemle*, **3**:75–76, 2017.

[71] K. Nagamine et al. Method of probing inner-structure of geophysical substance with the horizontal cosmic-ray muons and possible application to volcanic eruption prediction. *Nucl. Instrum. Methods Phys. Res. A*, **356**(2):585–595, 1995. doi: 10.1016/0168-9002(94)01169-9.

[72] R. Nishiyama et al. Monte Carlo simulation for background study of geophysical inspection with cosmic-ray muons. *Geophys. J. Int.*, **206**:1039–1050, 2016. doi: 10.1093/gji/ggw191.

[73] H. Gómez et al. Forward scattering effects on muon imaging. *J. Instrum.*, **12**:P12018, 2021. doi: 10.1088/1748-0221/12/12/p12018.

[74] L. Oláh et al. High-definition and low-noise muography of the Sakurajima volcano with gaseous tracking detectors. *Sci. Rep.*, **8**:3207, 2018. doi: 10.1038/s41598-018-21423-9.

[75] J. Peña Rodríguez et al. Muography background sources: simulation, characterization, and machine-learning rejection. *PoS*, (ICRC2021):400, 2021. doi: 10.22323/1.395.0400.

[76] L. Oláh et al. The first prototype of an MWPC-based borehole-detector and its application for muography of an underground pillar. *J-Stage*, **71**:161–168, 2018. doi: 10.3124/segj.71.161.

[77] J. Gluyas et al. Passive, continuous monitoring of carbon dioxide geostorage using muon tomography. *Phil. Trans. R. Soc. A.*, **377**:20180059, 2018. doi: 10.1098/rsta.2018.0059.

[78] A. Bonneville et al. Borehole muography of subsurface reservoirs. *Phil. Trans. R. Soc. A.*, **377**:20180060, 2019. doi: 10.1098/rsta.2018.0060.

[79] G. Saracino et al. A new cylindrical detector for borehole muon radiography. *Nucl. Instrum. Methods Phys. Res. A*, **1048**:167995, 2023. doi: 10.1016/j.nima.2022.167995.

[80] T. V. Acconcia et al. A very high momentum particle identification detector. *Eur. Phys. J. Plus*, **129**:91, 2014. doi: 10.1140/epjp/i2014-14091-5.

[81] D. Varga et al. Asymmetric Multi-Wire Proportional Chamber with reduced requirements to mechanical precision. *Nucl. Instrum. Methods Phys. Res. A*, **648**:163–167, 2011. doi: 10.1016/j.nima.2011.05.049.

[82] G.G. Barnaföldi et al. Portable cosmic muon telescope for environmental applications. *Nucl. Instrum. Methods Phys. Res. A*, **689**:60–69, 2012. doi: 10.1016/j.nima.2012.06.015.

[83] D. Varga et al. Close cathode chamber: Low material budget MWPC. *Nucl. Instrum. Methods Phys. Res. A*, **698**:11–18, 2013. doi: 10.1016/j.nima.2012.09.025.

[84] L. Oláh et al. Close Cathode Chamber technology for cosmic particle tracking. *J. Phys.: Conf. Ser.*, **632**:01202, 2015. doi: 10.1088/1742-6596/632/1/012020.

[85] F. Ludwig et al. The muon intensity in the Felsenkeller shallow underground laboratory. *Astroparticle Physics*, **112**:24–34, 2019. doi: 10.1016/j.astropartphys.2019.04.006.

[86] P. Ván et al. Long term measurements from the Mátra Gravitational and Geophysical Laboratory. *Eur. Phys. J. Spec. Top.*, **228**:1693–1743, 2019. doi: 10.1140/epjst/e2019-900153-1.

[87] D. Varga et al. High Efficiency Gaseous Tracking Detector for Cosmic Muon Madiography. *Adv. High Energy Phys.*, **2016**:1962317, 2016. doi: 10.1155/2016/1962317.

[88] D. Varga et al. Cosmic muon detector using proportional chambers. *Eur. J. Phys.*, **36**: 065006, 2015. doi: 10.1088/0143-0807/36/6/065006.

[89] D. Varga et al. Tracking detector for high performance cosmic muon imaging. *J. Instrum.*, **15**:C05007, 2020. doi: 10.1088/1748-0221/15/05/C05007.

[90] Z-Ultrat 3D printing material datasheet. https://cf.zortrax.com/wp-content/uploads/2018/06/Z-ULTRAT_Technical_Data_Sheet_eng-1.pdf. Accessed: 2023-03-22.

[91] D. Varga et al. Muographic observation instrument. Patent WO/2017/187308, 02 November 2017.

[92] G. Hamar et al. Gaseous tracking detectors at the Sakurajima Muography Observatory. *J. Phys.: Conf. Ser.*, **2374**:012188, 2022. doi: 10.1088/1742-6596/2374/1/012188.

[93] W. Blum and L. Rolandi. *Particle Detection with Drift Chambers*. Springer-Verlag, 1993.

[94] Y. Hayashi et al. A large area muon tracking detector for ultra-high energy cosmic ray astrophysics—-the GRAPES-3 experiment. *Nucl. Instrum. Methods Phys. Res. A*, **545** (3):643–657, 2005. doi: 10.1016/j.nima.2005.02.020.

[95] S. Wuyckens et al. A portable muon telescope based on small and gas-tight resistive plate chambers. *Phil. Trans. R. Soc. A.*, **377**:20180139, 2018. doi: 10.1098/rsta.2018.0139.

[96] L. Lopes et al. Towards sealed Resistive Plate Chambers. *J. Instrum.*, **15**:C11009, 2020. doi: 10.1088/1748-0221/15/11/C11009.

[97] S. Procureur et al. Why do we flush gas in gaseous detectors? *Nucl. Instrum. Methods Phys. Res. A*, **955**:163290, 2020. doi: 10.1016/j.nima.2019.163290.

[98] G. Nyitrai et al. Toward low gas consumption of muographic tracking detectors in field applications. *J. Appl. Phys.*, **129**:244901, 2021. doi: 10.1063/5.0053984.

[99] G. Nyitrai, G. Hamar, and D. Varga. Low gas consumption in tracking detectors for outdoor applications. *J. Phys.: Conf. Ser.*, **2374**:012181, 2021. doi: 10.1088/1742-6596/2374/1/012181.

[100] W. Diethorn. A methane proportional counter system for natural radiocarbon measurements. *USAEC Report*, **NY06628**, 1956.

[101] ASTM D4728-17. Standard test method for random vibration testing of shipping containers. *ASTM International: West Conshohocken, PA, USA*, **15.10**, 2017. doi: 10.1520/D4728-17.

[102] L. Oláh et al. MWPC-based muographic observation system for remote monitoring of active volcanoes. *Nucl. Instrum. Methods Phys. Res. A*, **936**:57–58, 2019. doi: 10.1016/j.nima.2018.11.004.

[103] L. Olah et al. Muographic monitoring of hydrogeomorphic changes induced by post-eruptive lahars and erosion of Sakurajima volcano. *Sci. Rep.*, **11**:17729, 2021. doi: 10.1038/s41598-021-96947-8.

[104] Y. Nomura et al. Pilot study of eruption forecasting with muography using convolutional neural network. *Sci. Rep.*, **10**:5272, 2020. doi: 10.1038/s41598-020-62342-y.

[105] L. Oláh et al. Muography of the active Sakurajima Volcano: Recent results and future perspectives of hazard assessment. *Journal of Advanced Instrumentation in Science*, **2022**:285, 2022. doi: 10.31526/jais.2022.285.

[106] L. Oláh et al. Muon imaging of volcanic conduit explains link between eruption frequency and ground deformation. *Geophys. Res. Lett.*, **50**(2):e2022GL101170, 2023. doi: 10.1029/2022GL101170.

[107] F. Sauli. *Micro-Pattern Gaseous Detectors*. World Scientific, 2020. doi: 10.1142/11882.

[108] F. Sauli. GEM: A new concept for electron amplification in gas detectors. *Nucl. Instrum. Methods Phys. Res. A*, **386**:531–534, 1997. doi: 10.1016/S0168-9002(96)01172-2.

[109] G. Charpak et al. A high-rate, high-resolution asymmetric wire chamber with mustrip readout. *Nucl. Instrum. Methods Phys. Res. A*, **346**:506–509, 1994. doi: 10.1016/0168-9002(94)90585-1.

[110] G. Nyitrai. MicroPattern Gaseous Detectors: construction and applications in large tracking systems. *20th Zimányi School Winter Workshop on Heavy Ion Physics, Budapest, Hungary*, Dec. 7-11 2020.

[111] S. Procureur et al. Precise characterization of a corridor-shaped structure in khufu's pyramid by observation of cosmic-ray muons. *Nat. Commun.*, **14**:1144, 2023. doi: 10.1038/s41467-023-36351-0.

[112] H. Gómez et al. Muon tomography with micromegas: Archaeology, nuclear safety and new developments for geotechnics. *J. Phys.: Conf. Ser.*, **1312**:012013, 2019. doi: 10.1088/1742-6596/1312/1/012013.

[113] I. Lázaro Roche. A compact muon tracker for dynamic tomography of density based on a thin time projection chamber with micromegas readout. *Particles*, **4**:333–342, 2021. doi: 10.3390/particles4030028.

[114] K. Gnanvo et al. Imaging of high-Z material for nuclear contraband detection with a minimal prototype of a muon tomography station based on GEM detectors. *Nucl. Instrum. Methods Phys. Res. A*, **652**(1):16–20, 2011. doi: 10.1016/j.nima.2011.01.163.

[115] G. Hamar and D. Varga. TCPD, a TGEM based hybrid UV photon detector. *J. Instrum.*, **8**:C12038, 2013. doi: 10.1088/1748-0221/8/12/C12038.

[116] G. Galgóczi et al. A GEM based TPC for beam monitoring. *J. Instrum.*, **15**:C08027, 2020. doi: 10.1088/1748-0221/15/08/C08027.

[117] T.E. Hilden et al. GEM foil gain prediction. *PoS*, (MPGD2017):010, 2019. doi: 10.22323/1.322.0010.

[118] T. Hildén et al. Optical quality assurance of GEM foils. *Nucl. Instrum. Methods Phys. Res. A*, **770**:113–122, 2015. doi: 10.1016/j.nima.2014.10.015.

[119] A.L. Gera. Upgrade of the ALICE Time Projection Chamber for the LHC Run3. *PoS*, (EPS-HEP2019):102, 2020. doi: 10.22323/1.364.0102.

[120] A. Breskin et al. A concise review on thgem detectors. *Nucl. Instrum. Methods Phys. Res. A*, **598**:107–111, 2009. doi: 10.1016/j.nima.2008.08.062.

[121] V. Peskov et al. First observation of Cherenkov rings with a large area CsI-TGEM-based RICH prototype. *Nucl. Instrum. Methods Phys. Res. A*, **695**:154–158, 2012. doi: 10.1016/j.nima.2011.11.045.

[122] G. Hamar and D. Varga. High resolution surface scanning of Thick-GEM for single photo-electron detection. *Nucl. Instrum. Methods Phys. Res. A*, **694**:16–23, 2012. doi: 10.1016/j.nima.2012.07.035.

[123] M. Baruzzo et al. Direct measurements of the properties of Thick-GEM reflective photocathodes. *Nucl. Instrum. Methods Phys. Res. A*, **972**:164099, 2020. doi: 10.1016/j.nima.2020.164099.

[124] G. Nyitrai et al. MPGD hole-by-hole gain scanning by UV excited single photoelectron detection. *Nucl. Instrum. Methods Phys. Res. A*, **958**:162726, 2020. doi: 10.1016/j.nima.2019.162726.

[125] G. Hamar and D. Varga. High granularity scanner for MPGD based photon detectors. *PoS*, (TIPP2014):056, 2014. doi: 10.22323/1.213.0056.

[126] M. Alexeev et al. Status of the development of large area photon detectors based on THGEMs and hybrid MPGD architectures for Cherenkov imaging applications. *Nucl. Instrum. Methods Phys. Res. A*, **824**:139–142, 2016. doi: 10.1016/j.nima.2015.11.034.

[127] S. Boglárka. (Hungarian) Müográfiai direkt probléma megoldása mérés optimalizáláshoz. *Tudományos Diákköri Dolgozat*, (ELTE Geofizika MSc), 2022.

[128] T. K. Gaisser and T. Stanev. Cosmic rays (review of particle physics). *Physics Letters, B*, **592**:228, 2004. doi: 10.1016/j.physletb.2004.06.011.

[129] M. Guan et al. A parametrization of the cosmic-ray muon flux at sea-level. arXiv: 1509.06176 [hep–ex], 2015. doi: 10.48550/arXiv.1509.06176.

[130] D. Reyna. A simple parameterization of the cosmic-ray muon momentum spectra at the surface as a function of zenith angle. arXiv:hep–ph/0604145, 2006. doi: 10.48550/arXiv.hep-ph/0604145.

[131] E. V. Bugaev et al. Cosmic rays (review of particle physics). *Phys. Rev. D*, **58**:054001, 1998. doi: 10.1103/PhysRevD.58.054001.

[132] D. Heck et al. CORSIKA: A Monte Carlo code to simulate extensive air showers. *FZKA-6019*, 2 1998.

[133] S. Agostinelli et al. Geant4 — a simulation toolkit. *Nucl. Instrum. Methods Phys. Res. A*, **506**(3):250–303, 2003. doi: 10.1016/S0168-9002(03)01368-8.

[134] T. Hebbeker and C. Timmermans. A compilation of high energy atmospheric muon data at sea level. *Astroparticle Physics*, **18**:107–127, 2002. doi: 10.1016/S0927-6505(01)00180-3.

[135] P. Kuusiniemi et al. Muography and geology: Does it matter which continent you stand on? *Journal of Advanced Instrumentation in Science*, **2022**:257, 2022. doi: 10.31526/JAIS.2022.257.

[136] A. Lechmann et al. The effect of rock composition on muon tomography measurements. *Solid Earth*, **9**:1517–1533, 2018. doi: 10.5194/se-9-1517-2018.

[137] J. Reichenbacher. Calculation of the underground muon intensity crouch curve from a parameterization of the flux at surface. arXiv:0706.1110 [hep–ph], 2007. doi: 10.48550/arXiv.0706.1110.

[138] A. Tarantola. *Inverse Problem Theory and Methods for Model Parameter Estimation*. Society for Industrial and Applied Mathematics, Philadelphia, 2005. doi: 10.1137/1.9780898717921.

[139] R. Nishiyama et al. Integrated processing of muon radiography and gravity anomaly data toward the realization of high-resolution 3-D density structural analysis of volcanoes: Case study of Showa-Shinzan lava dome, Usu, Japan. *J. Geophys. Res. Solid*, **119**(1):699–710, 2014. doi: 10.1002/2013JB010234.

[140] R. Nishiyama. *Joint Inversion of Muography and Gravity Data for 3D Density Imaging of Volcanoes*. In: Oláh, L., et al., Muography: Exploring Earth's Subsurface with Elementary Particles. Chapter 3. Wiley AGU Books, 2022. doi: 10.1002/9781119722748.ch3.

[141] S. Nagahara and S. Miyamoto. Feasibility of three-dimensional density tomography using dozens of muon radiographies and filtered back projection for volcanos. *Geosci. Instrum. Method. Data Syst.*, **7**:307–316, 2018. doi: 10.5194/gi-7-307-2018.

[142] S. Miyamoto and S. Nagahara. *Tomographic Imaging of Volcano Structures with Cosmic-Ray Muons*. In: Oláh, L., et al., Muography: Exploring Earth's Subsurface with Elementary Particles. Chapter 2. Wiley AGU Books, 2022. doi: 10.1002/9781119722748.ch2.

[143] A. Barnoud et al. Bayesian joint muographic and gravimetric inversion applied to volcanoes. *Geophys. J. Int.*, **218**:2179–2194, 2019. doi: 10.1093/gji/ggz300.

[144] E. Guardincerri et al. 3D cosmic ray muon tomography from an underground tunnel. *Pure Appl. Geophys.*, **174**:2133–2141, 2017. doi: 10.1007/s00024-017-1526-x.

[145] K. Cosburn, M. Roy, and R. Nishiyama. A machine learning approach to joint gravity and cosmic-ray muon inversion at Mt. Usu, Japan. *Geophys. J. Int.*, **233**:1081–1096, 2022. doi: 10.1093/gji/ggac497.

[146] N. Lesparre et al. Bayesian dual inversion of experimental telescope acceptance and integrated flux for geophysical muon tomography. *Geophys. J. Int.*, **188**:490–497, 2012. doi: 10.1111/j.1365-246X.2011.05268.x.

[147] D. W. Schouten and P. Ledru. Muon tomography applied to a dense uranium deposit at the McArthur River mine. *J. Geophys. Res. Solid Earth*, **123**:8637– 8652, 2018. doi: 10.1029/2018JB015626.

[148] D. Borselli et al. Three-dimensional muon imaging of cavities inside the Temperino mine (Italy). *Sci. Rep.*, **12**:22329, 2018. doi: 10.1038/s41598-022-26393-7.

[149] L. Cimmino et al. 3D muography for the search of hidden cavities. *Sci. Rep.*, **9**:2974, 2019. doi: 10.1038/s41598-019-39682-5.

[150] G. Liu et al. High-precision muography in archaeogeophysics: A case study on Xi'an defensive walls. *J. Appl. Phys.*, **133**:014901, 2023. doi: 10.1063/5.0123337.

[151] S. Nagahara et al. Three-dimensional density tomography determined from multidirectional muography of the Omuroyama scoria cone, Higashi–Izu monogenetic volcano field, Japan. *Bull. Volcanol.*, **84**:94, 2022. doi: 10.1007/s00445-022-01596-y.

[152] S. Procureur et al. 3D imaging of a nuclear reactor using muography measurements. *Sci. Adv.*, **9**:eabq8431, 2023. doi: 10.1126/sciadv.abq8431.

[153] V. Tioukov et al. Hidden chamber discovery in the underground Hellenistic necropolis of Neapolis by muography. *Sci. Rep.*, **13**:5438, 2023. doi: 10.1038/s41598-023-32626-0.

[154] F. Natterer and F. Wübbeling. *Mathematical methods in image reconstruction*. SIAM monographs on mathematical modeling and computation, 2001.

[155] D. S. Lalush and M. N. Wernick. Chapter 21 - iterative image reconstruction. In M. N. Wernick and J. N. Aarsvold, editors, *Emission Tomography*, pages 443–472. Academic Press, San Diego, 2004. ISBN 978-0-12-744482-6. doi: 10.1016/B978-012744482-6.50024-7.

[156] L. Balázs, G. Nyitrai, G. Surányi, G. Hamar, G.G. Barnaföldi, and D. Varga. 3D muographic inversion in the exploration of cavities and low-density fractured zones. *Geophys. J. Int.*, **(accepted)**, 2023. doi: 10.48550/arXiv.2309.12057.

[157] D. Varga et al. Construction and readout systems for gaseous muography detectors. *Journal of Advanced Instrumentation in Science*, **2022**:Jun., 2022. doi: 10.31526/jais.2022.307.